Simulation of electronic states in a nanowire field-effect transistor

A PhD thesis

by

José María Castelo Ares

directed by

Prof. Dr. Klaus Michael Indlekofer

and tutored by

Dr. Alberto García Cristóbal

Departamento de Física Aplicada
Universidad de Valencia

VNIVERSITAT DE VALÈNCIA

2015

This thesis took place at the Hochschule RheinMain (University of Applied Sciences) in Rüsselsheim (Germany) during the period 2011–2014

Hochschule **RheinMain**
University of Applied Sciences
Wiesbaden Rüsselsheim

within the framework of Nanowiring:
European Marie Curie Initial Training Network

nanowiring
sensing • lighting • energy • electronics

Abstract

Nanowires are emerging as promising candidates to form the basis of field-effect transistors, among other devices. Nanowire-based field-effect transistors are foreseen to be industrially standardized in the near future. Simulations are important in order to assess their performance. The multi-configurational self-consistent Green's function simulation method is able to correctly describe non-equilibrium electronic transport while at the same time accounts for few-electron Coulomb charging effects in such devices. Based on the non-equilibrium Green's function formalism, this method is augmented and implemented in a software package named **NWFET-Lab**. This package forms the basis of the calculations performed in this dissertation.

An adaptive numerical method to determine the non-equilibrium many-body statistical operator for quasi-isolated electronic states within the channel of a realistic nanowire field-effect transistor is presented. The statistical operator must satisfy a set of constraints related to the single-particle density matrix. Since the problem is under-determined in general, a form for its eigenvalues or weights that maximizes the entropy is required. Two eigenbases for the statistical operator are considered: (A) the set of all relevant Slater determinants of natural orbitals and (B) the eigenstates of the many-body Hamiltonian projected to the relevant Fock subspace. As an application, the onset of formation of Wigner molecules is addressed with the help of the density–density covariance.

A new numerical determination of the correlation of the system of electrons within the nanowire channel of the device, for pure as well as for mixed states, is presented. In contrast to the single-particle-reduced entropy, this so-called "modified correlation entropy" accounts for the correlation independently of the mixture degree, as measured by the von Neumann entropy, of the many-body state. For its determination a genetic algorithm optimization method is employed. An analysis of these three concepts of entropy is performed.

Resumen

De acuerdo con la ley empírica de Moore, el número de transistores en un circuito integrado se ve duplicado aproximadamente cada dos años. Una vez traspasada la frontera hacia la escala nanométrica, estos dispositivos comienzan a padecer efectos adversos al funcionamiento deseable de un transistor, como la pérdida de integridad eléctrica, efectos debidos a la corta longitud del canal o la falta de reproducibilidad. Las nanoestructuras cristalinas semiconductoras conocidas como nanohilos están emergiendo como candidatos prometedores para formar una nueva base alternativa de los transistores de efecto campo y continuar la miniaturización tecnológica en la escala nanométrica. Esto es debido al gran control electrostático de la puerta sobre el canal, constituido en estos dispositivos por un nanohilo, que los transistores de efecto campo basados en nanohilos demuestran a esta escala. Como beneficios adicionales del empleo de nanohilos para la construcción de estos dispositivos cabe mencionar la posibilidad de ser producidos en grandes cantidades en un solo proceso usando técnicas de crecimiento asequibles. Estas nanoestructuras presentan propiedades electrónicas reproducibles debido al control preciso del proceso de crecimiento, así como una alta movilidad de los portadores de carga consecuencia de su estructura monocristalina y su reducción de la dispersión. Junto a significativos avances experimentales, su estudio teórico está resultando de importancia para evaluar sus características y rendimiento.

Los dispositivos nanométricos están gobernados por las leyes de la mecánica cuántica, por lo que un método de simulación apropiado para su estudio debería ser capaz de describir efectos cuánticos como el confinamiento, las resonancias, la dispersión o el efecto tunel de los electrones en su interior. El número de electrones involucrados en el funcionamiento de transistores con canales de una longitud tan grande como 100 nm es del orden de $1 - 10$. Por tanto, efectos debidos a la presencia individual de electrones son relevantes en estos dispositivos, de modo que una descripción de muchos cuerpos (basada en el espacio de Fock) de la interacción de Coulomb es necesaria para una simulación realista. Por un

lado, un enfoque que considere el espacio de Fock completo del sistema es capaz de describir correctamente estos efectos, pero ve limitada su aplicación efectiva a dispositivos pequeños, debido a que la dimensión del espacio de Fock aumenta exponencialmente con el número de estados de una partícula (por ejemplo orbitales localizados). Por otro lado, una descripción de campo medio para modelizar la interacción de Coulomb es viable computacionalmente pero incapaz de describir efectos debidos a la presencia individual de electrones, a causa de la aproximación que esta descripción realiza de tal interacción como efecto promediado que tiene sobre un electron el resto de electrones.

La base teórica del trabajo presentado en esta tesis doctoral está fundamentada en el método multiconfiguracional autoconsistente basado en funciones de Green, originalmente presentado por Indlekofer et al. Este método está basado en el formalismo de funciones de Green fuera del equilibrio y como es habitual en este formalismo, se hace uso de una descripción de campo medio para modelizar la interacción de Coulomb. Sin embargo, el método limita este tipo de descripción para aquellos estados que no son relevantes para el transporte electrónico, haciendo uso de una descripción de muchos cuerpos (basada en un subespacio de Fock relevante) para los que sí son relevantes. Estados de una partícula relevantes son identificados como aquellos orbitales naturales (autoestados de la matriz densidad de una partícula ρ_1) que presentan fluctuación en su número de ocupación (autovalores de ρ_1) y que no se encuentran fuertemente acoplados a los contactos del transistor, centrándose en estados atrapados resonantemente en el interior del nanohilo. El número de estados relevantes N_{rel} es habitualmente muy inferior al número total de estados del sistema, la dimensión del subespacio de Fock generado por los estados relevantes no es muy alta y una descripción de muchos cuerpos dentro de este subespacio resulta ser asequible.

Uno de los objetivos de la presente tesis doctoral es el desarrollo de una herramienta informática de simulación para el estudio de las propiedades de transporte electrónico en transistores de efecto campo basados en nanohilos. El paquete de programas se conoce como **NWFET-Lab** e incluye tres módulos interrelacionados. El primero de ellos tiene la función de preparar los parámetros del sistema. El segundo consiste en el módulo de cálculo, fundamentado en el método multiconfiguracional autoconsistente basado en las funciones de Green, sucintamente descrito en el párrafo anterior. Este algoritmo original ha sido extendido

para incluir una mayor variedad de observables físicos y magnitudes relevantes para entender el comportamiento y características de un transistor basado en un nanohilo, así como los cálculos que a continuación se describen. El tercero y último de los módulos permite la visualización de los resultados obtenidos mediante el módulo de cálculo.

También se ha desarrollado un método numérico para la determinación del operador estadístico de muchos cuerpos fuera del equilibrio $\hat{\rho}_{\text{rel}}$ para el sistema de electrones atrapados resonantemente en el interior del nanohilo del transistor. La importancia de conocer el operador estadístico radica en que permite obtener valores esperados de observables de muchos cuerpos del sistema, así como la entropía de von Neumann. Este operador debe satisfacer ciertas restricciones dadas por la matriz densidad de una partícula ρ_1. Estas condiciones no son suficientes en general para su determinación unívoca, por lo que se ha escogido una forma funcional de los autovalores de $\hat{\rho}_{\text{rel}}$ que maximice la entropía, conocida como forma gran-canónica o de Boltzmann. En esta forma funcional aparecen los potenciales electroquímicos asociados a los orbitales naturales relevantes, que se convierten en cantidades independientes si el sistema se encuentra fuera del equilibrio y se consideran como variables de optimizacion libres que ajustar para que los autovalores cumplan las restricciones impuestas por ρ_1. Como autoestados de $\hat{\rho}_{\text{rel}}$ se consideran dos bases alternativas: (A) determinantes de Slater de orbitales naturales relevantes y (B) la base del Hamiltoniano de muchos cuerpos proyectado al subespacio de Fock relevante. A modo de aplicación, se ilustra la transición desde un régimen del sistema de electrones en el canal del transistor denominado "atómico" en el que la energía de Coulomb es relativamente pequeña, hasta un régimen denominado "Wigner" en el que esta energía es mayor, favoreciendo la separacion entre electrones y la consiguiente formación de moléculas de Wigner.

Finalmente se presenta una medida numérica de la correlación del sistema de electrones, que cuantifica únicamente su correlación tanto si la preparación del sistema es pura como si es una mezcla, en contraste con la entropía reducida de una partícula S_1 que también depende del grado de mezcla y por tanto sólo puede cuantificar la correlación de estados puros. Esta medida numérica, denominada entropía de correlación modificada $\Delta S \equiv \widetilde{S} - S$ se basa en la entropía de von Neumann S, cuyo cálculo depende del operador estadístico de muchos cuerpos fuera del equilibrio $\hat{\rho}_{\text{rel}}$ del sistema. Asimismo, $\widetilde{S}$ es la entropía de von Neumann

obtenida mediante de un operador estadístico $\widetilde{\rho}_{\text{rel}}$ que se asemeja óptimamente a $\hat{\rho}_{\text{rel}}$ pero cuya base de estados de muchos cuerpos consiste únicamente en determinantes de Slater construidos a partir de una base ortonormal optimizada de estados de una partícula, obtenida de tal manera que $\widetilde{S}$ sea minimizada. Esta base se encuentra relacionada con la base de orbitales naturales mediante una transformación unitaria U con $N_{\text{rel}} \times N_{\text{rel}}$ elementos. El proceso de minimizacion se lleva a cabo mediante un algoritmo genético cuyas variables de optimización son los $N_{\text{rel}} \times N_{\text{rel}}$ ángulos mediante los cuales es posible parametrizar U. Como resultado, se presenta un análisis de estos tres tipos de entropía (S_1, S y ΔS) y se muestra que efectivamente ΔS cuantifica la correlación electrónica independientemente del grado de mezcla.

Acknowledgement

I am grateful to my supervisor Klaus Michael Indlekofer, who treated me from the beginning with friendliness and helped me whenever I needed it. I would also like to thank my tutor Alberto García Cristóbal as well as all the people I got to know during these three years both in Rüsselsheim and in Valencia. Special thanks go to all the organizers of the Nanowiring network for giving all its members a valuable framework within which our careers, scientific skills and knowledge had the opportunity to develop. Thanks to all the fellows of the network for the good moments we shared and to the European Comission for financial support.

Contents

1. Introduction

1.1. The nanowire field-effect transistor

In this introductory chapter, we briefly address the problem of the downscaling of field-effect transistors (FETs), point out a candidate solution for this problem, see why this solution is promising and outline an overview of the devices this solution has enabled so far.

Since the invention of the integrated circuit (IC) in 1958 and the creation of the metal-oxide-semiconductor field-effect transistor (MOSFET) [1] in 1959, technology has followed a miniaturization trend expressed by Moore's law: the number of transistors on ICs doubles approximately every two years [2, 3]. This law, initially considered as a forecast, was later adopted as a target that has driven the industry up until the present.

The answer to the question of whether nanotechnology will be able to continue fulfilling Moore's law, despite the several difficulties [4, 5] that emerge as the channel length of MOSFETs gets smaller, depends on whether electrical integrity, no short-channel effects, low power consumption, low leakage currents and reproducibility can be maintained in ever downscaled devices. In this sense, replacement of old materials with new nanostructures may give an affirmative answer to that question.

The International Technology Roadmap for Semiconductors (ITRS) is a reference for the near and far future of semiconductor technology. As stated in the 2013 edition report [6], one of the main goals of the ITRS is identifying key technical requirements critical to sustain the historical scaling of semiconductor technology (Moore's law). In the same report one finds reference to major technological innovations, including new structures such as gate-all-around nanowires as next natural evolution for digital logic applications for the near term (2013-2020) and nanowire MOSFETs to below 10 nm gate length for the long term

(2021-2028). The report emphasizes the importance of understanding, modeling and implementation into manufacturing of these innovations.

Therefore, promising candidates for new electronics building blocks are semiconductor nanowires [7, 8, 9, 10]. Employing either a top-down or a bottom-up approach [11], these nanostructures are nowadays synthesized in a rational and controllable way, enabling the possibility to create axial and radial heterostructures and select the doping by addition of impurities. Due to their unique physical, chemical and electronic properties, nanowires find application in electronics [12, 13, 14, 15], optoelectronics [16], photovoltaics [17, 18], sensing [19] and biology [20, 21, 22].

Key to this dissertation is the nanowire field-effect transistor (NWFET) [23]. Similarly to a planar MOSFET, a NWFET is an active unipolar electronic device consisting of a channel, an insulator and gate, source and drain contacts. A basic difference between these types of devices, though, is that the channel of a NWFET is made of a single semiconductor nanowire, through which the electric carriers flow. On the other hand, the principles of operation do not differ between NWFETs and planar MOSFETs. Current is due to a bias voltage V_{DS} between the drain contact and the source contact, both contacts located at the extremes of the nanowire. The gate is a metallic electrode that modulates the electrostatic potential inside the channel and therefore influences the current via a gate–source voltage V_{GS}. There are two main gate geometries: planar and coaxial. A planar gate consists of a two-dimensional (2D) electrode positioned at the back, top or one side of the nanowire, while a coaxial or wrap gate is built all around the nanowire. It is isolated from the channel by an oxide insulator so that electrons are unable to flow out of the channel towards the gate.

The source and drain contacts can be ohmic or Schottky. Ohmic contacts consist of the two extremes of the intrinsic nanowire being heavily doped. Schottky contacts on the other hand, are made by metal deposited on the extremes of the nanowire, forming Schottky-barriers [24, 25] that the electrons in the source have to surpass or tunnel in order to contribute to the current. The device is then termed Schottky-barrier NWFET (SB-NWFET). See Fig. 1.1 for a schematic view of a SB-NWFET geometry.

It can be shown by the electrostatic analysis [26] of the NWFET, employing the one-dimensional (1D) Poisson equation for the potential at the channel–dielectric

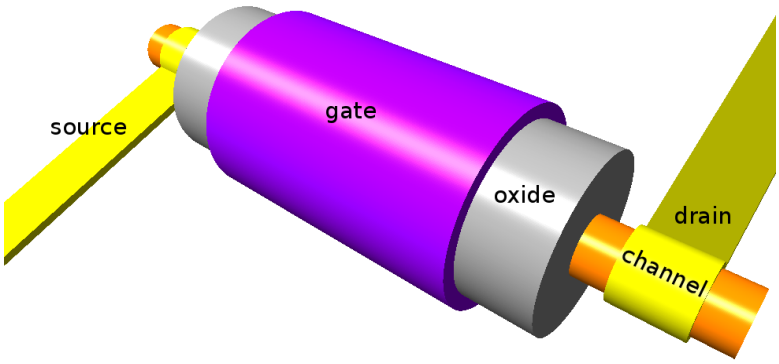

Figure 1.1.: Schematic view of a SB-NWFET.

interface $\Phi(x)$, that the relevant length scale for potential variations is given by the screening length λ, which appears both in the 1D Poisson equation and in its solution for point charge density $\Phi(x) \propto \exp(-|x|/\lambda)$.

For a coaxial gate geometry as shown in Fig. 1.1 the screening length λ is given by [27]

$$\lambda^2 = \frac{\varepsilon_{ch}}{\varepsilon_{ox}} \frac{d_{ch}^2}{8} \ln\left(1 + 2\frac{d_{ox}}{d_{ch}}\right) \tag{1.1}$$

where d_{ch} is the nanowire diameter, d_{ox} is the oxide thickness, ε_{ch} and ε_{ox} are the channel and oxide relative dielectric constants respectively.

In order to avoid the appearance of short-channel effects [5] when scaling down the channel length, λ has to be scaled accordingly in order to maintain the relation $L \gg \lambda$, which implies that the nanowire diameter d_{ch} and the oxide thickness d_{ox} must be scaled down. In this respect, nanowires are ideally suited for ultimately scaled FET devices, because of their one dimensional shape with a scalable diameter into the few nanometer range.

As additional benefits of employing nanowires for FET construction it is worth mentioning the possibility to be produced in large quantities in a single process, using bottom-up growth techniques that are cost-effective. They present reproducible electronic properties due to the precise control of the growth process. They also display high carrier mobility due to reduction of scattering because of their monocrystalline structure. Moreover, vertical integration of NWFETs in densely packed ICs is now possible, which is a necessity for their large-scale manufacturability.

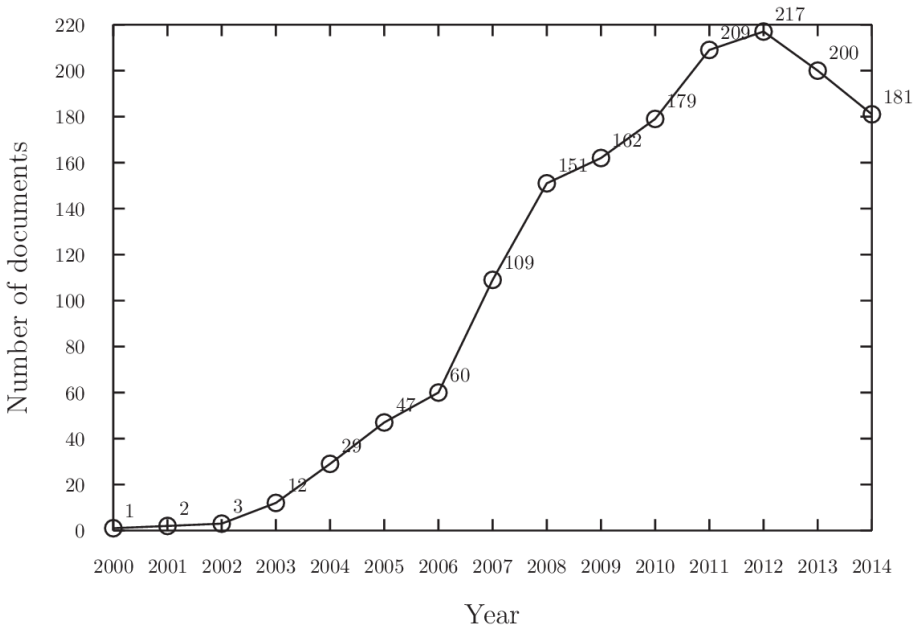

Figure 1.2.: Number of publications per year which include the keywords "nanowire transistor" or "nanowire field effect transistor" or "NWFET" in their contents, as obtained from Elsevier's database Scopus (http://www.scopus.com/). Note that the latest years do not include all the publications, only those available to the database at the moment.

Starting from the year 2000, the number of publications related to NWFET fabrication is growing, a fact that shows the interest and impact this subject is having since then. One can see this tendency in Fig. 1.2. In the year 2000, vanadium pentoxide V_2O_5 nanofiber-based FETs were reported [28]. The following year, NWFETs were demonstrated based on single-crystal InP nanowires, up to tens of micrometers long [29]. Radial nanowire heterostructures have also been employed as NWFETs, such as Ge/Si core/shell nanowires with a top-gate geometry, which showed improved *p*-type FET behavior [30]. Motivated by the consideration that current flowing in the on-state of NWFETs may be low due to the small diameter of the nanowire channel, a recent work proposes a massive parallel dense vertical nanowire array architecture for high performance FET [14]. Vertical integration [31, 32] is able to achieve a much higher density of nanowires than horizontal integration [33] and allows three-dimensional (3D) integration for complex structures. It is worth mentioning that programmable nanowire circuit modules have also been designed that use arrays of non-volatile multi-gate

NWFETs to operate as scalable nanoprocessors that perform simple logic functions [13]. As a step forward, a nanowire-based 2-bit 4-state finite-state machine has been implemented which is able to maintain its internal state, modify this state in response to external signals and output commands on that basis [15].

To summarize, as MOSFETs size enters into the nanometer scale, these devices begin to be prone to several effects that impede their proper functioning and a classical description of their physics begins to be inadequate. Promising candidates to become new building blocks for electronic devices are nanowires, which find application beyond the field of electronics. The NWFET in particular is expected to play an important role in the future, due to its superior electrostatic control of the channel by the gate in the nanoscale. Many advances in the experimental realization of nanowire-based devices have been reported, as well as important progresses in their simulation, where quantum and Coulomb effects in the nanoscale play a relevant role.

1.2. Ultimately scaled device simulation

Some of the challenges semiconductor technology will face in the near future in relation to nanowire-based devices, according to the ITRS 2013 [6], are the stochastic variation of dopants and thickness from device to device, the effects of the channel surface roughness on carrier transport and reliability, and controlling the source/drain series resistance within tolerable limits, since due to the increase of current density, lower resistance with smaller device dimensions is a challenging necessity. Simulation of NWFETs is therefore necessary to accurately predict the device performance and to understand its physics.

Nanoscale devices are governed by the laws of quantum mechanics, due to their small size in the nanometer scale. Therefore, a successful simulation method should be able to describe quantum effects, such as carrier confinement, resonances, scattering or tunneling. Furthermore, few-electron charging effects are of relevance in such devices, so a many-body description of the Coulomb interaction between electrons is necessary for a realistic simulation of NWFETs.

Present work on the simulation of these challenges usually focuses on a particular aspect of the problem and excludes the rest, whenever this restriction is justified by the features of the considered problem. So one can find in the lit-

erature simulations of the electronic transport characteristics for non-interacting electrons, in the presence of electron–electron or electron–phonon interaction. Quantum mechanical formalisms employed for the modeling of electronic transport in nanodevices, based on Schrödinger equation [34, 35], Wigner function [36], Liouville [37] and Pauli [38] master equations or Green's functions [39] have been reported.

Key to this dissertation is the non-equilibrium Green's function (NEGF) formalism [40, 41, 42, 43, 44], which allows for a quantum mechanical description of non-equilibrium electronic transport in ultimately scaled devices. This formalism may include the effects of the device contacts (reservoirs) and the relevant interactions (electron–electron and electron–phonon). Coulomb interaction, whenever it is considered, is usually modeled in a mean-field way, which has the advantage of being computationally light-weight and the disadvantage of being unable to describe few-electron charging effects. On the other hand, a full many-body description of this interaction is able to account for these effects at the expense of considering only small devices, as described by a suitable basis of single-particle states (localized spin/site orbitals, for example), since the corresponding Fock space dimension grows exponentially with the number of single-particle states, making simulation of realistic devices unfeasible.

As an hybrid approach that shares both the benefits of the mean-field and many-body descriptions, the multi-configurational self-consistent Green's function (MCSCG) method [45, 46] can correctly describe few-electron charging effects in a non-equilibrium NWFET. This method is the theoretical basis for the calculations and results obtained in this dissertation.

1.3. Structure of the dissertation

The basic formalism employed in this dissertation for the description of non-equilibrium NWFETs is the NEGF method. A theoretical introduction to NEGF is given in Chapter 2, where recent work concerning the simulation and understanding of the important challenges NWFETs face today is also described. Chapter 3 presents a description of the NEGF-based MCSCG method, which is the algorithm employed in the following calculations. The implementation of the MCSCG method in a software package is highlighted and several results (in the Coulomb

blockade regime) obtained by means of this implementation are presented. In Chapter 4 a numerical method to determine the non-equilibrium many-body statistical operator that describes the statistical preparation of the electrons within the NWFET channel is presented. The statistical operator is required to satisfy a set of constraints and its expression is furthermore determined by assuming its probability distribution maximizes the entropy. Once obtained, expectation values of many-body observables can be calculated. As an application, the onset of formation of Wigner molecules by the electrons within the nanowire channel is addressed. In Chapter 5 we study the correlation entropy of the electronic system. Three different definitions of entropy are analyzed and their significance (whether they account for mixture, correlation or both) is investigated. To conclude, a summary about the presented work and possible future ways to extend it is outlined in Chapter 6.

The appendices provide additional information. Appendix A, in particular, contains a description of **NWFET-Lab**, the open-source software package developed as a tool to simulate non-equilibrium electronic transport in NWFETs. It implements and extends the MCSCG algorithm, and provides all the calculations included in this dissertation.

2. Introduction to the non-equilibrium Green's function formalism

2.1. Quantum field operators

The many-body quantum description of a system of Fermions known as second quantization, relies on some mathematical objects known as the creation and annihilation operators [47, 44], expressed as $c_k^\dagger$ and c_k, corresponding to a state k of a discrete orthonormal single-particle basis. Operators in the Fock space can be represented in terms of them, in their so-called second quantized form. $c_k^\dagger$ and c_k act on a many-body state by creating or annihilating, respectively, a particle on a given single-particle state k. In the occupation number representation, where the state of the system is described by a vector $|b_0 b_1 \dots b_k \dots\rangle$ with $b_k \in \{0, 1\}$, this can be expressed as [48]

$$c_k \,|\dots b_k \dots\rangle = (-1)^{S_k} \delta_{b_k,1} \,|\dots b_k - 1 \dots\rangle \tag{2.1a}$$

$$c_k^\dagger \,|\dots b_k \dots\rangle = (-1)^{S_k} \delta_{b_k,0} \,|\dots b_k + 1 \dots\rangle \tag{2.1b}$$

where $S_k = b_0 + b_1 + \cdots b_{k-1}$ counts how many occupied states are on the left of single-particle state k.

As a consequence of the indistinguishability of Fermions, their many-body quantum state is antisymmetric under the interchange of two particles. This implies that these operators satisfy the following anti-commutation relations [42, 43, 44]

$$\{c_k, c_{k'}^\dagger\} = \delta_{kk'} \tag{2.2a}$$

$$\{c_k, c_{k'}\} = \{c_k^\dagger, c_{k'}^\dagger\} = 0 \tag{2.2b}$$

where we denote $\{A, B\} = AB + BA$. The Fermionic quantum statistics is respected by working with these operators satisfying these anti-commutation relations. In particular, the Pauli exclusion principle is seen to hold by noting that $c_k^\dagger c_k^\dagger = 0$, by virtue of Eqs. (2.2b), so no two particles can be in the same state. Analogous operators and commutation relations exist for Bosonic systems.

In the position basis, the creation and annihilation operators are known as quantum field operators, $\psi^\dagger(\mathbf{x}, \sigma)$ and $\psi(\mathbf{x}, \sigma)$, which create and annihilate, respectively, a particle at position $\mathbf{x}$ with spin σ. They can be expressed in terms of the creation and annihilation operators, $c_k^\dagger$ and c_k, associated to a discrete single-particle orthonormal basis $\{\phi_k(\mathbf{x}, \sigma)\}$ as follows [42, 44]

$$\psi^\dagger(\mathbf{x}, \sigma) = \sum_k \phi_k^*(\mathbf{x}, \sigma) c_k^\dagger \tag{2.3a}$$

$$\psi(\mathbf{x}, \sigma) = \sum_k \phi_k(\mathbf{x}, \sigma) c_k \quad . \tag{2.3b}$$

As an example, the basis states $\phi_k(\mathbf{x}, \sigma)$ can be localized atomic sites of a tight-binding model, where $c_k^\dagger$ and c_k create and remove an electron at site k. It can be shown [42, 43] that given Eqs. (2.2) and Eqs. (2.3), the quantum field operators satisfy the following anti-commutation relations

$$\{\psi(\mathbf{x}, \sigma), \psi^\dagger(\mathbf{x}', \sigma')\} = \delta(\mathbf{x} - \mathbf{x}')\delta_{\sigma\sigma'} \tag{2.4a}$$

$$\{\psi(\mathbf{x}, \sigma), \psi(\mathbf{x}', \sigma')\} = \{\psi^\dagger(\mathbf{x}, \sigma), \psi^\dagger(\mathbf{x}', \sigma')\} = 0 \quad . \tag{2.4b}$$

2.2. Hamiltonian in second quantization

We consider the Hamiltonian $\hat{H} = \hat{H}_0 + \hat{H}_{ee}$ of a system of electrons which has a single-particle term $\hat{H}_0$ that includes the influence of external fields and a two-particle term $\hat{H}_{ee}$ that accounts for the electron–electron interaction. In terms of quantum field operators it may be written as follows [47, 42, 43]

$$\begin{aligned} \hat{H} = &\sum_\sigma \int d\mathbf{x}\ \psi^\dagger(\mathbf{x}, \sigma) \left(\frac{\hat{p}^2}{2m} + V_0(\mathbf{x}) \right) \psi(\mathbf{x}, \sigma) + \\ &+ \frac{1}{2} \sum_{\sigma, \sigma'} \int d\mathbf{x} \int d\mathbf{x}'\ \psi^\dagger(\mathbf{x}, \sigma) \psi^\dagger(\mathbf{x}', \sigma') V_{\text{Coul}}(\mathbf{x}, \mathbf{x}') \psi(\mathbf{x}', \sigma') \psi(\mathbf{x}, \sigma) \end{aligned} \tag{2.5}$$

where the momentum operator reads as $\hat{p} = -i\vec{\nabla}$, $V_0(\mathbf{x})$ is an external potential and $V_{\text{Coul}}(\mathbf{x}, \mathbf{x}')$ accounts for the Coulomb interaction. Here and in the rest of the Chapter we make $\hbar = 1$.

Employing a discrete orthonormal single-particle basis, the single-particle term of the Hamiltonian can be written as

$$\hat{H}_0 = \sum_{jk} h_{jk} c_j^\dagger c_k \tag{2.6a}$$

$$h_{jk} = \sum_{\sigma} \int d\mathbf{x}\ \phi_j^\dagger(\mathbf{x}, \sigma) \phi_k(\mathbf{x}, \sigma) V_0(\mathbf{x}) \tag{2.6b}$$

and the two-particle term $\hat{H}_{ee}$ as

$$\hat{H}_{ee} = \frac{1}{2} \sum_{mjkl} V_{mjkl} c_m^\dagger c_j^\dagger c_k c_l \tag{2.7a}$$

$$V_{mjkl} = \sum_{\sigma\sigma'} \int d\mathbf{x} \int d\mathbf{x}'\ V_{\text{Coul}}(\mathbf{x}, \mathbf{x}') \phi_m^*(\mathbf{x}, \sigma) \phi_j^*(\mathbf{x}', \sigma') \phi_k(\mathbf{x}', \sigma') \phi_l(\mathbf{x}, \sigma) \tag{2.7b}$$

where use of Eqs. (2.3) has been made.

The Hamiltonian governs the dynamics of the system. In particular, the equation of motion for the quantum field operator $\psi(\mathbf{x}, \sigma, t)$ reads as [42, 49]

$$\left(i\frac{\partial}{\partial t} - \hat{h}_0(\mathbf{x}) \right) \psi(\mathbf{x}, \sigma, t) = \sum_{\sigma'} \int d\mathbf{x}'\ V_{\text{Coul}}(\mathbf{x}, \mathbf{x}') \hat{n}(\mathbf{x}', \sigma', t) \psi(\mathbf{x}, \sigma, t) \tag{2.8}$$

which is used in Sec. 2.5. We have defined $\hat{h}_0(\mathbf{x}) \equiv \hat{p}^2/2m + V_0(\mathbf{x})$ and the density operator $\hat{n}(\mathbf{x}', \sigma', t) \equiv \psi^\dagger(\mathbf{x}', \sigma', t)\psi(\mathbf{x}', \sigma', t)$. Here, $\psi^\dagger(\mathbf{x}, \sigma, t)$ and $\psi(\mathbf{x}, \sigma, t)$ are the time-dependent quantum field operators in the Heisenberg picture with respect to $\hat{H}$ [42]. Note that the equal-time anti-commutation relations given by Eqs. 2.4 do not apply in general to these operators for unequal times. A corresponding equation of motion exists for $\psi^\dagger(\mathbf{x}, \sigma, t)$.

2.3. Green's functions

Green's functions [40, 41, 42, 43, 44] are mathematical objects which are useful for evaluating physical properties of a many-body system, either in thermal equilibrium or under non-equilibrium conditions. They are quantum field correlation

functions expressed in terms of the expectation value of products of quantum field operators. One may define one-particle (two-point) Green's functions or in general, n-particle (2n-point) Green's functions.

To describe a non-equilibrium system, we focus on four different (but interrelated) one-particle Green's functions, which we term $G^<$, $G^>$, G^R and G^A. We consider also G^T, which is useful in equilibrium. Out of these Green's functions, which are defined in the following, only two are required in a stationary non-equilibrium situation and only one for equilibrium. Only Fermionic Green's functions are considered, since we are interested in describing electronic transport. Equivalent definitions exist for Bosonic systems. We abbreviate the spatial $\mathbf{x}$, spin σ and time t coordinates of the quantum field operators $\psi(\mathbf{x}, \sigma, t)$ and $\psi^\dagger(\mathbf{x}, \sigma, t)$, expressed in the Heisenberg picture [42], as $1 \equiv (\mathbf{x}_1, \sigma_1, t_1)$ and $2 \equiv (\mathbf{x}_2, \sigma_2, t_2)$.

The "lesser" Green's function is defined as

$$G^<(1,2) \equiv i \left\langle \psi^\dagger(2)\psi(1) \right\rangle \tag{2.9}$$

and provides information about the electron kinetics. The expectation value of any string $\hat{S}$ of operators is given by means of the statistical operator of the system $\hat{\rho}$ as $\left\langle \hat{S} \right\rangle = \mathrm{Tr}(\hat{\rho}\hat{S})$. If the system's preparation is pure ($\hat{\rho} = |\Phi\rangle \langle\Phi|$) as given by a single state $|\Phi\rangle$, we see that $G^<(1,2)$ is the probability amplitude for the many-body system to remain in the state $|\Phi\rangle$ after removing at time t_1 a particle with spin σ_1 at position $\mathbf{x}_1$ and restoring at time t_2 a particle with spin σ_2 at position $\mathbf{x}_2$. Equivalently, it may be interpreted as the amplitude for the process of removing a particle with coordinates 2 from state $|\Phi\rangle$ given a particle is removed at coordinates 1 from state $|\Phi\rangle$. For the case of a mixture, an additional statistical averaging over the distribution of initial states takes place. The "greater" Green's function is defined as

$$G^>(1,2) \equiv -i \left\langle \psi(1)\psi^\dagger(2) \right\rangle \tag{2.10}$$

which provides information about the hole kinetics.

Other two combinations of field correlations are of importance, namely, the

retarded Green's function

$$G^R(1,2) \equiv -i\theta(t_1 - t_2)\left\langle\{\psi(1), \psi^\dagger(2)\}\right\rangle = \theta(t_1 - t_2)\left(G^>(1,2) - G^<(1,2)\right) \tag{2.11}$$

and the advanced Green's function

$$G^A(1,2) \equiv i\theta(t_2 - t_1)\left\langle\{\psi(1), \psi^\dagger(2)\}\right\rangle = -\theta(t_2 - t_1)\left(G^>(1,2) - G^<(1,2)\right) \tag{2.12}$$

which contain information about the dynamics and spectral properties of the system. Here $\theta(t)$ is the Heaviside step function, which takes the following two values, $\theta(t < 0) = 0$ and $\theta(t \geq 0) = 1$.

As a Green's function that allows the construction of a systematic perturbation theory in equilibrium, the time-ordered or causal Green's function is defined as

$$G^T(1,2) \equiv -i\left\langle T\left(\psi(1)\psi^\dagger(2)\right)\right\rangle = \theta(t_1 - t_2)G^>(1,2) + \theta(t_2 - t_1)G^<(1,2) \tag{2.13}$$

where T is the time-ordering operator, which orders the operators in its argument according to the criterion that the operator with the earlier time is placed on the right

$$T(A(t_1)B(t_2)) = \theta(t_1 - t_2)A(t_1)B(t_2) - \theta(t_2 - t_1)B(t_2)A(t_1) \quad . \tag{2.14}$$

The anti-time-ordering operator $\widetilde{T}$ can also be defined, which orders oppositely to T.

These Green's functions satisfy the following relation

$$G^R(1,2) - G^A(1,2) = G^>(1,2) - G^<(1,2) \tag{2.15}$$

which is a combination that results in the spectral weight function

$$A(1,2) \equiv i(G^R(1,2) - G^A(1,2)) = \left\langle\{\psi(1), \psi^\dagger(2)\}\right\rangle = i(G^>(1,2) - G^<(1,2)). \tag{2.16}$$

$A(1,2)$ is essentially the imaginary part of the retarded Green's function, it determines the decay of the correlations in time domain and hence also the dissipation. It is important for obtaining the local density of states (LDOS) $\rho(\mathbf{x}, E)$ by Fourier transforming it from the time domain to the energy domain ($t_1 - t_2 \to E$) as

follows

$$\rho(\mathbf{x}, E) = \frac{1}{2\pi} A(\mathbf{x}, \mathbf{x}, E) \quad . \tag{2.17}$$

Furthermore, the following relations are satisfied

$$G^A(1,2) = \left(G^R(2,1)\right)^* \tag{2.18}$$

$$G^<(1,2) = -\left(G^<(2,1)\right)^* \tag{2.19}$$

$$G^>(1,2) = -\left(G^>(2,1)\right)^* \tag{2.20}$$

$$A(1,2) = (A(2,1))^* \quad . \tag{2.21}$$

Expressing the field operators in terms of a discrete single-particle orthonormal basis, as shown in Eqs. (2.3), the Green's functions become matrices

$$G^<_{jk}(t_1, t_2) = i \left\langle c^\dagger_k(t_2) c_j(t_1) \right\rangle \tag{2.22a}$$

$$G^>_{jk}(t_1, t_2) = -i \left\langle c_j(t_1) c^\dagger_k(t_2) \right\rangle \tag{2.22b}$$

$$G^R_{jk}(t_1, t_2) = -i\theta(t_1 - t_2) \left\langle \{c_j(t_1), c^\dagger_k(t_2)\} \right\rangle \tag{2.22c}$$

$$G^A_{jk}(t_1, t_2) = i\theta(t_2 - t_1) \left\langle \{c_j(t_1), c^\dagger_k(t_2)\} \right\rangle \quad . \tag{2.22d}$$

It can be shown [43] that for thermal equilibrium, the lesser Green's function $G^<$, which carries information about fluctuations, is proportional to the dissipative part as given by the spectral weight function A. This constitutes the fluctuation-dissipation theorem which, expressing these quantities in the energy domain, reads as

$$G^<(E) = i f(E) A(E) \tag{2.23}$$

where the proportionality factor is the probability of finding a particle (an occupied state) as given by the Fermi-Dirac distribution function

$$f(E) = \left(\exp\left(\frac{E - \mu}{k_B T} \right) + 1 \right)^{-1} \quad . \tag{2.24}$$

Here μ is the electrochemical potential of the system, k_B is Boltzmann's constant and T is the temperature. Similarly, for thermal equilibrium the following relation holds

$$G^>(E) = -i(1 - f(E)) A(E) \tag{2.25}$$

where the proportionality factor is the probability of finding a hole (an empty state).

A device with an applied bias voltage between the drain and source contacts is not in equilibrium, since the electrochemical potentials of the contacts, μ_S and μ_D, may be different. But the equilibrium expression for $G^<$ can be employed to describe the contacts themselves, which may be assumed to be in local equilibrium.

2.4. Contour-ordered Green's function

We may express the total Hamiltonian of the system as $\hat{H}(t) = \hat{H}_0 + \hat{H}_1(t)$, where $\hat{H}_0$ is a time-independent term that describes the isolated and/or non-interacting system and $\hat{H}_1(t)$ is a perturbation, that we consider time-dependent in general but which need not necessarily be so, as in the case of the electron–electron interaction. For an arbitrary observable $\hat{O}$, the connection between the Heisenberg picture with respect to $\hat{H}(t)$ and the Heisenberg picture with respect to $\hat{H}_0$ is given by [40, 42, 43]

$$\hat{O}_H(t) = \hat{U}_I^\dagger(t, t_0)\hat{O}_{H_0}(t)\hat{U}_I(t, t_0) \tag{2.26}$$

where the evolution operator $\hat{U}_I(t, t_0)$ for $t > t_0$ reads as

$$\hat{U}_I(t, t_0) = T\left(\exp\left(-i\int_{t_0}^{t} dt'\ \hat{H}_{1H_0}(t')\right)\right) \tag{2.27}$$

and for $t < t_0$ reads as

$$\hat{U}_I(t, t_0) = \widetilde{T}\left(\exp\left(-i\int_{t_0}^{t} dt'\ \hat{H}_{1H_0}(t')\right)\right) \quad . \tag{2.28}$$

The time-ordering operator T and the anti-time-ordering operator $\widetilde{T}$ were introduced in Sec. 2.3. The interaction Hamiltonian term in the Heisenberg picture with respect to $\hat{H}_0$ reads as

$$\hat{H}_{1H_0}(t) = \hat{U}_{H_0}^\dagger(t, t_0)\hat{H}_1(t)\hat{U}_{H_0}(t, t_0) \tag{2.29}$$

where

$$\hat{U}_{H_0}(t, t_0) = \exp\left(-i\hat{H}_0(t - t_0)\right) \quad . \tag{2.30}$$

For a system in its ground state ($\hat{\rho} = |\Phi\rangle\langle\Phi|$), one can obtain an expression for the time-ordered Green's function $G^T(1,2)$ ready for perturbation expansion. This is done by expressing the quantum field operators $\psi^\dagger(\mathbf{x},\sigma,t)$ and $\psi(\mathbf{x},\sigma,t)$ that appear in $G^T(1,2)$ by means of Eq. (2.26). By allowing the interaction to be switched on and off adiabatically and using the Gell-Mann and Low theorem, which relates the asymptotic state in the far future $|\Phi(\infty)\rangle$ with that in the far past $|\Phi(-\infty)\rangle$, $G^T(1,2)$ may be written in a form amenable to Wick's decomposition [50, 42].

But Gell-Mann and Low theorem does not hold in non-equilibrium situations, since then the states $|\Phi(\infty)\rangle$ and $|\Phi(-\infty)\rangle$ are not simply related and the time evolution as given by the general Hamiltonian $\hat{H}(t)$ is not adiabatic. Equilibrium theory cannot account for systems out of equilibrium [50].

Nevertheless, for $\hat{O}_H(t)$ as given by Eq. (2.26)

$$\hat{O}_H(t) = \widetilde{T}\left(\exp\left(i\int_{t_0}^{t} dt'\ \hat{H}_{1H_0}(t')\right)\right)\hat{O}_{H_0}(t)T\left(\exp\left(-i\int_{t_0}^{t} dt'\ \hat{H}_{1H_0}(t')\right)\right) \tag{2.31}$$

one can also perform a perturbative evaluation, by joining the exponential functions from the left and right of $\hat{O}_{H_0}(t)$ and introducing a time-ordering operator that recognizes whether the field operators belong to the time-ordered or anti-time-ordered parts of the product. This can be done by introducing a contour c running along the time axis, as shown in Fig. 2.1, and a contour ordering operator T_c. The time arguments $t(s)$ of the field operators are assigned to the contour, via a contour parameter s. We term the parts of the contour that run forward and backward in time as the $\overrightarrow{c}$-branch and the $\overleftarrow{c}$-branch, respectively, so that $c = \overrightarrow{c} + \overleftarrow{c}$. The T_c operator orders products of operators according to the position of their contour time argument on the closed contour, earlier contour time places an operator to the right. Reduced to the $\overrightarrow{c}$-branch or the $\overleftarrow{c}$-branch, T_c becomes the time-ordering T or the anti-time-ordering $\widetilde{T}$ operator respectively.

It can be shown [40, 42] that the two Heisenberg pictures, with respect to the total Hamiltonian $\hat{H}(t)$ and with respect to the Hamiltonian $\hat{H}_0$ of the isolated system, are connected in the following way

$$\hat{O}_H(t) = T_c\left(\exp\left(-i\int_c ds\ \hat{H}_{1H_0}(t(s))\right)\hat{O}_{H_0}(t)\right) \tag{2.32}$$

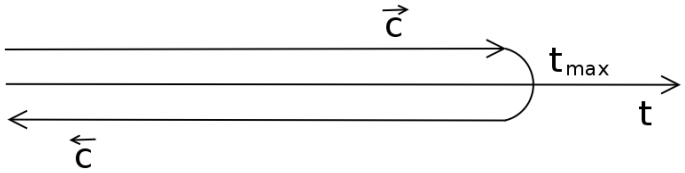

Figure 2.1.: The closed time path contour $c = \overrightarrow{c} + \overleftarrow{c}$. The branches are displaced from the time axis only for graphical purposes.

which follows from the fact that $T_{\overrightarrow{c}} = T$ and $T_{\overleftarrow{c}} = \widetilde{T}$, so

$$T_{\overrightarrow{c}}\left(\exp\left(-i\int_{\overrightarrow{c}} ds\ \hat{H}_{1H_0}(t(s))\right)\right) = \hat{U}_I(t,t_0) \tag{2.33a}$$

$$T_{\overleftarrow{c}}\left(\exp\left(-i\int_{\overleftarrow{c}} ds\ \hat{H}_{1H_0}(t(s))\right)\right) = \hat{U}_I^\dagger(t,t_0) \quad . \tag{2.33b}$$

The right hand side of Eq. (2.32) is in a form ready for a perturbative analysis, by a series expansion of the exponential.

The contour-ordered one-particle Green's function is defined as

$$G(\mathbf{x}_1,\sigma_1,s_1,\mathbf{x}_2,\sigma_2,s_2) \equiv -i\left\langle T_c\left(\psi(\mathbf{x}_1,\sigma_1,t(s_1))\psi^\dagger(\mathbf{x}_2,\sigma_2,t(s_2))\right)\right\rangle \tag{2.34}$$

where the field operators are expressed in the Heisenberg picture with respect to the total Hamiltonian $\hat{H}(t)$ of the system. Making the abbreviations $1 \equiv (\mathbf{x}_1,\sigma_1,t(s_1))$ and $2 \equiv (\mathbf{x}_2,\sigma_2,t(s_2))$ and by virtue of Eq. (2.32) it reads as

$$G(1,2) = -i\left\langle T_c\left(\exp\left(-i\int_c ds\ \hat{H}_{1H_0}(t(s))\right)\psi_{H_0}(1)\psi_{H_0}^\dagger(2)\right)\right\rangle \tag{2.35}$$

where the field operators are now expressed in the Heisenberg picture with respect to the Hamiltonian $\hat{H}_0$ of the isolated system. The contour runs up to the time $t_{\max} > t_1, t_2$ above the largest time argument of the Green's function.

One of the advantages of contour ordering compared to time ordering is that depending on the position of the times t_1 and t_2 on the contour, four possible combinations of Green's functions can be distinguished. Denoting a time t^+ as belonging to the $\overrightarrow{c}$-branch and a time t^- as belonging to the $\overleftarrow{c}$-branch of the contour, we have [51]

$$G^{++}(1,2) = G(\mathbf{x}_1,\sigma_1,t_1^+,\mathbf{x}_2,\sigma_2,t_2^+) = -i\left\langle T\left(\psi(1)\psi^\dagger(2)\right)\right\rangle \tag{2.36a}$$

$$G^{--}(1,2) = G(\mathbf{x}_1,\sigma_1,t_1^-,\mathbf{x}_2,\sigma_2,t_2^-) = -i\left\langle \widetilde{T}\left(\psi(1)\psi^\dagger(2)\right)\right\rangle \tag{2.36b}$$

$$G^{+-}(1,2) = G(\mathbf{x}_1,\sigma_1,t_1^+,\mathbf{x}_2,\sigma_2,t_2^-) = i\left\langle \psi^\dagger(2)\psi(1)\right\rangle \tag{2.36c}$$

$$G^{-+}(1,2) = G(\mathbf{x}_1,\sigma_1,t_1^-,\mathbf{x}_2,\sigma_2,t_2^+) = -i\left\langle \psi(1)\psi^\dagger(2)\right\rangle \tag{2.36d}$$

It can be shown [51] that these Green's functions are related to those introduced in Sec. 2.3, which are the ones employed for numerical implementations, as follows

$$G^<(1,2) = G^{+-}(1,2) \tag{2.37a}$$

$$G^>(1,2) = G^{-+}(1,2) \tag{2.37b}$$

$$G^R(1,2) = G^{++}(1,2) - G^{+-}(1,2) \tag{2.37c}$$

$$G^A(1,2) = G^{++}(1,2) - G^{-+}(1,2) \quad . \tag{2.37d}$$

2.5. Equations of motion for the Green's functions

In general, the contour-ordered n-particle Green's function is defined as

$$G_n(1,\ldots,n,1',\ldots,n') \equiv \frac{1}{i^n}\left\langle T_c\left(\psi(1)\cdots\psi(n)\psi^\dagger(n')\cdots\psi^\dagger(1')\right)\right\rangle \quad . \tag{2.38}$$

It can be shown [49] that these Green's functions satisfy the following equations of motion

$$\begin{aligned}&\left(i\frac{d}{ds_k} - \hat{h}_0(k)\right) G_n(1,\ldots,n,1',\ldots,n') = \\ &= -i\int d\bar{1}\; V_{\text{Coul}}(k;\bar{1}) G_{n+1}(1,\ldots,n,\bar{1},1',\ldots,n',\bar{1}^+) + \\ &+ \sum_{j=1}^{n}(-1)^{k+j}\delta(k;j') G_{n-1}(1,\ldots,\mathring{k},\ldots,n,1',\ldots,\mathring{j}',\ldots,n')\end{aligned} \tag{2.39}$$

where, among other considerations, use of the equation of motion for the field operator, Eq. (2.8), has been made. An analogous equation exists for the primed variables. Here, the arguments with a ring on top are absent from the argument list. Also, $\bar{1}^+ \equiv (\bar{\mathbf{x}}_1, \bar{\sigma}_1, \bar{t}(\bar{s}_1^+))$ indicates a contour argument infinitesimally larger than $\bar{t}(\bar{s}_1)$. As an example, only Coulomb interaction is considered. One could also take into account scattering or contact coupling.

This infinite set of coupled equations is known as the Martin-Schwinger hierarchy and shows that due to the interactions as given by the Coulomb term, the time dependence of a general n-particle Green's function is described in terms of lower-order and higher-order correlation functions. This makes the determination of the Green's functions problematic.

In the particular case of the contour-ordered one-particle Green's function, the equation of motion reads as

$$\left(i\frac{d}{ds_1} - \hat{h}_0(1)\right) G(1,1') = \delta(1,1') - i\int d2\; V_{\text{Coul}}(1,2)G_2(1,2,1',2^+) \quad (2.40)$$

where the zero-particle Green's function is defined as the identity. Furthermore, this equation can be rewritten in a convenient form by implicitly defining the self-energy Σ as [49]

$$\int d2\; \Sigma(1,2)G(2,1') = -i\int d2\; V_{\text{Coul}}(1,2)G_2(1,2,1',2^+) \quad . \quad (2.41)$$

Note that the right hand side of this definition is the second term on the right of Eq. (2.40). With this definition at hand, the equation of motion can be recast into a more useful form, known as Dyson equation [40, 42, 49]

$$G(1,1') = G_0(1,1') + \int d2 \int d3\; G_0(1,2)\Sigma(2,3)G(3,1') \quad (2.42)$$

where $G_0(1,1')$ is the free (without V_{Coul}) contour-ordered Green's function. Dyson equation provides a way to obtain G once Σ is known. Therefore the focus of the problem is shifted towards obtaining the self-energy, which can be a functional of the Green's function and contains everything that is not contained in G_0 (the "perturbation", like Coulomb interaction, scattering or contact coupling).

2.6. Non-equilibrium perturbation theory

The exponential appearing in Eq. (2.35) can be decomposed in a series expansion. This produces a sum of terms with an ever increasing number of products of interaction Hamiltonians under contour ordering. Under certain conditions on $\hat{H}_0$ and $\hat{\rho}$, Wick's theorem [42] provides the way for decomposing such averages over strings of field operators into products involving the free or equilibrium contour-

ordered Green's function

$$G_0(1,2) = -i\left\langle T_c\left(\psi_{H_0}(1)\psi^{\dagger}_{H_0}(2)\right)\right\rangle \quad . \tag{2.43}$$

The results of employing Wick's theorem to decompose the contributions from the expansion of the exponential containing the interaction are expressions with ever increasing complexity. However, by means of the diagrams invented by Feynman, it is possible to graphically depict and interpret the perturbative expressions, as well as to construct approximations and exact equations that may hold true beyond perturbation theory. One can argue in terms of Feynman diagrams to define the concept of self-energy and as a result, to arrive at Dyson equation [42, 44], alternatively to what was done in the previous Sec. 2.5.

2.7. Dyson equation

Defining the operator product $C = A * B$ as [51]

$$C(1,1') = \int d\mathbf{x}_2 \int_c dt_2 \; A(1,2)B(2,1') \tag{2.44}$$

that is, integration over space and contour, Dyson equation can be rewritten as

$$G = G_0 + G_0 * \Sigma * G \quad . \tag{2.45}$$

The following identities are obtained from the "$*$"-product definition [51]

$$C^{++} = A^{++} \cdot B^{++} - A^{+-} \cdot B^{-+} \tag{2.46a}$$
$$C^{--} = A^{-+} \cdot B^{+-} - A^{--} \cdot B^{--} \tag{2.46b}$$
$$C^{+-} = A^{++} \cdot B^{+-} - A^{+-} \cdot B^{--} \tag{2.46c}$$
$$C^{-+} = A^{-+} \cdot B^{++} - A^{--} \cdot B^{-+} \tag{2.46d}$$

where, for example, $C^{+-} = C(\mathbf{x}_1, \sigma_1, t_1^+, \mathbf{x}_2, \sigma_2, t_2^-)$ is a function with the first time argument in the forward branch and the second one in the backward branch of the contour. Here, we define the operator product $C = A \cdot B$ as

$$C(1,1') = \int d\mathbf{x}_2 \int_{-\infty}^{\infty} dt_2 \; A(1,2)B(2,1') \tag{2.47}$$

that is, integration over space and time. These identities are useful in order to write the Dyson equations for all the Green's functions, as made explicitly in the following [51]

$$G^{++} = G_0^{++} + G_0^{++}\Sigma^{++}G^{++} - G_0^{++}\Sigma^{+-}G^{-+} - G_0^{+-}\Sigma^{-+}G^{++} + G_0^{+-}\Sigma^{--}G^{-+} \quad (2.48a)$$

$$G^{--} = G_0^{--} + G_0^{-+}\Sigma^{++}G^{+-} - G_0^{-+}\Sigma^{+-}G^{--} - G_0^{--}\Sigma^{-+}G^{+-} + G_0^{--}\Sigma^{--}G^{--} \quad (2.48b)$$

$$G^{+-} = G_0^{+-} + G_0^{++}\Sigma^{++}G^{+-} - G_0^{++}\Sigma^{+-}G^{--} - G_0^{+-}\Sigma^{-+}G^{+-} + G_0^{+-}\Sigma^{--}G^{--} \quad (2.48c)$$

$$G^{-+} = G_0^{-+} + G_0^{-+}\Sigma^{++}G^{++} - G_0^{-+}\Sigma^{+-}G^{-+} - G_0^{--}\Sigma^{-+}G^{++} + G_0^{--}\Sigma^{--}G^{-+} \quad (2.48d)$$

where we have suppressed the "$\cdot$"-product symbol between operators for brevity.

For a time-invariant system for which G depends only on the time difference $\Delta t = t_1 - t_2$, it is possible to perform a Fourier transformation from time variables to the energy variable ($\Delta t \to E$). By means of it, the "$\cdot$"-product between time-dependent functions becomes a simple multiplication between energy-dependent functions, or matrices if the field operators are expressed using a discrete orthonormal single-particle basis, as Eqs. (2.22) show. We assume this in the following and explicitly write the Dyson equations for the retarded and lesser Green's functions, according to the expressions given by Eqs. (2.48)

$$G^R = G_0^R + G_0^R\Sigma^R G^R \quad (2.49a)$$

$$G^< = G^R\Sigma^< G^A + \left(1 + G^R\Sigma^R\right) G_0^< \left(1 + \Sigma^A G^A\right) \quad (2.49b)$$

with $G^A = G^{R\dagger}$. These energy-dependent matrix equations are the foundation of the non-equilibrium Green's function formalism (NEGF) for the non-equilibrium quantum kinetic simulation of nanoelectronic devices.

2.8. Hartree-Fock approximation of the self-energy

As Eq. (2.40) indicates, the determination of the contour-ordered one-particle Green's function $G(1, 1')$ depends explicitly on the contour-ordered two-particle Green's function $G_2(1, 2, 1', 2')$. It can be shown [49] that the approximation

$$G_2(1, 2, 1', 2') = G(1, 1')G(2, 2') - G(1, 2')G(2, 1') \quad (2.50)$$

satisfies the equations of motion for $G_2(1, 2, 1', 2')$ for the non-interacting case (with $V_{\text{Coul}}(1, 2) = 0$, so that the explicit dependence of G_2 on G_3 is absent).

This is the so-called Hartree-Fock approximation [49] to G_2, which indicates that, whenever the interaction between particles is weak, G_2 can be approximately expressed as the product of functions that describe how a single particle propagates when added to the system. Due to their indistinguishability, the anti-symmetrized version of the products appears in this approximation.

Substituting the Hartree-Fock approximation to G_2 in the implicit definition of the self-energy, Eq. (2.41), it follows that

$$\Sigma(1,2) = \delta(1,2)V_H(1) + iV_{\text{Coul}}(1,2)G(1,2^+) \quad . \tag{2.51}$$

Here, the Hartree potential V_H is identified with

$$V_H(1) = -i\int d3\; V_{\text{Coul}}(1,3)G(3,3^+) = \int d\mathbf{x}_3 V_{\text{Coul}}(\mathbf{x}_1,\mathbf{x}_3)n(\mathbf{x}_3,t(s_1)) \tag{2.52}$$

where $n(\mathbf{x}_3,t(s_1)) = -iG(\mathbf{x}_3,\sigma_3,t(s_1),\mathbf{x}_3,\sigma_3,t(s_1^+))$ is the particle density. The Hartree potential can be understood as the classical potential that a particle experiences from a density distribution of all the particles of the system. The second term in $\Sigma(1,2)$ is called the Fock or exchange potential, which is local in time but non-local in space and cannot be interpreted as a classical potential.

The Hartree-Fock approximation neglects the direct interaction between two particles, a single particle moves like a free particle under the influence of an effective potential dependent on the position of the rest of the particles. This is the idea of a mean-field approximation.

Written in terms of the single-particle density matrix (in the position basis)

$$\begin{aligned}\rho_1(\mathbf{x}_1,\sigma_1,\mathbf{x}_2,\sigma_2,t(s)) &\equiv \left\langle \psi^\dagger(\mathbf{x}_2,\sigma_2,t(s))\psi(\mathbf{x}_1,\sigma_1,t(s))\right\rangle = \\ &= -iG(\mathbf{x}_1,\sigma_1,t(s),\mathbf{x}_2,\sigma_2,t(s^+))\end{aligned} \tag{2.53}$$

the self-energy reads as

$$\Sigma(1,2) = \delta(1,2)\int d3\; V_{\text{Coul}}(1,3)\rho_1(3,3) - V_{\text{Coul}}(1,2)\rho_1(1,2) \quad . \tag{2.54}$$

Changing the representation from the continuous position basis to a discrete single-particle basis $\{\phi_k(\mathbf{x})\}$ (of localized spin/site orbitals, for example), the quantum field operators change according to Eqs. (2.3). Therefore, the quantities

that depend directly on these operators change according to

$$\Sigma(1,2) = \sum_{kl} \phi_k(\mathbf{x}_1)\phi_l^*(\mathbf{x}_2)\Sigma_{kl} \tag{2.55}$$

$$\rho_1(1,2) = \sum_{kl} \phi_k(\mathbf{x}_1)\phi_l^*(\mathbf{x}_2)\rho_{1kl} \tag{2.56}$$

which appear in the expression for the self-energy. Substituting these quantities into Eq. (2.54), multiplying both sides of this expression with $\phi_i^*(\mathbf{x}_1)\phi_j(\mathbf{x}_2)$, integrating with respect to $\mathbf{x}_1$ and $\mathbf{x}_2$ and taking into account the form of the tensor elements for the interaction Hamiltonian as expressed by Eq. (2.7b), it is straightforward to prove that the self-energy can be written in the discrete basis as [45]

$$\Sigma_{ij} = \sum_{kl} (V_{ilkj} - V_{likj})\rho_{1kl} \quad . \tag{2.57}$$

Here, the first term represents the Hartree potential, whereas the second term represents the Fock or exchange potential.

2.9. NEGF schemes

Several NEGF schemes can be distinguished depending on the treatment given to the Hamiltonian and to the Green's function. Usually, in the following approaches a suitable coordinate system adapted to the symmetry of the device is employed. One of the coordinate axis coincides with the longitudinal propagation direction, while the rest of the axes are perpendicular to it, defining adjacent "slices". The Hamiltonian is discretized in space and together with the considered self-energy matrices can be used to obtain the Green's functions, from which the charge density can be obtained. This charge density determines the electrostatic potential in the device by means of solving Poisson's equation. The potential is input to the Hamiltonian and a self-consistent algorithm is thus defined. This algorithm is known as Schrödinger-Poisson solver and employs a Hartree mean-field approximation to electronic interaction, thus being unable to describe few-electron charging effects.

In the real space NEGF simulation scheme [52], the Hamiltonian, usually in the effective mass approximation, is discretized in real space. Its matrix representation in a suitable chosen basis is given by a block diagonal matrix, composed in turn

of block diagonal submatrices. One can distinguish two kinds of submatrices, namely, those which couple space points within each slice and depend both on site coupling energies and on the potential within the slice, and those which couple adjacent slices and depend only on site coupling energies. To obtain the retarded Green's function, the effective Hamiltonian matrix for each energy has to be inverted. Since there is no restriction on the solution domain, this approach is computationally expensive.

Within the real space representation, several methods exist which reduce the computational cost of the NEGF calculations. The recursive Green's function method [53, 54, 55] performs well for two-terminal devices that can be discretized into cross-sectional slices with nearest neighbor interaction. On the other hand, it finds difficulties dealing with additional contacts that imply more neighbors to be considered. The contact block reduction method [56, 57, 58] decomposes the retarded Green's functions into four blocks. One of the blocks concerns the contacts, a second one concerns the decoupled device and the last two the coupling between contacts and device. Focus lies on solving only for the contact and the contact-device submatrices, those blocks necessary to obtain various electronic observables such as the transmission coefficient. Only the contact self-energies are considered. The corresponding reduced Dyson equation's size is given by the size of the contact regions only, implying calculations are reduced in number. This method produces good results in the ballistic regime for multiterminal devices with an arbitrary geometry, potential profile and number of contacts. On the other hand, it does not describe incoherent scattering.

The mode space NEGF simulation scheme [59, 60] separates the confinement in the transversal directions form the longitudinal propagation direction. Schrödinger's equation is solved within each transversal slice for all points along the longitudinal direction. The resulting wave functions, together with those corresponding to the longitudinal direction, form a basis with which to represent the Hamiltonian. The resulting transversal energies form subbands that depend on the position along the transport direction and enter into the Hamiltonian matrix, which is in this case a 1D quantity. Knowing the Hamiltonian for each subband, the retarded Green's function can be readily obtained. Note that in mode space representation, the transport is reduced to 1D, in contrast to the real space representation. In the case of a thin channel FET, strong electron quantum con-

finement produces a large energy separation between modes, so only the lowest modes are populated. This, together with the reduced size of the mode space Hamiltonian, implies that calculations in this scheme are lighter without loss in accuracy as compared to a real space scheme, which implicitly treats all modes.

Two approaches can be employed within the mode space NEGF simulation scheme. The uncoupled mode space representation [52, 59, 61, 62] neglects subband coupling, which produces good results as long as the transverse potential profile along the longitudinal axis remains uniform. The mode coupling occurs where the transversal energy does not change gradually along the transport direction. One then has to consider subband coupling and employ the coupled mode space representation [59, 60, 63, 64].

These NEGF simulation schemes have been successfully applied to simulate electronic transport in NWFETs. Recently there has been a great interest in studying the variability of these devices due to discrete dopants and surface roughness. With channel lengths and diameter below the micrometer scale, the characteristics of a nanoscale FET become sensitive to minute variations in the distribution of individual doping atoms [65, 66, 67, 68, 69, 70, 71] or deviation from perfectly smooth surfaces [72, 73, 74, 75]. Therefore, simulation of these effects has been useful to understand the impact they have on the performance and variability of these devices. Usually a 3D real space NEGF scheme is needed to account for these inhomogeneities. Furthermore, few-electron charging is not considered within the mean-field Hartree-Fock approximation described above. A many-body treatment is needed which will be addressed in the next chapter.

3. Multi-configurational self-consistent Green's function method

3.1. Introduction

The number of electrons involved in the operation of NWFETs with channel lengths as large as $\sim$ 100 nm is on the order of 1–10. Therefore single-electron charging effects are important and an electronic transport model at these scales must be able to describe them. This implies that such a model must take into account the Coulomb interaction between electrons in a many-body description.

On the one hand, a NEGF approach to electronic transport in a NWFET describes non-equilibrium states very well but the Coulomb interaction is typically modeled in terms of a self-consistent mean-field Hartree potential, which does not account for single-electron charging effects. On the other hand, a full many-body formulation of the Coulomb interaction correctly predicts these effects at the expense of considering only a small number of single-particle states, since the dimension of the many-body Fock space increases exponentially with this number.

The multi-configurational self-consistent Green's function (MCSCG) method [45, 46] is an hybrid approach to the simulation of ultimately scaled NWFETs that benefits both from the NEGF formalism to describe non-equilibrium electronic transport and from the many-body Coulomb interaction formulation for a special small set of adaptively chosen relevant states. For the rest of the states the interaction is treated in a conventional mean-field way. The Fock space description allows for the calculation of few-electron Coulomb charging effects beyond mean-field. With the MCSCG method, Coulomb blockade effects are correctly described for low enough temperatures, while under strong non-equilibrium and

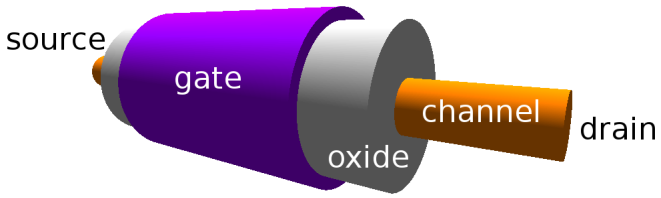

Figure 3.1.: Schematic view of a 1D NWFET geometry.

high temperatures the method retains a mean-field Hartree-Fock approximation which produces an adequate description of Coulomb interaction.

3.2. The system

A NWFET features a nanowire channel that can be considered almost 1D, since for diameters ~ 10 nm only a few or even a single radial mode participate in the current. Therefore, the model describes the channel as a 1D nanowire of length L, diameter d_{ch} and relative dielectric constant $\varepsilon_{\mathrm{ch}}$. In the following we consider a coaxially gated NWFET, as illustrated in Fig. 3.1. Channel (orange color) and gate electrode (purple color) are isolated by the presence of an oxide (gray color) with thickness d_{ox} and relative dielectric constant $\varepsilon_{\mathrm{ox}}$. The two extremes of the channel are contacted by source and drain, which can be considered to be either Ohmic contacts or deposited metallic electrodes forming two Schottky barriers. The system is at a temperature T.

3.3. Theoretical elements of the method

What distinguishes the MCSCG approach is its ability to describe few-electron charging effects for realistic NWFETs out of equilibrium, based on an hybrid approach that combines both many-body Fock space and mean-field descriptions of electron–electron Coulomb interaction. Details of its fundamental characteristic features are given in Sec. 3.4 but first we present in the following sections the theoretical elements the MCSCG method makes use of, which may be common to other non-equilibrium electronic transport simulation approaches.

3.3.1. Coulomb Green's function

The electrostatic potential $V(x)$ inside the 1D nanowire channel obeys a modified Poisson equation [27, 76]

$$\frac{\partial^2 V(x)}{\partial x^2} - \frac{1}{\lambda^2} V(x) = -\frac{\rho(x)}{\varepsilon_0 \varepsilon_{\mathrm{ch}} S} - \frac{1}{\lambda^2} V_{\mathrm{G}} \tag{3.1}$$

where $\rho(x)$ is the 1D charge density, V_{G} is the gate potential and $S = \pi d_{\mathrm{ch}}^2/4$ is the effective cross-sectional area. The screening length λ, which should be $\lambda \ll L$ to avoid short-channel effects [26], is given by Eq. (1.1) for a coaxial transistor geometry.

Given $\rho(x)$, Eq. (3.1) can be solved by means of a Green's function which we term Coulomb Green's function and constitutes an important ingredient in the formalism. It describes the charge interaction within the channel and enables the formulation of classical electrostatics and the many-body interaction between electrons on equal footing. It can be obtained as [45]

$$v(x,x') = \frac{\lambda}{2}\left(e^{-\frac{|x-x'|}{\lambda}} - e^{-\frac{x+x'}{\lambda}}\right) + \frac{\lambda}{2} e^{-\frac{L}{\lambda}} \left(\frac{\cosh\left(\frac{x-x'}{\lambda}\right)}{\sinh\left(\frac{L}{\lambda}\right)} - \frac{\cosh\left(\frac{x+x'}{\lambda}\right)}{\sinh\left(\frac{L}{\lambda}\right)} \right) \tag{3.2}$$

with $0 \leq x, x' \leq L$ and vanishing potential at the boundaries $V(0) = V(L) = 0$. The potential for a given charge density $\rho(x)$ inside the channel thus reads as [77]

$$V(x) = \frac{1}{\varepsilon_0 \varepsilon_{\mathrm{ch}} S} \int dx' \; v(x,x') \rho(x') + V_{\mathrm{ext}}(x) \tag{3.3}$$

with the external potential contribution

$$V_{\mathrm{ext}}(x) = \frac{\sinh\left(\frac{L-x}{\lambda}\right)}{\sinh\left(\frac{L}{\lambda}\right)} V_{\mathrm{S}} + \frac{\sinh\left(\frac{x}{\lambda}\right)}{\sinh\left(\frac{L}{\lambda}\right)} V_{\mathrm{D}} + \frac{1}{\lambda^2} \int dx' \; v(x,x') (V_{\mathrm{G}}(x') + V_{\mathrm{dop}}(x')) \tag{3.4}$$

which stems from external charges due to the applied drain–source voltage, the gate and doping influences. Here V_{S} and V_{D} denote the source and drain contact potentials respectively, $V_{\mathrm{G}}(x)$ is a position dependent gate potential and $V_{\mathrm{dop}}(x)$ denotes the potential resulting from fixed charges due to ionized doping atoms.

3.3.2. Localized single-particle basis

According to Ref. [78], InP has a molecular density $\rho_m = 1.979 \times 10^{22}$ cm^{-3} or expressed in nanometers, an atomic density $\rho_a = 39.58$ nm^{-3}. Considering an InP cylindrical nanowire channel with diameter $d_{\text{ch}} = 20$ nm and length $L = 100$ nm it is easy to verify, just by multiplying its volume by ρ_a, that the number of atoms that make this nanowire is around $N_a \simeq 1.24 \times 10^6$. To feasibly address the mathematical description of such a large number of elements one needs a simplification.

In this model, this simplification consists of considering a one-band tight-binding description of the NWFET channel in the effective mass approximation. It is represented by a localized 1D single-particle basis $\{\phi_i(x,\sigma)\}$ with $N_{\text{max}} = 2 \times N_{\text{sites}}$ spin orbitals, where the factor 2 stems from considering spin and N_{sites} is the number of spatial sites.

Taking again the previous InP example, whose lattice constant is $a_0 = 5.87$ Å, this model would need a number of localized orbitals or sites $N_{\text{sites}} = L/a_0 \simeq 170$. This number is much smaller than the number of atoms N_a in a realistic InP nanowire. Nevertheless, the model produces results that agree with experimental observations.

3.3.3. Hamiltonian

The total system Hamitonian $\hat{H} = \hat{H}_0 + \hat{H}_{ee} + \hat{H}_{\text{S}} + \hat{H}_{\text{D}}$ in the localized orbital basis can be split into four parts. $\hat{H}_0$ contains all single-particle terms of the transistor channel, with matrix elements h_{ij} which read as

$$\hat{H}_0 = \sum_{i,j=0}^{N_{\text{max}}-1} h_{ij}\ \hat{c}_i^\dagger \hat{c}_j \tag{3.5a}$$

$$h_{ij} = -e \sum_\sigma \int dx\ \phi_i^*(x,\sigma)\phi_j(x,\sigma)V_{\text{ext}}(x) + \delta_{ij} d_i + t_{ij} \tag{3.5b}$$

where $\hat{c}_i^\dagger$ and $\hat{c}_j$ are Fermionic creation and annihilation operators respectively, expressed in the single-particle localized spin/site basis, d_i and t_{ij} are the diagonal and the hopping matrix elements respectively, arising from tight-binding [41].

The many-body Coulomb interaction between electrons within the channel region is described by a two-particle term $\hat{H}_{ee}$ with Coulomb tensor elements V_{ijkl}

as follows

$$\hat{H}_{ee} = \frac{1}{2}\sum_{i,j,k,l=0}^{N_{\max}-1} V_{ijkl}\ \hat{c}_i^\dagger \hat{c}_j^\dagger \hat{c}_k \hat{c}_l \tag{3.6a}$$

$$V_{ijkl} = \frac{e^2}{\varepsilon_0 \varepsilon_{ch} S}\sum_{\sigma,\sigma'}\int dx \int dx'\ v(x,x')\phi_i^*(x,\sigma)\phi_j^*(x',\sigma')\phi_k(x',\sigma')\phi_l(x,\sigma). \tag{3.6b}$$

That the Coulomb tensor elements can be expressed by means of the Coulomb Green's function given by Eq. (3.2) can be seen by considering the classical expression for the Coulomb interaction energy of a charge distribution $\rho(x)$ and its potential $V(x)$

$$E_{ee} = \frac{1}{2}\int dx\ \rho(x)V(x) \tag{3.7}$$

where the potential is given through the Coulomb Green's function as follows

$$V(x) = \frac{1}{\varepsilon_0 \varepsilon_{\text{ch}} S}\int dx'\ v(x,x')\rho(x') \tag{3.8}$$

resulting in an equation

$$E_{ee} = \frac{1}{2\varepsilon_0 \varepsilon_{\text{ch}} S}\int dx \int dx'\ \rho(x)v(x,x')\rho(x') \tag{3.9}$$

which has Eqs. (3.6a) and (3.6b) associated as quantum operator and tensor elements, respectively, in the multi-particle space.

3.3.4. Single-particle density matrix and natural orbital basis

The single-particle density matrix [79] ρ_1 of the system in the localized orbital basis can be obtained from the lesser Green's function as follows

$$\rho_{1jk} = \frac{1}{2\pi i}\int dE\ G_{kj}^{<}(E) \quad . \tag{3.10}$$

Its dimensions are $N_{\max} \times N_{\max}$. The eigenvectors of ρ_1 are known as natural orbitals and its eigenvalues ξ_i can be interpreted as average occupation numbers of the natural orbitals [79, 80]. They satisfy $0 \leq \xi_i \leq 1$. Υ is the unitary transformation matrix that diagonalizes ρ_1, such that $\rho_1^{\text{diag}} = \Upsilon^\dagger \rho_1 \Upsilon$ is the single-particle density matrix in diagonal form, and gives the transformation between

natural orbital basis and spin/site basis. The natural orbitals are represented by the columns of Υ.

Note that the index ordering criterion in Eq. (3.10) influences the expression of the Coulomb self-energy as given by Eq. (3.16), to be compared to Eq. (2.57).

3.3.5. NEGF description

A quantum dynamical description of the many-body non-equilibrium state of the NWFET is obtained by means of the real-time NEGF formalism, as introduced in Chapter 2. The two-point retarded and lesser Green's functions in the time domain are given by

$$\begin{aligned} G^R_{jk}(t) &= -i\theta(t)\left\langle \left\{ c_j(t), c_k^\dagger(0) \right\} \right\rangle \\ G^<_{jk}(t) &= i\left\langle c_k^\dagger(0) c_j(t) \right\rangle \end{aligned} \tag{3.11}$$

for steady-state conditions, where the Green's functions depend only on the time difference $\Delta t = t - t'$ and we have chosen $t' = 0$. We consider the Fourier transformed functions defined as

$$G(E) = \frac{1}{\hbar}\int dt\ e^{\frac{i}{\hbar}Et} G(t) \tag{3.12}$$

and work in the energy domain. The Green's functions satisfy the following Dyson equations for the channel

$$\begin{aligned} G^R &= G_0^R + G_0^R \Sigma^R G^R \\ G^< &= G^R \Sigma^< G^A + (1 + G^R \Sigma^R) G_0^< (\Sigma^A G^A + 1) \end{aligned} \tag{3.13}$$

where the Green's functions G and self-energies Σ are matrices in the localized spin/site representation, $G_0^R \equiv (E - h + i\varepsilon)^{-1}$ with $\varepsilon \to 0^+$ is the equilibrium retarded Green's function and $G^A = G^{R\dagger}$ is the advanced Green's function. We assume $G_0^< \equiv 0$, which means that the channel remains empty without contacts.

For temperatures T well above the Kondo temperature of the system, the Coulomb interaction can be treated independently of the contact coupling. Within this approximation, the total self-energy $\Sigma = \Sigma_{ee} + \Sigma_S + \Sigma_D$ can be written as a sum of a Coulomb interaction term Σ_{ee} and two contact terms Σ_S and Σ_D of a non-interacting form, due to the coupling of the channel to the source and drain

regions ($c = \mathrm{S}, \mathrm{D}$), which in matrix form read as [45]

$$\Sigma^R_{c_{jk}}(E) = \sum_{p,q \in c} t_{c_{jp}} G^R_{0c_{pq}}(E) t_{c_{qk}} \tag{3.14}$$

with the isolated contact Green's function G^R_{0c} and contact-channel hopping terms t_c. The corresponding lesser self-energy is given by [45]

$$\Sigma^<_c = i f_c \Gamma_c \tag{3.15}$$

where $\Gamma_c \equiv i(\Sigma^R_c - \Sigma^A_c)$. The local source and drain Fermi distribution functions are represented by f_S and f_D respectively, assuming local equilibrium within the reservoirs.

The Coulomb self-energy is obtained as a first-order expansion, represented by the Hartree-Fock diagrams, where the four-point Green's functions are factorized into linear combinations of products of two-point functions. Using this approximation, it reads as [45]

$$\Sigma^R_{ee_{ml}} = \sum_{j,k=0}^{N_\mathrm{max}-1} (V_{mjkl} - V_{jmkl})\, \rho_{1jk} \quad . \tag{3.16}$$

3.4. The MCSCG method: fundamental features

So far we have described a NEGF approach to electronic transport with a mean-field approximation to Coulomb interaction. On the one hand, for integer-number electron filling conditions such an approximation can be employed to obtain a good description of the system for application relevant temperatures. On the other hand, under non-equilibrium conditions, implying non-integer average filling situations, a first-order mean-field self-energy does not produce a good description in general. In this section we describe the fundamental characteristic features that define the MCSCG approach [45, 46], which is able to cope with such particle number fluctuations.

3.4.1. Relevant states and relevant Fock subspace

In the following, the natural orbital basis is used as single-particle basis and we express all the relevant quantities using this basis.

Given that the natural orbital basis has N_{max} states, the resulting many-body Fock space $\mathcal{F}$ has dimension $\dim(\mathcal{F}) = 2^{N_{\text{max}}}$. The set of all Slater determinants of natural orbitals constitute a basis of the whole Fock space, corresponding to states with well defined occupation (0 or 1) of single-particle basis states for the chosen basis of natural orbitals. Thus, a Slater determinant $|D_K\rangle \in \mathcal{F}$ can be uniquely identified in the occupation number representation by a vector of N_{max} bits $b_i \in \{0, 1\}$ of the form $|D_K\rangle = |b_0 b_1 \cdots b_{N_{\text{max}}-1}\rangle$ and an index $K = 0, \ldots, 2^{N_{\text{max}}} - 1$, which is the corresponding integer representation of the binary sequence.

To make calculations of realistic nanowire devices numerically feasible, instead of considering the full Fock space, we restrict ourselves to a relevant subspace $\mathcal{F}_{\text{rel}}$ as spanned by a relevant many-body basis $\mathcal{B}_{\text{rel}}$. The Slater determinants (also known as configurations) $|D_K\rangle \in \mathcal{B}_{\text{rel}}$ are constructed as follows. There are as many Slater determinants as possible bit combinations of zeros and ones (empty and occupied single-particle states) of the N_{rel} relevant natural orbitals. Here "relevant" means fluctuating ($0 < \xi_i < 1$, with given thresholds) and weakly coupled to the contacts, that is, resonantly trapped, quasibound electrons (the magnitude of the imaginary part of the contact coupling self-energy is below a given threshold), thus being responsible for few electron Coulomb charging effects. Thus the dimension of the relevant Fock subspace is $\dim(\mathcal{F}_{\text{rel}}) = 2^{N_{\text{rel}}}$.

The main idea of the method is to treat the electron–electron Coulomb interaction of the N_{rel} relevant states and their contribution to the Coulomb self-energy Σ^R_{ee} in a many body multi-configurational manner within the relevant Fock subspace $\mathcal{F}_{\text{rel}}$. The N_{rest} rest of the natural orbitals (those occupied with $\xi_i \simeq 1$, those empty with $\xi_i \simeq 0$ or those fluctuating but strongly coupled) are kept empty in every $|D_K\rangle$ and treated in a mean-field way.

As an example, for $N_{\text{max}} = 100$ the dimension of the full Fock space is $\dim(\mathcal{F}) \simeq 1.27 \times 10^{30}$, making a full many-body approach to electron–electron interaction unfeasible for typical lengths of the NWFET. On the other hand if only $N_{\text{rel}} = 6$ natural orbitals are relevant then the dimension of the relevant Fock subspace is $\dim(\mathcal{F}_{\text{rel}}) = 64$ and the many-body approach is rendered feasible.

3.4.2. Statistical operator

Once the relevant single-particle states have been identified and the relevant Fock subspace accordingly constructed, the state of the system is described by a projected many-body statistical operator

$$\hat{\rho}_{\text{rel}} = \sum_{K=0}^{2^{N_{\text{rel}}}-1} w_K \left|D_K\right\rangle \left\langle D_K\right| \tag{3.17}$$

whose eigenbasis is given by the set of relevant Slater determinants of natural orbitals. The eigenvalue or weight $w_K \in [0,1]$ can be interpreted as the probability associated with the Slater determinant or configuration $|D_K\rangle \in \mathcal{B}_{\text{rel}}$. The statistical operator is Hermitian and satisfies $\text{Tr}(\hat{\rho}_{\text{rel}}) = \sum_K w_K = 1$.

For each configuration $|D_K\rangle = |b_0 b_1 \cdots b_{N_{\text{rel}}-1}\rangle$ with $b_n \in \{0,1\}$, a corresponding single-particle density matrix ρ_{1K} can be derived from ρ_1 as follows

$$\rho_{1K} = \sum_{n\in\text{Rel}} b_n \left|\phi_n\right\rangle \left\langle\phi_n\right| + \sum_{n\notin\text{Rel}} \xi_n \left|\phi_n\right\rangle \left\langle\phi_n\right| \tag{3.18}$$

where $|\phi_n\rangle$ and ξ_n are respectively the single-particle eigenstates and eigenvalues of ρ_1. The matrix expression of ρ_{1K} in the localized orbital basis has elements

$$\rho_{1K_{ij}} = \sum_{n\in\text{Rel}} b_n \Upsilon^*_{jn} \Upsilon_{in} + \sum_{n\notin\text{Rel}} \xi_n \Upsilon^*_{jn} \Upsilon_{in} \tag{3.19}$$

with Υ the unitary transformation matrix that diagonalizes ρ_1.

These individual single-particle density matrices define, through Eq. (3.16), a set of Coulomb self-energies $\Sigma^r_{ee}[\rho_{1K}]$ that we assume become adequate for each configuration. Since the Green's functions are calculated as expectation values and these are given by the statistical operator, one can write the Green's function as a configuration average

$$\overline{G} = \sum_{K=0}^{2^{N_{\text{rel}}}-1} w_K G[\rho_{1K}] \tag{3.20}$$

where $G[\rho_{1K}]$ is the corresponding Green's function (retarded and lesser) that is obtained by using Eq. (3.13) with an individual $\Sigma^r_{ee}[\rho_{1K}]$.

In Chapter 4 we describe a method to numerically determine the relevant sta-

tistical operator of the NWFET system employing both the eigenbasis of Slater determinants of natural orbitals and an alternative eigenbasis. These results are used to extend the MCSCG algorithm, as a new implementation known as **NWFET-Lab** (see Appendix A).

3.4.3. Mean-field interaction

We can include in the total system Hamiltonian $\hat{H}$ a single-particle term which describes the mean-field interaction of relevant single-particle states with the non-relevant. In the localized orbital basis it reads as

$$\hat{H}_{ee}^{\text{ext}} = \sum_{i,j=0}^{N_{\max}-1} \Sigma_{ee_{ij}}^{R}[\hat{\rho}_{1\text{vac}}]\hat{c}_i^{\dagger}\hat{c}_j \tag{3.21}$$

where the Coulomb self-energy $\Sigma_{ee}^{R}[\hat{\rho}_{1\text{vac}}]$ is given Eq. (3.16) with a particular $\hat{\rho}_{1\text{vac}}$, which is the single-particle density matrix for the vacuum state within $\mathcal{F}_{\text{rel}}$. This state is the Slater determinant with all relevant single-particle states empty (bits set to 0). $\hat{\rho}_{1\text{vac}}$ can be obtained from its diagonal form $\rho_{1\text{vac}_{ij}}^{\text{diag}} = \delta_{ij}\xi_i^{\text{vac}}$ by assuming all relevant single-particle states have an average occupation number $\xi_i^{\text{vac}} = 0$ (vacuum state within $\mathcal{F}_{\text{rel}}$) and the non-relevant have their actual values $\xi_i^{\text{vac}} = \xi_i$. Performing an inverse transformation we obtain a non-diagonal single-particle density matrix for the vacuum state $\hat{\rho}_{1\text{vac}} = \Upsilon\rho_{1\text{vac}}^{\text{diag}}\Upsilon^{\dagger}$.

3.4.4. Determination of the weigths

We consider a vector **w** of weights that describes a probability distribution that maximizes the entropy under the subsidiary condition that $\rho_1 = \sum_K w_K\rho_{1K}$. With this approximation we obtain

$$w_K = \frac{1}{Z}\exp\left(-\frac{1}{k_B T}\left(E_K - \sum_{i=0}^{N_{\text{rel}}-1}\mu_i N_i(|D_K\rangle)\right)\right) \tag{3.22}$$

where Z is a normalization constant, k_B is Boltzmann's constant and T is the temperature. $N_i(|D_K\rangle)$ denotes the occupation number (0 or 1) of the relevant single-particle state i for the configuration $|D_K\rangle$ and μ_i represents an individual electrochemical potential, that is a Lagrange parameter for the subsidiary condition above and can be obtained with the help of a Newton iteration scheme.

0.	Start with a given ρ_1
1.	Diagonalize ρ_1 and select relevant single-particle states
2.	Obtain matrices ρ_{1K} from ρ_1 for all configurations K of relevant states
3.	Obtain $G^R[\rho_{1K}]$ from Dyson equation with Hartree-Fock $\Sigma^R_{ee}[\rho_{1K}]$, $\forall K$
4.	Obtain $G^<[\rho_{1K}]$ from Dyson equation with $G^R[\rho_{1K}]$, $\forall K$
5.	Determine configuration weight vector $\mathbf{w}$
6.	Calculate averages $G^R = \sum_K w_K G^R[\rho_{1K}]$ and $G^< = \sum_K w_K G^<[\rho_{1K}]$
7.	Obtain new ρ_1 via numerical integration of $G^<(E)$ over E
8.	Loop back to step 1 until convergence
9.	Calculate observables

Table 3.1.: The MCSCG algorithm

The energy E_K of the relevant Slater determinant $|D_K\rangle$ is given by the diagonal matrix elements of the projected many-body Hamiltonian $\hat{H}_{\text{rel}}$ within the relevant Fock subspace $\mathcal{F}_{\text{rel}}$, which is obtained from $\hat{H}$ via projection to the relevant Fock subspace $\mathcal{F}_{\text{rel}}$ and whose components read as $H_{\text{rel}_{IJ}} = \langle D_I | \hat{H}_0 + \hat{H}_{ee} + \hat{H}^{\text{ext}}_{ee} | D_J \rangle$ so that $E_K = H_{\text{rel}_{KK}}$. Note that the configurations, as Slater determinants, might not be exact eigenstates of $\hat{H}_{\text{rel}}$. Later on (Chapter 4) we generalize the concept of configuration as general many-body state.

3.4.5. Self-consistency algorithm

A self-consistency algorithm, the so-called MCSCG algorithm, can be defined by taking the average $\overline{G}^<$ from Eq. (3.20) for the obtained set of weights $\mathbf{w}$ as new $G^<$, for a whole new iteration step of the calculation scheme defined in the previous sections. Convergence is achieved when the mean change in the occupation numbers ξ_i of the natural orbitals (eigenvalues of ρ_1) between two consecutive iterations is below a chosen threshold. We provide a view of the implementation of the MCSCG algorithm in Table 3.1.

3.5. Software implementation

The MCSCG algorithm has been implemented in two consecutive software versions. The earliest version, named **whiskersim** [81], implements the algorithm described in the previous sections and summarized in Table 3.1. As a main ob-

jective of this dissertation, a second version, named **NWFET-Lab** [82], has been implemented, which includes and extends the previous version. In contrast to the earliest version, which is console-based, the second version has a graphical user interface. It can additionally perform calculations in a parallel, multi-threading way, computes a larger variety of observables and includes the possibility of using an alternative eigenbasis for the relevant statistical operator $\hat{\rho}_{\text{rel}}$ as described in Chapter 4. Also with this second implementation, the natural orbitals with occupation numbers, associated currents and spin are calculated. Additionally, the density–density covariance, single-particle-reduced entropy, von Neumann entropy, correlation entropy, energy or spin can be obtained. For more information about **NWFET-Lab**, its structure, features and technical details, see Appendix A.

3.6. Limit of the 1D approximation

Even if their aspect ratio (length-to-width ratio) is very high, semiconductor nanowires are 3D crystals, with more than one type of atom in its unit cell in general. Their cross-sectional geometry can be cylindrical, hexagonal, square or triangular. And their constituent material can be a direct or indirect band gap semiconductor. Nevertheless, the MCSCG method models the nanowire channel as a 1D nanostructure and considers only direct band gap semiconductors. Also, instead of considering realistically the crystal lattice of the semiconductor, it makes use of a 1D single-band tight-binding description, represented by a spatially localized 1D single-particle basis. Despite this drastic simplification, the model yields results consistent with experimental observations. We provide in this Section an analysis of the limit of this 1D approximation.

The single-particle Hamiltonian $\hat{H}_0 = \hat{H}_{\text{crystal}}(x) - eV_{\text{dop}}(x) - eV_{\text{ext}}(x)$ term can be divided into one "crystal" contribution $H_{\text{crystal}}(x)$, a potential arising from possible doping of the nanowire $V_{\text{dop}}(x)$ and an external potential due to gate and contacts $V_{\text{ext}}(x)$. The crystal Hamiltonian contains the dynamics of a single electron under the influence of a potential $V_{\text{crystal}}(x)$ periodic with the same period of the lattice and arising from the fixed localized ions. This term reads as

$$\hat{H}_{\text{crystal}}(x) = -\frac{\hbar^2}{2m^*}\frac{d^2}{dx^2} + V_{\text{crystal}}(x) \quad . \tag{3.23}$$

Written in terms of creation and annihilation operators, the single-particle Hamil-

tonian has the form

$$\hat{H}_0 = \sum_{jk} h_{jk} \hat{c}_j^\dagger \hat{c}_k \tag{3.24a}$$

$$h_{jk} = -e \int dx\ \phi_j^*(x)(V_{\text{dop}}(x) + V_{\text{ext}}(x))\phi_k(x) + \int dx\ \phi_j^*(x) H_{\text{crystal}}(x)\phi_k(x). \tag{3.24b}$$

The MCSCG limits the 1D tight-binding model to nearest-neighbors and so [83]

$$\int dx\ \phi_j^*(x) H_{\text{crystal}}(x)\phi_k(x) = \delta_{jk} d - \delta_{jk-1} t - \delta_{jk+1} t \tag{3.25}$$

where $t = \frac{\hbar^2}{2m^* a_0^2}$ are the nearest neighbors hopping terms for a single energy band and $d = 2t$ is the diagonal term. Here, a_0 is the lattice constant of the nanowire semiconductor. The corresponding energy band is of cosine nature and has the expression [83]

$$E(k) = d - 2t\cos(ka_0) = \frac{\hbar^2}{m^* a_0^2}(1 - \cos(ka_0)) \tag{3.26}$$

which can be approximated by a parabola at the vicinity of the minimum $k = 0$

$$E(k) = \frac{\hbar^2 k^2}{2m^*} \tag{3.27}$$

with an effective mass m^*, determined from the curvature of the band at $k = 0$. Figure 3.2 shows both energy bands. For energies $E(k) > t$ the effective mass approximation begins to fail.

On the other hand, it can be shown [84] that a nanowire of radius $R = d_{\text{ch}}/2$ with the following radial potential

$$V(r) = \begin{cases} 0 & \text{if } 0 < r < R \\ \infty & \text{if } r \geq R \end{cases} \tag{3.28}$$

is characterized by radial energies

$$E_r^{mn} = \frac{\hbar^2}{2m^*}\left(\frac{x_{mn}}{R}\right)^2 \tag{3.29}$$

with $m = 0, \pm 1, \pm 2, \ldots$ and $n = 1, 2, 3, \ldots$ being the angular and radial quantum

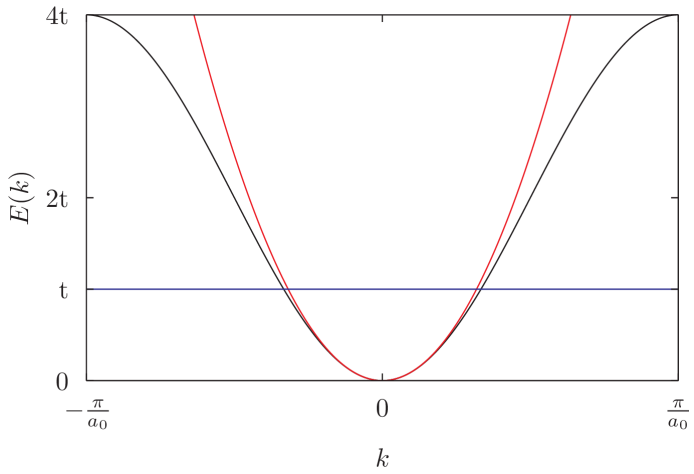

Figure 3.2.: Cosine and parabolic energy bands.

numbers respectively and x_{mn} the nth root of the mth Bessel function of the first kind J_m. We see that the radial energies depend on the nanowire diameter d_{ch} and the electron effective mass m^*.

As long as the typical energy of the electrons within the channel does not surpass the difference between the first and the second radial energies $\Delta E_r = E_r^{02} - E_r^{01}$, only the first radial mode is populated and the electronic transport can be considered as 1D. Electrons may have energies below $t = \frac{\hbar^2}{2m^* a_0^2}$ before the effective mass approximation begins to fail, so we compare ΔE_r with the whole range of energies $E_{\text{typ}}(z) = zt$ for $0.1 \leq z \leq 1$, to find an expression for the maximum nanowire channel diameter d_{ch}^* which limits the 1D approximation, as a function of the parameter z. By equating these two energies we arrive at

$$d_{\text{ch}}^* = 2a_0 \sqrt{\frac{x_{02}^2 - x_{01}^2}{z}} \quad . \tag{3.30}$$

For a nanowire with diameter above the estimated limit, the first and following excited radial modes begin to be populated and electronic transport begins to deviate from being purely 1D. Note that ΔE_r and t must also be larger than any relevant scale in transport direction (for example, the maximum $|eV_{\text{DS}}|$ or the barrier height).

Figure 3.3 shows d_{ch}^* as a function of the typical energy $E_{\text{typ}}(z) = zt$ for two different nanowire materials: InP and ZnO. At the highest energy ($z = 1$), if the

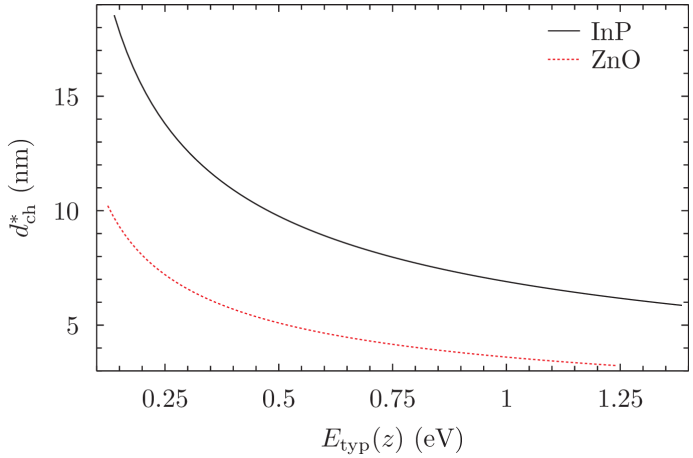

Figure 3.3.: Maximum diameter for the 1D approximation to be valid as a function of the electron energy $E_{\mathrm{typ}}(z) = zt$ for $0.1 \leq z \leq 1$, for two different nanowire semiconductors.

chosen material is InP ($a_0 = 5.9$ Å, $m^*/m_e = 0.079$) [78] or ZnO ($a_0 = 3.25$ Å, $m^*/m_e = 0.29$) [85], limit diameters $d^*_{\mathrm{ch}} = 5.86$ nm and $d^*_{\mathrm{ch}} = 3.23$ nm result, respectively.

3.7. Results: Coulomb blockade regime

In this section, we show some results obtained by means of the MCSCG method, for a NWFET in the Coulomb blockade regime. At low enough temperature and drain–source voltage V_{DS} (compared to the channel's Coulomb charging energy and single-particle energy level spacing), the energy which is necessary to add an extra electron to the channel can exceed the thermal energy, and the current through the NWFET is blocked. Within this Coulomb blockade regime, the NWFET behaves as a single-electron transistor (SET) [86, 87, 88, 89].

We have chosen the following parameters for the system. The channel consists of an InP nanowire, which has a lattice constant $a_0 = 5.9$ Å, an electron effective mass $m^*/m_e = 0.079$ and a relative dielectric constant $\varepsilon_{\mathrm{ch}} = 12.5$, as found in Ref. [78]. We considered a basis with a number of sites $N_{\mathrm{sites}} = 30$ giving a length $L = 17.7$ nm. Its diameter is $d_{\mathrm{ch}} = 5$ nm. The channel and the gate are separated by a SiO_2 oxide layer of thickness $d_{\mathrm{ox}} = 10$ nm and relative dielectric constant $\varepsilon_{\mathrm{ox}} = 3.9$. The device has a temperature of $T = 77$ K.

The source and drain are contacted with a metal to form Schottky barriers of height $\Phi_{SB} = 0.2$ eV with respect to the electrochemical potential of the contacts (μ_S and μ_D), which act as double tunnel barriers to confine the electrons in the nanowire. Figure 3.4 shows four potential profiles $V_{ext}(x)$ (see Eq. (3.4)) along the channel for different applied V_{GS} and V_{DS} for the considered system. No doping is present ($V_{dop}(x) = 0$) and the gate influence spans the whole nanowire ($V_G(0 \leq x \leq L) = V_G$). The Schottky barrier height Φ_{SB} is highlighted in the graphs with a two-way arrow and the electrochemical potential in the metal contacts is located 0.5 eV above their (artificial) band minima $E^M_{B_S}(\text{min})$ and $E^M_{B_D}(\text{min})$.

In the simulations, Coulomb diamonds emerge in the current–voltage characteristics, as shown in the black areas of Fig. 3.5. In these regions, the drain current I_D reduces to almost zero by Coulomb blockade and the channel is occupied by an integer number of electrons N_e. Along the $V_{DS} \simeq 0$ axis, drain current can flow where the electron number within the channel fluctuates between N_e and $N_e + 1$, that is, in the regions between the vertices of consecutive diamonds. By varying the gate–source voltage V_{GS} along this axis, Coulomb oscillations in the drain current or in the conductance such as those in Fig. 3.7 can be observed. The simulations correctly resemble the features that are observed in experiments [90, 91, 92, 93], which shows that the MCSCG method is able to capture few-electron charging effects in those situations where they play an important role.

A comparison between the current–voltage characteristics and the electron number, as shown in Figs. 3.5 and 3.6, reveals that I_D is not a smoothly changing function of the voltages, but presents plateaus with the shape of diamonds, whose low-left to up-right diagonals are aligned and approximately coincide with the contour lines where N_e takes an integer number (depicted in Fig. 3.6 by numbered black lines). These boundaries define diagonal "strips" where the current increases in steps for a fixed non-integer N_e between integer values. In comparison, a pure mean-field approach to the Coulomb interaction produces no plateaus, but smooth variations in the current with the voltage [46]. Figure 3.6 reveals that for fixed V_{DS}, the effect of increasing V_{GS} is to increase the electron number in the nanowire channel. As V_{GS} gets larger, a lower V_{DS} is required to maintain the same I_D in the device. This is clearly shown in Fig. 3.5, where the regions with equal drain current tend to approach the $V_{DS} = 0$ axis as V_{GS} is increased. This

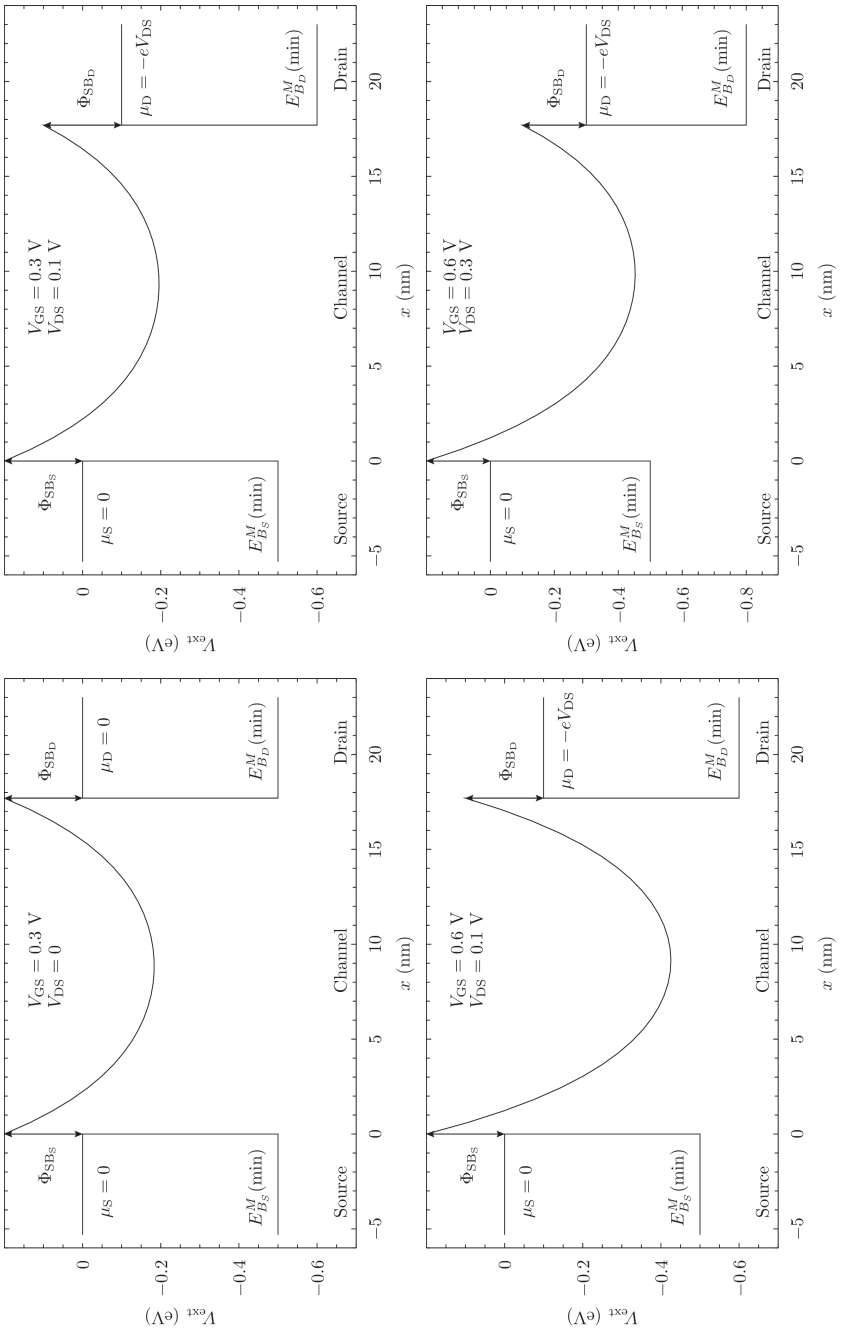

Figure 3.4.: Potential profile along the nanowire channel for different applied voltages.

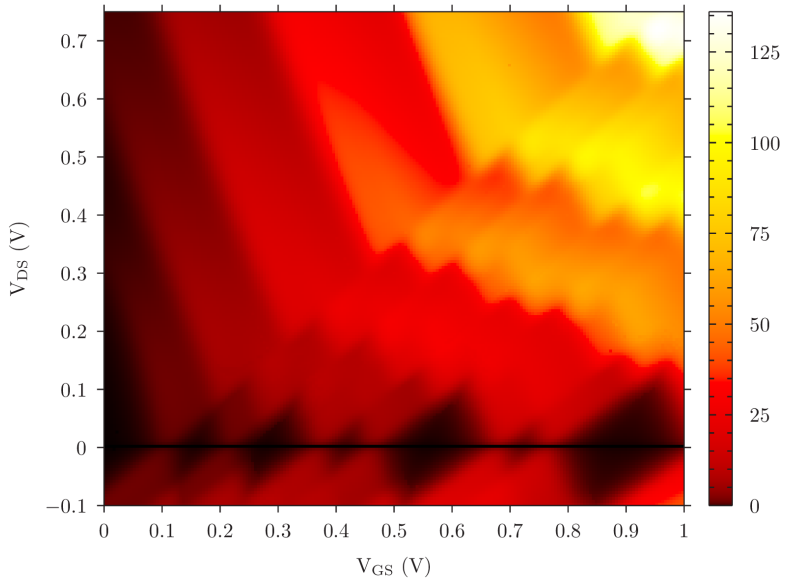

Figure 3.5.: Absolute value of the drain current $|I_D|$ (nA).

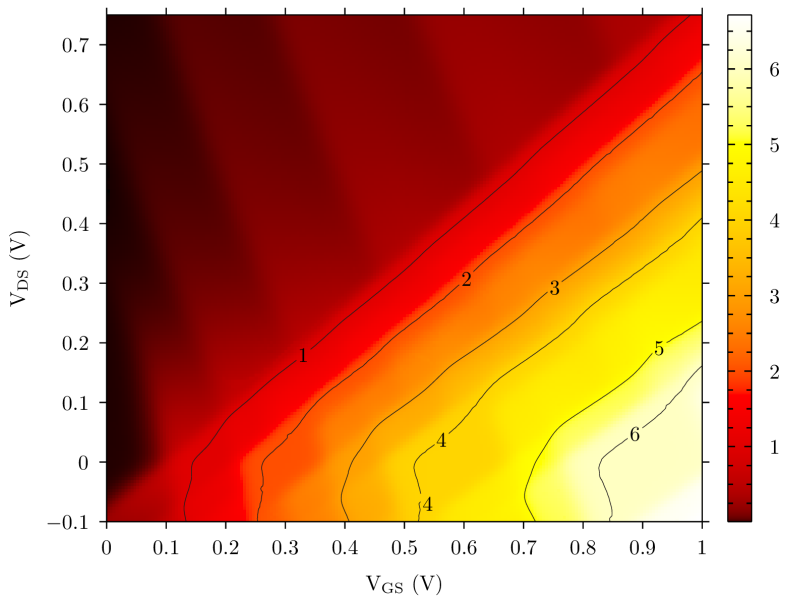

Figure 3.6.: Electron number N_e.

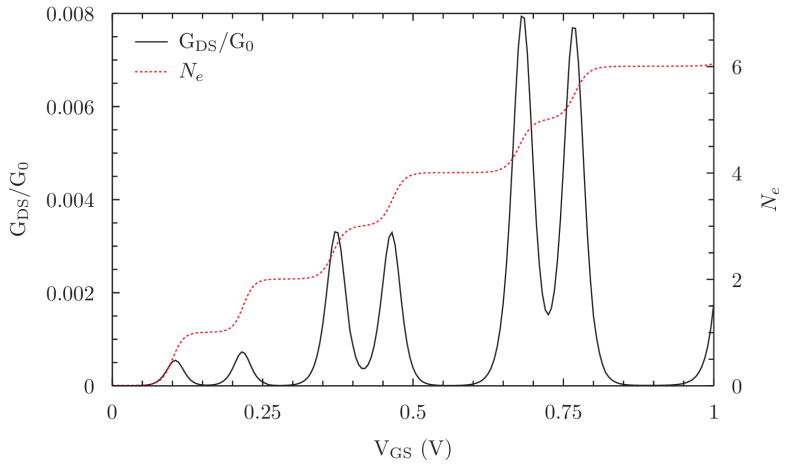

Figure 3.7.: Conductance oscillations G_{DS}/G_0 for $V_{DS} = 5$ mV, where $G_0 = 2e^2/h$ is the conductance quantum, and electron number N_e. Note that current flows for non-integer N_e, corresponding to the regions between Coulomb diamonds.

is to be expected, since for fixed V_{DS} the drain current increases with the number of electric carriers N_e involved in the transport, a quantity that gets larger with higher V_{GS}. Indeed, the effect of the gate is to vary the number of electrons that pass through the channel and therefore to change I_D.

Figure 3.8 shows the local density of states (LDOS) for an empty channel ($N_e = 0$), corresponding to the case $V_{DS} = 0$ and $V_{GS} = 0$. Sharp energy resonances can be seen, which correspond to resonantly trapped states.

Additionally, we have selected two non-equilibrium voltage points to analyze their natural orbital decomposition. Table 3.2 contains the relevant information describing these two situations, which we term as point X and point Y. Both

	Point X	Point Y
V_{GS} (V)	0.48	0.79
V_{DS} (V)	0.38	0.31
I_D (nA)	42.09	57.85
N_e	0.33	3.13
N_{occ}	0	2
N_{rel}	8	6

Table 3.2.: Characteristics of two selected voltage points.

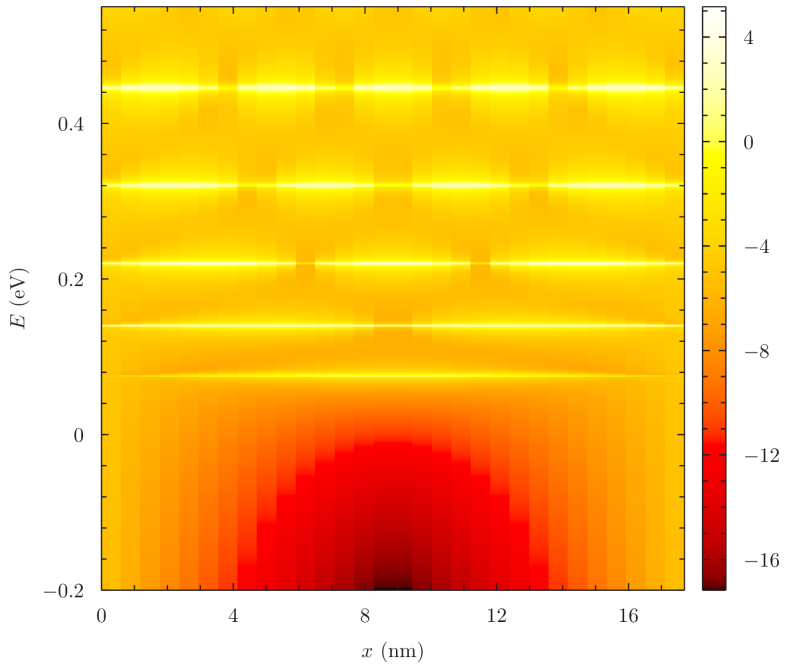

Figure 3.8.: LDOS (1/eV) in logarithmic scale for an empty channel.

points are characterized by having an appreciable drain current, whereas their electron numbers are quite different. As was shown in Sec. 3.3.4, the natural orbitals correspond to the columns of the unitary transformation matrix Υ that diagonalizes the density matrix ρ_1. We present plots of the highest occupied natural orbitals, together with their occupation numbers ξ_i and associated drain currents I_D, for point X in Fig. 3.9 and for point Y in Fig. 3.10. In these figures, the modulus squared of the even-numbered natural orbital wave functions corresponding to spin up (dashed red lines), spin down (dotted blue lines) and the total sum of these (solid black lines) are displayed. The odd-numbered natural orbitals are identical to the even-numbered, except for the fact that the wave functions for both spins are swapped, leaving the total unchanged, so they are not displayed.

Point X features 8 relevant natural orbitals which correspond to the four first panels in Fig. 3.9 with highest occupation number. The two lower panels correspond to the 4 following non-relevant natural orbitals, which describe electrons strongly coupled to the contacts, as is clear by the probability density distribution

being only appreciable in the extremes of the channel. These states are associated with a negative current but since their occupation number is very low, they do not affect the total current in a sensible way. Figure 3.11 shows the electron density for point X.

Point Y features 2 fully occupied natural orbitals ($\xi_0 \sim \xi_1 \sim 1$) which do not contribute to the current, contrarily to the next 6 relevant natural orbitals, as can be seen in Fig. 3.10. The probability densities are very similar to those of point X, only they are indexed in a different order. The natural orbitals with the highest contribution to the current are the same in both cases (0 and 1 for point X, 4 and 5 for point Y). Figure 3.12 shows the electron density for point Y.

We extend the analysis of the occupation number and current of each natural orbital to the whole V_{GS}–V_{DS} voltage plane. The natural orbitals are ordered by decreasing occupation number, not by identifying their wave functions, which may swap between voltage points. We can see by comparing Fig. 3.13a with Fig. 3.6 that the first two natural orbitals (0 and 1) have nonzero occupation number in the voltage regions where the electron number is $N_e < 1$ and present a significant increase in occupation number in the diagonal strip with $1 < N_e < 2$. They become fully occupied roughly for those voltages where the electron number $N_e > 2$. This is reasonable, since each natural orbital can be occupied by an electron or a fraction of an electron and the first two natural orbitals are the first to be populated. This can be better understood by analyzing the occupation number of the natural orbitals in the Coulomb diamonds. The "zeroth" diamond corresponds to $N_e = 0$ and we see that here the natural orbitals 0 and 1 are completely empty. The electronic state is characterized by the state $|00\rangle$. The first diamond corresponds to $N_e = 1$ and the electronic state is given by a mixture of the equally probable two configurations $|10\rangle$ and $|01\rangle$. The natural orbitals 0 and 1 are relevant and their occupation number takes a value around 0.5 in this diamond. From the second diamond on, they are fully occupied.

The same observation applies to Fig. 3.14a, where the occupation number of the two following natural orbitals (2 and 3) gradually increases with increasing electron number. In the voltage regions with $3 < N_e < 4$ the change is larger and for $N_e > 4$ they become fully occupied. The electronic state in the third Coulomb diamond is a mixture of $|1110\rangle$ and $|1101\rangle$. The occupation number of these natural orbitals takes a value of 0.5 in this diamond, in analogy with the

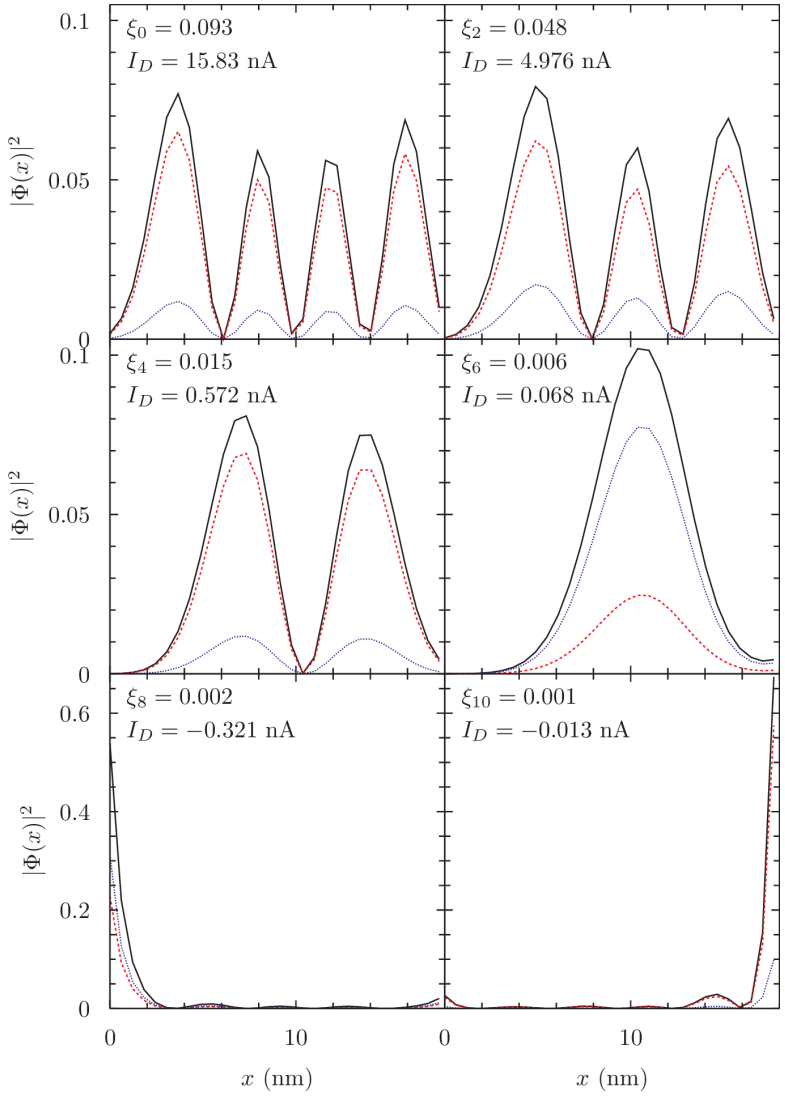

Figure 3.9.: Plots of the highest occupied natural orbitals with their occupation numbers ξ and associated drain currents I_D (nA) for point X. Spin up: dashed red lines. Spin down: dotted blue lines. Total: solid black lines.

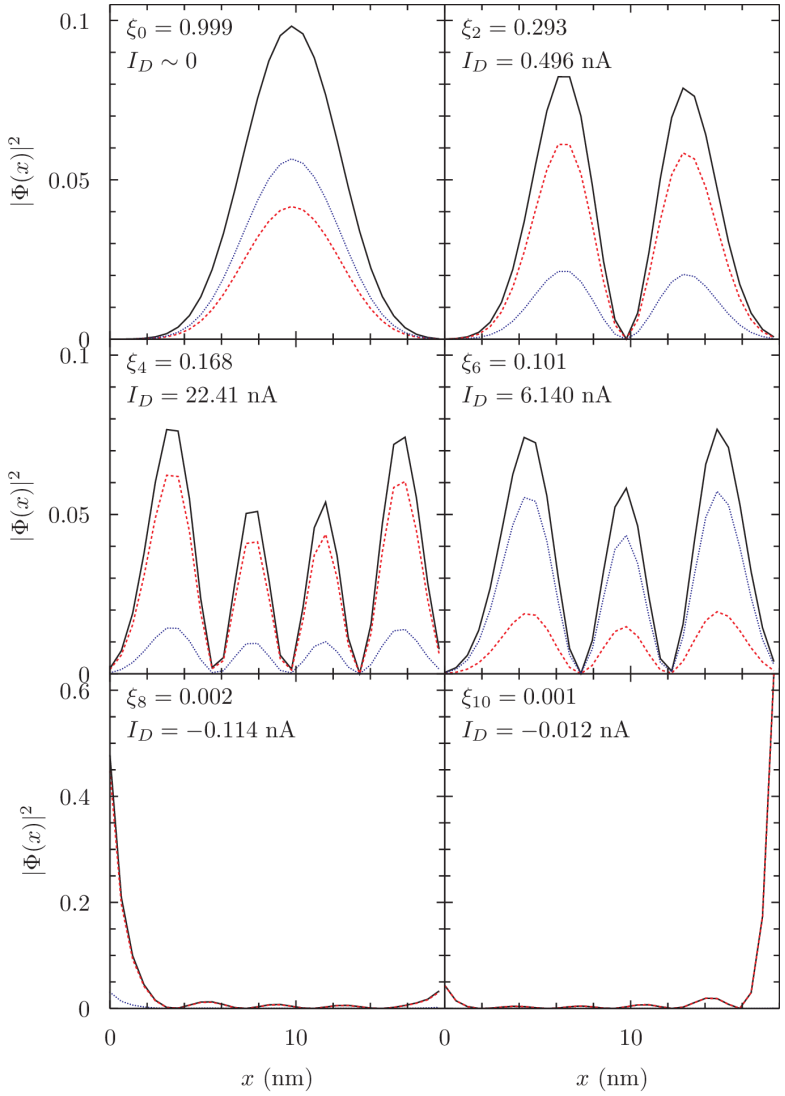

Figure 3.10.: Plots of the highest occupied natural orbitals with their occupation numbers ξ and associated drain currents I_D (nA) for point Y. Spin up: dashed red lines. Spin down: dotted blue lines. Total: solid black lines.

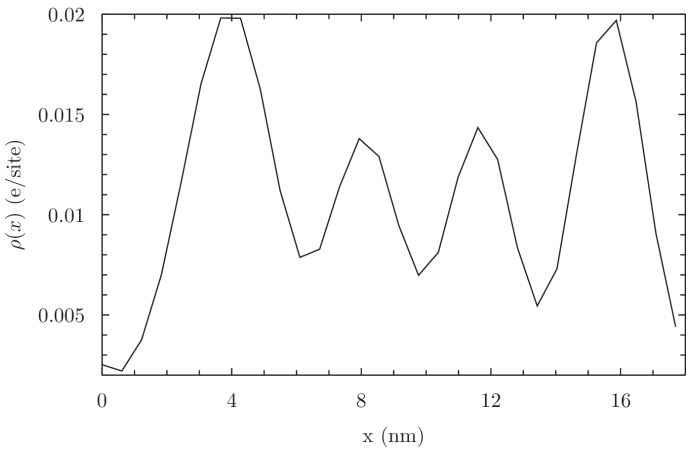

Figure 3.11.: Electron density for point X.

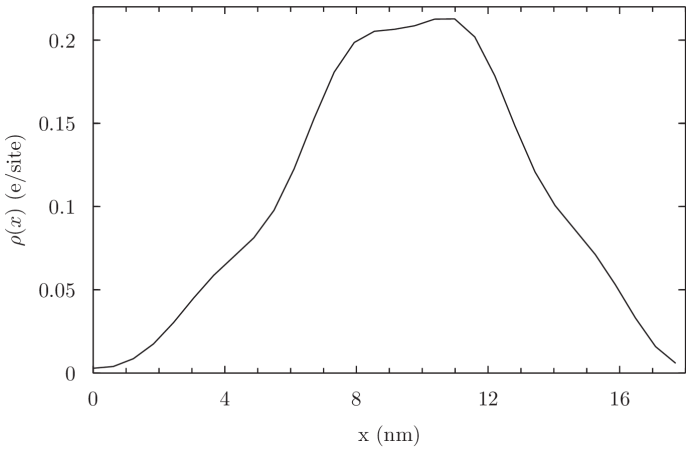

Figure 3.12.: Electron density for point Y.

first two natural orbitals and the first diamond. From the fourth diamond on, they are fully occupied. An analogous analysis applies to the natural orbitals 4 and 5 as shown in Fig. 3.15a.

Figure 3.13b shows the contribution of the first two natural orbitals (0 and 1) to the drain current, to be compared to their occupation number as shown in Fig. 3.13a. It is clear that the current takes nonzero values only in those voltage regions with $N_e < 1$, while it drops to zero outside these areas, where $N_e > 1$ and these natural orbitals begin to be largely populated. Fully occupied natural orbitals do not contribute to the total current. The same observations can be made of Figs. 3.14 and 3.15.

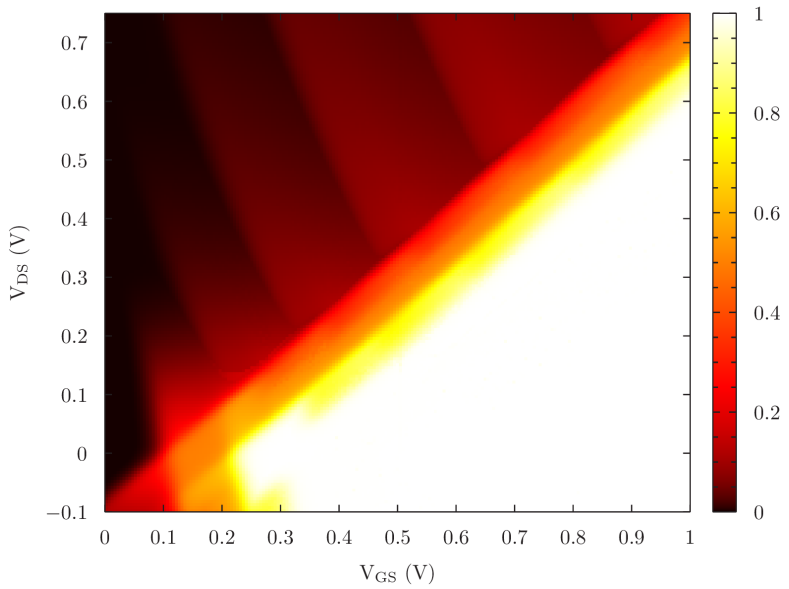

(a) Occupation number for natural orbitals 0 and 1

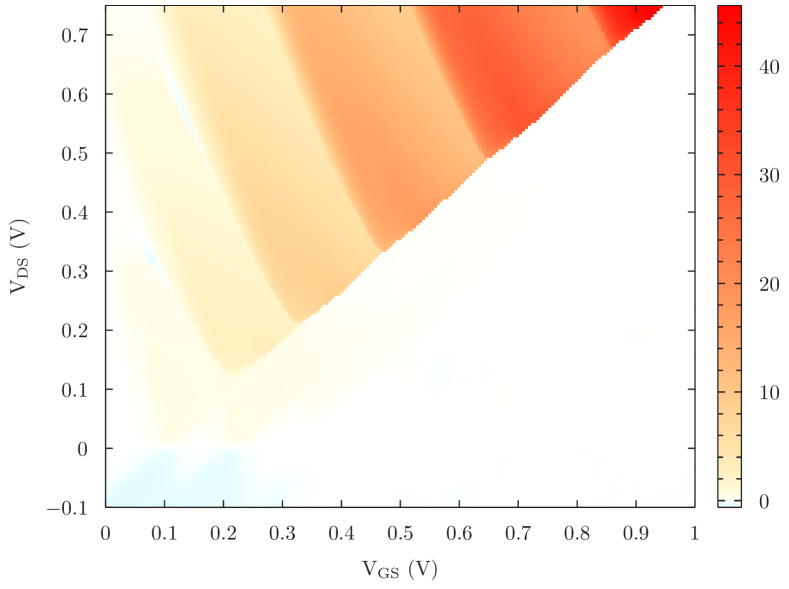

(b) Drain current I_D (nA) for natural orbitals 0 and 1

Figure 3.13.: Occupation number and drain current of natural orbitals 0 and 1 on the V_{GS}–V_{DS} plane.

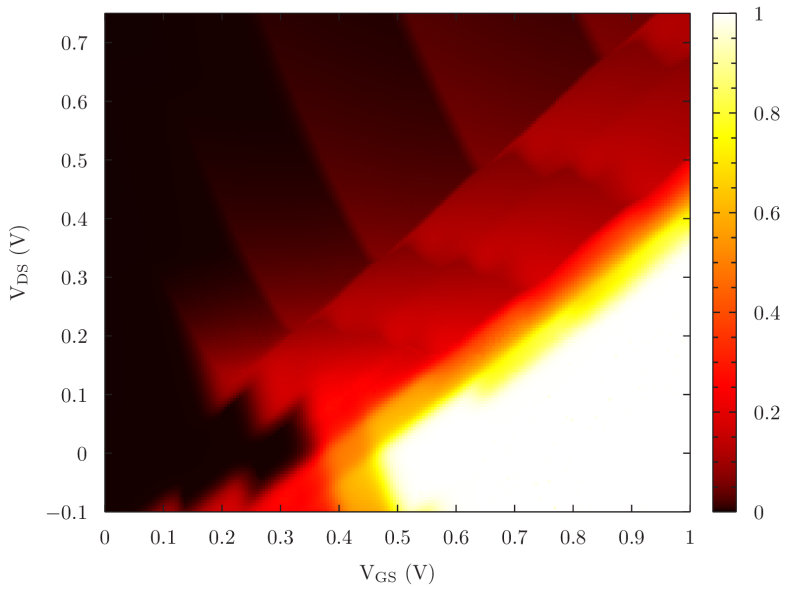

(a) Occupation number for natural orbitals 2 and 3

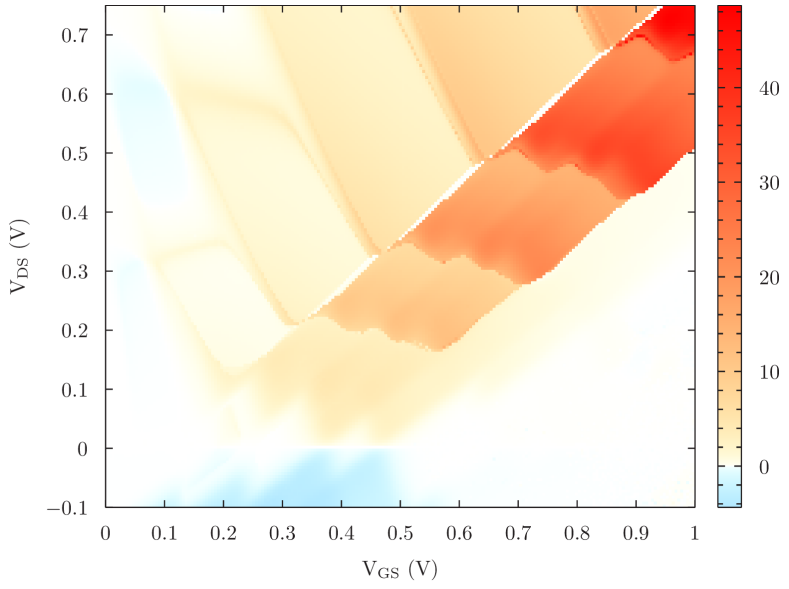

(b) Drain current I_D (nA) for natural orbitals 2 and 3

Figure 3.14.: Occupation number and drain current of natural orbitals 2 and 3 on the V_{GS}–V_{DS} plane.

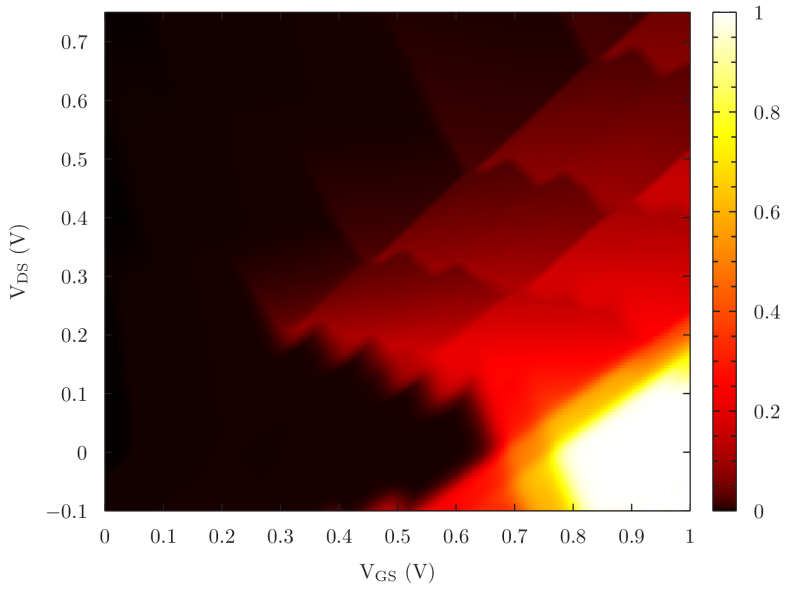

(a) Occupation number for natural orbitals 4 and 5

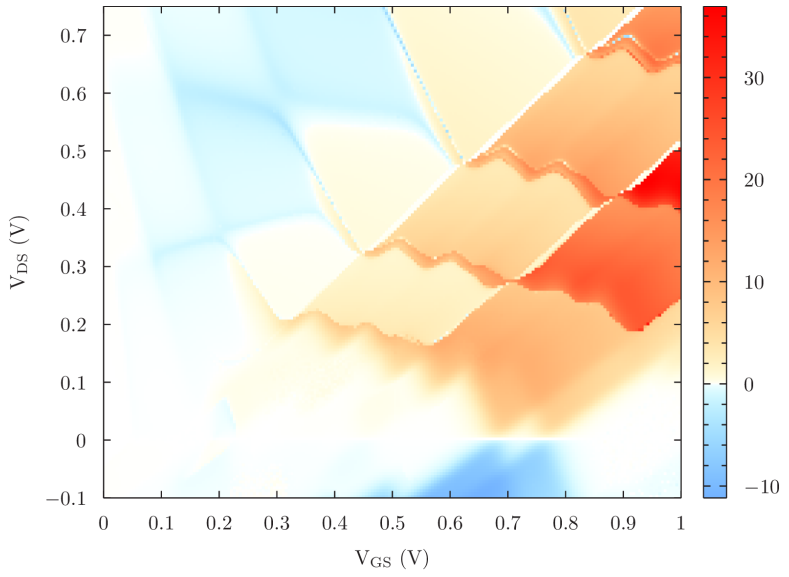

(b) Drain current I_D (nA) for natural orbitals 4 and 5

Figure 3.15.: Occupation number and drain current of natural orbitals 4 and 5 on the V_{GS}–V_{DS} plane.

4. Numerical determination of the non-equilibrium many-body statistical operator

4.1. Introduction

Various authors [94, 95, 96, 97] have considered the general mathematical construction of a non-equilibrium many-body statistical operator of interacting electrons for given external constraints or bias conditions. In this Chapter, we present an adaptive numerical approach to determine a reduced non-equilibrium many-body statistical operator $\hat{\rho}_{\mathrm{rel}}$ for quasi-isolated electronic states within the channel of a realistic NWFET system [98, 99, 100].

The underlying physical model assumes the knowledge of the (self-consistent) single-particle density matrix [79] ρ_1 of the whole channel system for the given gate and bias voltage condition, resulting from a non-equilibrium Green's function (NEGF) calculation for the NWFET for a given set of applied voltages (see Sec. 3.3.4). In turn, the single-particle Hilbert space of the whole channel system is divided into a small, adaptively chosen relevant subspace and an orthogonal rest, following the idea of the MCSCG approach, from which a relevant Fock subspace is constructed (see Sec. 3.4.1). From the given matrix ρ_1, a reduced many-body statistical operator $\hat{\rho}_{\mathrm{rel}}$ within the relevant subspace can be constructed. Here, the given matrix elements of ρ_1 impose constraints on $\hat{\rho}_{\mathrm{rel}}$. In comparison, the approach described in Ref. [95] is based on direct constraints on single-particle observables (such as the electronic current), whereas the approach described in this Chapter is based on a general ρ_1 with an adaptive relevant Fock subspace.

In general, the Fock subspace operator $\hat{\rho}_{\mathrm{rel}}$ is not uniquely defined by the constraint of a given single-particle density matrix ρ_1. Further physical assumptions

are therefore required. We assume that the eigenvalues w_N of $\hat{\rho}_{\text{rel}}$ are of a generalized grand-canonical Boltzmann form (to maximize entropy), parametrized by a set of effective electrochemical potentials and an effective temperature. Furthermore, for the assumed many-body eigenbasis of $\hat{\rho}_{\text{rel}}$, two alternatives are considered: (A) Slater determinants of relevant natural orbitals and (B) the eigenbasis of the projected many-body Hamiltonian within the relevant subspace. In order to determine an optimum $\hat{\rho}_{\text{rel}}$ that satisfies the given constraints on ρ_1 numerically, a genetic algorithm is employed that searches for the optimum solution that minimizes a suitably defined deviation measure.

From the determined $\hat{\rho}_{\text{rel}}$, one can calculate expectation values for any observable of the system. As an example, we describe the onset of formation of Wigner molecules by means of the electron density (a single-particle observable obtainable simply by means of ρ_1) and the density-density covariance (a many-body observable which can only be obtained by means of $\hat{\rho}_{\text{rel}}$).

The original implementation of the MCSCG algorithm (see Chapter 3) makes use of a $\hat{\rho}_{\text{rel}}$ expressed as a mixture of relevant Slater determinants of natural orbitals, as in case A above (see Sec. 3.4.2). **NWFET-Lab**, a new augmented version of the original implementation, has the possibility to choose between cases A and B, so it is able to alternatively employ a $\hat{\rho}_{\text{rel}}$ expressed as a mixture of eigenstates of the projected many-body Hamiltonian within the relevant subspace. For more details on **NWFET-Lab** see Appendix A.

4.2. Preliminary theoretical considerations

4.2.1. Relevant Fock space revisited

Following the lines of thought of Sec. 3.4.1, to make calculations of realistic nanowire devices numerically feasible, instead of considering the full Fock space, we restrict ourselves to a relevant subspace $\mathcal{F}_{\text{rel}}$. We still maintain the classification of single-particle states into relevant and non-relevant and construct a many-body basis $\mathcal{B}_{\text{rel}}$ of $\mathcal{F}_{\text{rel}}$ with Slater determinants $|D_K\rangle$ accordingly, so that to each $|D_K\rangle \in \mathcal{B}_{\text{rel}}$ corresponds a different combination of the bits (0 or 1) of the N_{rel} relevant natural orbitals. So again we have $\dim(\mathcal{F}_{\text{rel}}) = 2^{N_{\text{rel}}}$.

Nevertheless, we introduce a difference here. The natural orbitals whose average occupation numbers are close to unity ($\xi_i \simeq 1$) can be treated in two

$$\mathcal{F}_{\text{rel}} = \{ \quad |11000000\rangle, \quad |11100000\rangle, \quad |11010000\rangle, \quad |11110000\rangle, \\ |11001000\rangle, \quad |11101000\rangle, \quad |11011000\rangle, \quad |11111000\rangle \quad \}$$

Table 4.1.: An example of many-body relevant basis $\mathcal{B}_{\text{rel}}$.

alternative ways: (i) they may be treated as being fully occupied (bit set to 1 for N_{occ} bits) in every $|D_K\rangle$ and thus being incorporated statically within the many-body Fock subspace, or (ii) they may be set as empty (bit set to 0) in every $|D_K\rangle$ and being incorporated in a mean-field way (in the single-particle part of the Hamiltonian), which is the approach followed in Sec. 3.4.1. The rest of the natural orbitals (i.e., those which are empty with $\xi_i \simeq 0$ or which are fluctuating but being strongly coupled to the contacts) are kept empty (bit set to 0 for N_{rest} bits) in every $|D_K\rangle$ and being incorporated in a mean-field way (in the single-particle part of the Hamiltonian).

Thus, when fixing the occupied states in all Slater determinants, $|D_K\rangle$ is composed of N_{occ} to $N_{\text{occ}} + N_{\text{rel}}$ electrons, whereas if using a mean-field description for these single-particle states $|D_K\rangle$ is composed of 0 to N_{rel} electrons. This can be found in a modified version of **coul.c** [101].

As an example, we show the relevant many-body basis $\mathcal{B}_{\text{rel}}$ of the relevant Fock subspace $\mathcal{F}_{\text{rel}}$ in Table 4.1 with $N_{\text{max}} = 8$, $N_{\text{occ}} = 2$ and $N_{\text{rel}} = 3$, implying that its dimension is $\dim(\mathcal{F}_{\text{rel}}) = 2^3 = 8$.

In the special situation where $N_{\text{rel}} = 0$, all single-particle states are either empty or occupied and the state of the system is described by a single Slater determinant. On the other hand, whenever $N_{\text{rel}} > 0$ this is no longer the case. The many-body state cannot then be described by just a single Slater determinant and therefore we construct $\mathcal{B}_{\text{rel}}$ which serves as a basis in order to express it.

4.2.2. Mean-field interaction revisited

As presented in the previous Sec. 4.2.1, we have the choice to treat the fully occupied single-particle states in a many-body way, by fixing their corresponding bits to one in every $|D_K\rangle$, or set them to zero and treat them in a mean-field way. We consider optionally also the possibility of treating the non-relevant rest of single-particle states with a mean-field approach or not at all.

As in Sec. 3.4.3, the Coulomb self-energy given by Eq. (3.16) is used for

the mean-field description of Coulomb interaction, with a single-particle density matrix $\hat{\rho}_{1\mathrm{vac}}$ for the vacuum state within the relevant Fock subspace $\mathcal{F}_{\mathrm{rel}}$. $\hat{\rho}_{1\mathrm{vac}}$ can be obtained from its diagonal form $\rho^{\mathrm{diag}}_{1\mathrm{vac}_{ij}} = \delta_{ij}\xi^{\mathrm{vac}}_i$ by $\rho_{1\mathrm{vac}} = \Upsilon\rho^{\mathrm{diag}}_{1\mathrm{vac}}\Upsilon^\dagger$, where Υ is the unitary transformation that diagonalizes the single-particle density matrix ρ_1. We have now two options for the terms ξ^{vac}_i corresponding to non-relevant single-particle states, either to consider mean-field interaction and set them to their actual values $\xi^{\mathrm{vac}}_i = \xi_i$ or not to consider mean-field interaction and set their values to zero $\xi^{\mathrm{vac}}_i = 0$. As before, all relevant single-particle states have an average occupation number $\xi^{\mathrm{vac}}_i = 0$ (vacuum state within $\mathcal{F}_{\mathrm{rel}}$).

4.2.3. Change to natural orbital basis

Since $\mathcal{F}_{\mathrm{rel}}$ is constructed in terms of Slater determinants of a subset of natural orbitals, the best would be to get the matrix elements and Coulomb tensor elements in the natural orbital basis, whose transformation is given by Υ, the unitary matrix that diagonalizes $\hat{\rho}_1$. Also, this is done because in case we want to truncate the calculations using this basis, the impact on the results would be smaller than in the case of the localized orbital basis (it would be equivalent to cut the nanowire).

The creation and annihilation operators $\hat{c}^\dagger_i$ and $\hat{c}_i$ (with hat) in the spin/site basis are related to those in the natural orbital basis $c^\dagger_i$ and c_i (without hat) as follows [42]

$$\hat{c}^\dagger_i = \sum_{k=0}^{N_{\mathrm{max}}-1} \Upsilon^*_{ik} c^\dagger_k \quad , \quad \hat{c}_i = \sum_{k=0}^{N_{\mathrm{max}}-1} \Upsilon_{ik} c_k \quad . \tag{4.1}$$

From these expressions we can verify that the single-particle matrix given by Eq. (3.5b) and the two-particle tensor given by Eq. (3.6b) of the Hamiltonian transform as follows

$$h'_{ij} + \Sigma^{r'}_{ee_{ij}}[\rho_{1\mathrm{vac}}] = \sum_{p,q=0}^{N_{\mathrm{max}}-1} \Upsilon^*_{ip}\Upsilon_{jq}(h_{pq} + \Sigma^{r}_{ee_{pq}}[\rho_{1\mathrm{vac}}]) \tag{4.2a}$$

$$V'_{ijkl} = \sum_{p,q,r,s=0}^{N_{\mathrm{max}}-1} \Upsilon^*_{ip}\Upsilon^*_{jq}\Upsilon_{kr}\Upsilon_{ls}V_{pqrs} \quad . \tag{4.2b}$$

See implementation in **coul.c** [101].

4.2.4. Projected many-body Hamiltonian

The projected many-body Hamiltonian $\hat{H}_{\text{rel}}$ within the relevant Fock subspace $\mathcal{F}_{\text{rel}}$ is obtained from $\hat{H}$ (see Sec. 3.3.3) via projection to the relevant Fock subspace $\mathcal{F}_{\text{rel}}$. It has dimensions $\dim(\mathcal{F}_{\text{rel}})\times\dim(\mathcal{F}_{\text{rel}})$. For every pair of Slater determinants of natural orbitals $|D_I\rangle, |D_J\rangle \in \mathcal{B}_{\text{rel}}$ we obtain the matrix element $\langle D_I|\,\hat{H}_{\text{rel}}\,|D_J\rangle$ as follows

$$\langle D_I|\,(\hat{H}_0 + \hat{H}_{ee}^{\text{ext}})\,|D_J\rangle = \sum_{i,j=0}^{N_{\text{max}}-1} (h'_{ij} + \Sigma^{r'}_{ee_{ij}}[\hat{\rho}_{1\text{vac}}])\,\langle D_I|\,c_i^\dagger c_j\,|D_J\rangle \tag{4.3a}$$

$$\langle D_I|\,\hat{H}_{ee}\,|D_J\rangle = \sum_{i,j,k,l=0}^{N_{\text{max}}-1} V'_{ijkl}\,\langle D_I|\,c_i^\dagger c_j^\dagger c_k c_l\,|D_J\rangle \tag{4.3b}$$

where the elements of the matrix h'_{ij}, the Coulomb self-energy $\Sigma^{r'}_{ee_{ij}}[\hat{\rho}_{1\text{vac}}]$ and the Coulomb tensor V'_{ijkl} in the natural orbital basis are already known.

Two kinds of operator products need to be evaluated: single-particle terms $\langle D_I|\,c_i^\dagger c_j\,|D_J\rangle$ and two-particle terms $\langle D_I|\,c_i^\dagger c_j^\dagger c_k c_l\,|D_J\rangle$. These terms are evaluated according to the Fermionic anti-commutation rules [42] obeyed by the creation and annihilation operators for the natural orbital basis states $c_i^\dagger$ and c_i, as given by Eqs. (2.2). The action of these operators is as described in Eqs. (2.1). See implementation in functions *twoop* and *fourop* from **coul.c** [101].

4.2.5. Diagonalization of the projected many-body Hamiltonian

Once the matrix representation of $\hat{H}_{\text{rel}}$ has been obtained it can be diagonalized, yielding $\dim(\mathcal{F}_{\text{rel}})$ eigenstates $|\psi_N\rangle$ and eigenenergies E_N that satisfy the eigenvalue equation

$$\hat{H}_{\text{rel}}\,|\psi_N\rangle = E_N\,|\psi_N\rangle \quad . \tag{4.4}$$

Every energy eigenstate expressed in the basis $\{|D_K\rangle\}$ of $\mathcal{F}_{\text{rel}}$ has the form

$$|\psi_N\rangle = \sum_{K=0}^{\dim(\mathcal{F}_{\text{rel}})-1} \Lambda_{KN}\,|D_K\rangle \tag{4.5}$$

where $\Lambda_{KN} = \langle D_K\,|\,\psi_N\rangle$, which defines a unitary transformation matrix Λ that diagonalizes the projected many-body Hamiltonian matrix: $\Lambda^\dagger H_{\text{rel}}\Lambda = H_{\text{rel}}^{\text{diag}}$.

In order to check the validity of the method so far, we can compare the many-body eigenenergies $E_N(1)$ corresponding to a particle number $N_e = 1$ with the single-particle eigenenergies resulting from diagonalizing the $N_{\rm rel} \times N_{\rm rel}$ sub-matrix of the single-particle Hamiltonian H_0 expressed in the natural orbital basis. They should coincide. We can also compare the energy differences $E_{M_1}(N+1) - E_{M_2}(N)$, corresponding to $N_e = N+1$ and $N_e = N$ respectively, with the resonances in the LDOS obtained with the MCSCG method [82].

Another way of verifying the results is to treat in mean-field the non-relevant fixed occupied and empty single-particle states but setting their respective $\xi_i^{\rm vac}$ to 1 and 0, not to their actual values. Forcing this situation is equivalent to consider no mean-field and setting these states fixed in the Slater determinants. The eigenvector components of $\hat{H}_{\rm rel}$ given by Λ should coincide in both situations and the energies should just be shifted by a constant amount.

4.3. Many-body statistical operator

4.3.1. On the statistical preparation of the system

The statistical preparation of the relevant subsystem is given by the reduced many-body statistical operator

$$\hat{\rho}_{\rm rel} = \sum_{N=0}^{\dim(\mathcal{F}_{\rm rel})-1} w_N \, |\rho_N\rangle \, \langle \rho_N| \quad . \tag{4.6}$$

It is Hermitian and satisfies $\mathrm{Tr}(\hat{\rho}_{\rm rel}) = \sum_N w_N = 1$, with $w_N \in [0,1]$. The eigenvalue w_N can be interpreted as the probability associated with the eigenstate $|\rho_N\rangle$. The eigenvectors of $\hat{\rho}_{\rm rel}$ can be expressed in terms of the basis of Slater determinants of natural orbitals via the unitary transformation X as follows

$$|\rho_J\rangle = \sum_{K=0}^{\dim(\mathcal{F}_{\rm rel})-1} X_{KJ} \, |D_K\rangle \tag{4.7}$$

whose components read as $X_{KJ} = \langle D_K \, | \, \rho_J \rangle$.

There is no beforehand prescription on how to determine $\hat{\rho}_{\rm rel}$. It should describe in the best of the possible ways our state of knowledge about the physical situation, without drawing any conclusions not warranted by the available data.

In this sense the probability distribution given by $\hat{\rho}_{\text{rel}}$ which is most conservative is the one that is as smooth and spread out as possible, subject to the available information of the system, since then no special cases or states are over or under estimated without motivation. This measure of amount of uncertainty is given by the entropy. In order to determine $\hat{\rho}_{\text{rel}}$, we require that its probability distribution maximizes the entropy subject to certain constraints. This determines the functional form of the eigenvalues w_N of $\hat{\rho}_{\text{rel}}$, known as grand canonical or Boltzmann form. Entropy maximization is covered in Sec. 4.4.

So far, no assumption has been made about the eigenvectors $|\rho_N\rangle$ that form the orthonormal eigenbasis of $\hat{\rho}_{\text{rel}}$ within the relevant Fock subspace $\mathcal{F}_{\text{rel}}$. In the following, we consider two cases: (A) the Slater determinant basis of natural orbitals and (B) the eigenbasis of $\hat{H}_{\text{rel}}$ within the relevant subspace. One has to note that for a stationary relevant subsystem, where the time evolution of $\hat{\rho}_{\text{rel}}$ is assumed to be driven solely by the projected $\hat{H}_{\text{rel}}$, both operators need to commute, leading to the basis choice (case B) where $|\rho_N\rangle$ are chosen as eigenstates of $\hat{H}_{\text{rel}}$.

4.3.2. Single-particle density matrix constraint

The constraint that $\hat{\rho}_{\text{rel}}$ must satisfy is given by the following expression

$$\rho_{1_{ij}} \overset{!}{=} \text{Tr}(\hat{\rho}_{\text{rel}} c_j^\dagger c_i) \quad (\forall i,j \in \text{relevant}) \tag{4.8}$$

which links $\hat{\rho}_{\text{rel}}$ with the given ρ_1 within the N_{rel} dimensional subspace of relevant natural orbitals. It results from the fact that the expectation value of any single-particle observable $\hat{A} = \sum_{i,j=0}^{N_{\text{max}}-1} a_{ij} c_i^\dagger c_j$ can be obtained in the following two equivalent ways

$$\left\langle \hat{A} \right\rangle = \text{Tr}(\hat{\rho}_{\text{rel}} \hat{A}) = \sum_{i,j=0}^{N_{\text{max}}-1} a_{ij} \text{Tr}(\hat{\rho}_{\text{rel}} c_i^\dagger c_j) \tag{4.9}$$

$$\left\langle \hat{A} \right\rangle = \text{Tr}(\rho_1 a) = \sum_{i,j=0}^{N_{\text{max}}-1} a_{ij} \rho_{1ji} \quad . \tag{4.10}$$

Within the relevant single-particle subspace (N_{rel} dimensional), equation (4.8) provides a set of $N_{\text{rel}} \times N_{\text{rel}}$ complex conditions. Noting that both sides of the

equation are Hermitian, we can see that the number of unique real constraints is reduced to $N_{\text{rel}} \times N_{\text{rel}}$.

Since we are using the natural orbital basis in which the given ρ_1 is diagonal with eigenvalues ξ_i and according to the expression of $\hat{\rho}_{\text{rel}}$ determined by Eq. (4.6), the constraints imposed by Eq. (4.8) can be rewritten as

$$\xi_i \delta_{ij} \stackrel{!}{=} \sum_n w_n \langle \rho_n | \, c_j^\dagger c_i \, | \rho_n \rangle \quad (\forall i, j \in \text{ relevant}). \tag{4.11}$$

Here, the indices i and j are restricted to the relevant subspace in the natural orbital basis.

One has to note that the diagonal constraints ($i = j$) are equivalent to constrained average particle numbers $\langle \hat{n}_i \rangle$ for the corresponding natural orbitals. For the following subsections, we denote the resulting coefficients as

$$N_i(|\rho_N\rangle) \equiv \langle \rho_N | \, c_i^\dagger c_i \, | \rho_N \rangle = \langle \rho_N | \, \hat{n}_i \, | \rho_N \rangle \tag{4.12}$$

so that this subset of ρ_1-diagonal constraints read as

$$\xi_i \stackrel{!}{=} \sum_N w_N N_i(|\rho_N\rangle) \quad (\forall i \in \text{ relevant}). \tag{4.13}$$

It can be shown that Eqs. (4.8) are restricted to the subset of relevant single-particle states, so the number of relevant constraints is $N_{\text{rel}} \times N_{\text{rel}}$ instead of $N_{\text{max}} \times N_{\text{max}}$. This follows from the analysis of the quantity $\langle D_{K'} | \, c_j^\dagger c_i \, | D_K \rangle$, which appears in Eqs. (4.11) once we express $|\rho_N\rangle$ in terms of the basis of Slater determinants of natural orbitals via the unitary transformation X (see Eq. (4.7)). If any of the indices i or j correspond to any of the N_{rest} unoccupied single-particle states of $|D_K\rangle$ or $|D_{K'}\rangle$ then $\langle D_{K'} | \, c_j^\dagger c_i \, | D_K \rangle = 0, \ \forall \ K, K'$. Therefore $\langle \rho_N | \, c_j^\dagger c_i \, | \rho_N \rangle = 0, \ \forall \ N$ and Eqs. (4.11) reduce to $\xi_i \delta_{ij} = 0$. These are not a set of constraints for $\mathbf{w}$. If $i = j$ they imply $\xi_i = 0$, which is what we assumed for the non-relevant almost empty natural orbitals. If $i \neq j$ they are trivial equalities $0 = 0$. Similarly, if any of the indices i or j correspond to any of the N_{occ} occupied single-particle states of $|D_K\rangle$ or $|D_{K'}\rangle$ then $\langle D_{K'} | \, c_j^\dagger c_i \, | D_K \rangle = \delta_{ij} \delta_{KK'}$. Therefore $\langle \rho_N | \, c_j^\dagger c_i \, | \rho_N \rangle = \delta_{ij} \sum_K X_{KN}^* X_{KN} = \delta_{ij}, \ \forall \ N$ and Eqs. (4.11) reduce to $\xi_i \delta_{ij} = \delta_{ij} \sum_N w_N = \delta_{ij}$. These are not a set of constraints for $\mathbf{w}$. If $i = j$ they imply $\xi_i = 1$, which is what we assumed for the non-relevant almost occupied

natural orbitals. If $i \neq j$ they are trivial equalities $0 = 0$.

4.3.3. Average energy constraint

Assuming the average energy $\langle E \rangle$ of the system, or equivalently the temperature T, is a well-defined constant quantity, there exists a relation between the statistical operator $\hat{\rho}_{\text{rel}}$ and $\langle E \rangle$, namely

$$\langle E \rangle = \text{Tr}(\hat{\rho}_{\text{rel}} \hat{H}_{\text{rel}}) = \sum_N w_N \langle \rho_N | \hat{H}_{\text{rel}} | \rho_N \rangle = \sum_N w_N \varepsilon_N \tag{4.14}$$

where we have defined

$$\varepsilon_N \equiv \langle \rho_N | \hat{H}_{\text{rel}} | \rho_N \rangle \quad . \tag{4.15}$$

This constraint is taken into account by fixing the temperature, which appears in the grand canonical form of w_N.

4.3.4. Case A: Slater determinant basis of natural orbitals

In this case, the statistical operator corresponds to a mixture of Slater determinants of relevant natural orbitals, that is $\{|\rho_N\rangle\} = \{|D_N\rangle\}$. This is the same situation as described in Sec. 3.4.2. Thus, we obtain

$$\hat{\rho}_{\text{rel}} = \sum_{N=0}^{\dim(\mathcal{F}_{\text{rel}})-1} w_N |D_N\rangle \langle D_N| \quad . \tag{4.16}$$

In this case $X = I$ and its matrix representation is diagonal in the Slater determinant basis of natural orbitals $\{|D_N\rangle\}$. The off-diagonal constraints given by Eqs. (4.11) vanish. The remaining equations for the diagonal terms, Eqs. (4.13), read as

$$\xi_i \stackrel{!}{=} \sum_{N=0}^{\dim(\mathcal{F}_{\text{rel}})-1} w_N N_i(|D_N\rangle) \quad (\forall i \in \text{ relevant}), \tag{4.17}$$

where we defined $N_i(|D_N\rangle) \equiv \langle D_n | \hat{n}_i | D_n \rangle$ as the occupation number of the relevant natural orbital i for the Slater determinant $|D_n\rangle$. The energies in Eq. (4.15) associated with each eigenvector $|D_n\rangle$ of $\hat{\rho}_{\text{rel}}$ are given by the diagonal elements of H_{rel} and read as $\varepsilon_N = \langle D_N | \hat{H}_{\text{rel}} | D_N \rangle = H_{\text{rel}_{NN}}$. Both quantities, $N_i(|D_N\rangle)$ and ε_N are required in Eqs. (4.28) and (4.29) below.

One has to note that the vector $\mathbf{w}$ of eigenvalues of $\hat{\rho}_{\mathrm{rel}}$ with $\dim(\mathcal{F}_{\mathrm{rel}}) = 2^{N_{\mathrm{rel}}}$ components has to satisfy a set of N_{rel} conditions given by Eqs. (4.17), so the number of unknowns is greater than the number of constraints and the problem is under-determined in general, thus requiring further assumptions about the function form of w_N, such as a Boltzmann form (see Sec. 4.4).

4.3.5. Case B: eigenbasis of the projected many-body Hamiltonian

In this case, we assume a stationary state of a relevant subsystem that is solely driven by the projected $\hat{H}_{\mathrm{rel}}$. Thus, we have $[\hat{\rho}_{\mathrm{rel}}, \hat{H}_{\mathrm{rel}}] = 0$ and, consequently, we choose $\{|\rho_N\rangle\}$ to be identical to the orthonormal eigenbasis $\{|\psi_N\rangle\}$ of the projected $\hat{H}_{\mathrm{rel}}$. Hence, we obtain

$$\hat{\rho}_{\mathrm{rel}} = \sum_{N=0}^{\dim(\mathcal{F}_{\mathrm{rel}})-1} w_N \left|\psi_N\right\rangle \left\langle\psi_N\right| \tag{4.18}$$

which in the Slater determinant basis of natural orbitals $\{|D_N\rangle\}$ reads as

$$\rho_{\mathrm{rel}_{KK'}} = \left\langle D_K\right| \hat{\rho}_{\mathrm{rel}} \left|D_{K'}\right\rangle = \sum_{N=0}^{\dim(\mathcal{F}_{\mathrm{rel}})-1} w_N \Lambda^*_{K'N} \Lambda_{KN} \tag{4.19}$$

since in this case $X = \Lambda$. The ρ_1 constraints have the form

$$\begin{aligned} \xi_i \delta_{ij} &\stackrel{!}{=} \sum_{N=0}^{\dim(\mathcal{F}_{\mathrm{rel}})-1} w_N \left\langle\psi_N\right| c_j^\dagger c_i \left|\psi_N\right\rangle \\ &= \sum_{N=0}^{\dim(\mathcal{F}_{\mathrm{rel}})-1} w_N \sum_{K,K'=0}^{\dim(\mathcal{F}_{\mathrm{rel}})-1} \Lambda^*_{K'N} \Lambda_{KN} \left\langle D_{K'}\right| c_j^\dagger c_i \left|D_K\right\rangle \end{aligned} \tag{4.20}$$

$\forall\ i, j \in$ relevant. For the diagonal coefficients of Eq. (4.12) we have

$$N_i(|\psi_N\rangle) = \left\langle\psi_N\right| \hat{n}_i \left|\psi_N\right\rangle = \sum_{K=0}^{\dim(\mathcal{F}_{\mathrm{rel}})-1} |\Lambda_{KN}|^2 N_i(|D_K\rangle) \quad . \tag{4.21}$$

The energies E_N associated with each eigenvector $|\psi_N\rangle$ of $\hat{\rho}_{\mathrm{rel}}$ are given by the eigenvalues of H_{rel}, that is, $\varepsilon_N = E_N$ here. Both $N_i(|\psi_N\rangle)$ and ε_N are required in Eqs. (4.28) and (4.29) below.

The vector $\mathbf{w}$ of eigenvalues of $\hat{\rho}_{\text{rel}}$ with $\dim(\mathcal{F}_{\text{rel}}) = 2^{N_{\text{rel}}}$ components has to satisfy a set of $N_{\text{rel}} \times N_{\text{rel}}$ conditions given by Eqs. (4.20). If $N_{\text{rel}} = 3$, the number of constraints is larger than the number of unknowns and the problem is over-determined. If $N_{\text{rel}} = 2$ or 4, the number of constraints coincides with the number of unknowns. For $N_{\text{rel}} > 4$ the relation $2^{N_{\text{rel}}} > N_{\text{rel}}^2$ holds, the problem is under-determined, thus requiring further assumptions about the function form of w_n, such as a Boltzmann form (see Sec. 4.4).

A way to check the consistency of the method is to artificially set H_{rel} to a diagonal form by forcing $\Lambda_{IJ} = \delta_{IJ}$, which makes case B identical with case A and so should yield the same results.

4.4. Maximum entropy

4.4.1. Entropy maximization with Lagrange multipliers

The chosen ansatz of a grand canonical form for the eigenvalues w_N of $\hat{\rho}_{\text{rel}}$ results from the assumption of maximum entropy under a number of constraints. This means they must be such that the von Neumann entropy (within the relevant subspace)

$$S = -k_B \text{Tr}(\hat{\rho}_{\text{rel}} \ln \hat{\rho}_{\text{rel}}) = -k_B \sum_{N=0}^{\dim(\mathcal{F}_{\text{rel}})-1} w_N \ln w_N \tag{4.22}$$

is maximized. k_B is Boltzmann's constant and S has units J/K. Alternatively we can express S in bit units. A bit is defined as $k_B \ln 2$ and $S/(k_B \ln 2) = -\sum_N w_N \log_2 w_N$ is the expression of the entropy in bits.

The entropy maximization subject to several constraints can be performed by the use of Lagrange multipliers. The constraints are given by the normalization condition, the average energy given by Eq. (4.14) and the average particle number (in natural orbitals) given by Eqs. (4.13). The respective Lagrange multipliers are α, β and the set of N_{rel} multipliers γ_i. We require that the Lagrangian function

$$\begin{aligned} L = S - (\alpha - k_B) \left(\sum_{N=0}^{\dim(\mathcal{F}_{\text{rel}})-1} w_N - 1 \right) - \beta \left(\sum_{N=0}^{\dim(\mathcal{F}_{\text{rel}})-1} \varepsilon_N w_N - \langle E \rangle \right) - \\ - \sum_{i=0}^{N_{\text{rel}}-1} \gamma_i \left(\sum_{N=0}^{\dim(\mathcal{F}_{\text{rel}})-1} N_i(|\rho_N\rangle) w_N - \xi_i \right) \end{aligned} \tag{4.23}$$

is maximized, which in essence is equal to maximizing the entropy S, since the Lagrange multipliers multiply null expressions if the constraints are satisfied.

By requiring $\frac{\partial L}{\partial w_N} = 0$ we arrive at the following relation that gives the weights once all the Lagrange multipliers are known

$$w_N = \exp\left(-\frac{1}{k_B}\left(\alpha + \beta\varepsilon_N + \sum_{i=0}^{N_{\text{rel}}-1}\gamma_i N_i(|\rho_N\rangle)\right)\right) \quad . \tag{4.24}$$

From this form for the weights and the normalization constraint we get an expression which determines the Lagrange multiplier α once β and γ are known

$$\alpha = k_B \ln(Z(\beta, \gamma)) \tag{4.25}$$

where we have defined the so called partition function

$$Z(\beta, \gamma) = \sum_{N=0}^{\dim(\mathcal{F}_{\text{rel}})-1} \exp\left(-\frac{1}{k_B}\left(\beta\varepsilon_N + \sum_{i=0}^{N_{\text{rel}}-1}\gamma_i N_i(|\rho_N\rangle)\right)\right) \quad . \tag{4.26}$$

The meaning of the Lagrange multipliers β and γ_i is as usual in thermodynamics [102], namely

$$\beta = \frac{1}{T} \quad , \quad \gamma_i = -\beta\mu_i = -\frac{\mu_i}{T} \tag{4.27}$$

where T is the temperature and μ_i is the electrochemical potential associated with the single particle state i. Note that if the electrochemical potentials are different, the system is in non-equilibrium.

With these results at hand, the form of the statistical weights as functions of the temperature T and the chemical potentials μ_i reads as

$$w_N = \frac{1}{Z(T, \mu)} \exp\left(-\frac{1}{k_B T}\left(\varepsilon_N - \sum_{i=0}^{N_{\text{rel}}-1}\mu_i N_i(|\rho_N\rangle)\right)\right) \tag{4.28}$$

with the following expression for the partition function

$$Z(T, \mu) = \sum_{N=0}^{\dim(\mathcal{F}_{\text{rel}})-1} \exp\left(-\frac{1}{k_B T}\left(\varepsilon_N - \sum_{i=0}^{N_{\text{rel}}-1}\mu_i N_i(|\rho_N\rangle)\right)\right) \quad . \tag{4.29}$$

4.4.2. Infinite temperature limit

We consider here the limit in which the electrons behave like independent particles, the maximum entropy infinite temperature limit. The consequence of making this limit is that the form of the weights is modified. Analyzing the quantities that appear in their exponents we have

$$\lim_{T\to\infty}\left(\frac{\varepsilon_n}{k_B T}\right) = 0 \quad , \quad \lim_{T\to\infty}\left(\frac{\mu_i}{k_B T}\right) = \mu_i' \tag{4.30}$$

resulting in an expression for the weights

$$w_N = \frac{1}{Z(\mu')}\exp\left(\sum_{i=1}^{N'_\mu}\mu_i' N_i(|D_N\rangle)\right) \tag{4.31}$$

with the partition function

$$Z(\mu') = \sum_n \exp\left(\sum_{i=1}^{N'_\mu}\mu_i' N_i(|D_N\rangle)\right) \quad . \tag{4.32}$$

Considering this, the present calculation of the newly defined Lagrange parameters μ' is analogous to the one in section 4.4. Only in this case the form of the weights is different, the quantities ε_n being absent.

Furthermore, in the limit of independent particles the weights have the following analytical form,

$$w_n = \prod_{i=1}^{N_{\max}} \xi_i^{N_i(|D_N\rangle)}\,(1-\xi_i)^{1-N_i(|D_N\rangle)} \tag{4.33}$$

where $\xi_i \in [0,1]$ is the average occupation number of fluctuating single-particle state i (eigenvalue i of ρ_1) and $N_i(|D_N\rangle) \in \{0,1\}$ is the particle number in Slater determinant $|D_N\rangle$ in state i. Its implementation can be found in [81]. We expect these solutions to reflect some of the characteristics of the Slater determinants.

It is possible to prove [103] that Eq. (4.33) implies the form of the weights given by Eq. (4.31). For this task we first write the weights as

$$w_N = \prod_{i=1}^{N_{\max}} u_i(N_i(|D_N\rangle)) \quad , \quad u_i(m_i) \equiv K_i \exp(\mu_i' m_i) \tag{4.34}$$

where the expression for u_i is motivated by Eq. (4.31). Then we can show that K_i and μ_i' exist which are independent of m_i and only dependent on ξ_i. Let us study the two possible cases

$$m_i = 0 \quad \Rightarrow \quad u_i(m_i) = K_i \equiv 1 - \xi_i \tag{4.35a}$$

$$m_i = 1 \quad \Rightarrow \quad u_i(m_i) = K_i \exp(\mu_i') \equiv \xi_i \tag{4.35b}$$

from where we get a form for K_i and μ_i'

$$K_i = 1 - \xi_i \quad , \quad \mu_i' = \ln\left(\frac{\xi_i}{1-\xi_i}\right) \quad . \tag{4.36}$$

As one can see K_i and μ_i' exist and are independent of m_i and only depend on ξ_i. To obtain an expression for Z we compare both forms for w_n given by Eq. (4.31) and Eq. (4.34)

$$w_N = \frac{1}{Z}\prod_{i=1}^{N_{\max}} \frac{u_i(N_i(|D_N\rangle))}{K_i} = \prod_{i=1}^{N_{\max}} u_i(N_i(|D_N\rangle)) \quad \Rightarrow \quad Z = \frac{1}{\prod_{i=1}^{N_{\max}}(1-\xi_i)}. \tag{4.37}$$

These results prove the validity of the analytical expression Eq. (4.33) for the weights in the case of independent particles. One can check this by substituting the formulas for Z and μ_i' in Eq. (4.31) to arrive at Eq. (4.33).

As an alternative to the derivation of the form for μ_i' we consider the case of independent particles (Fermions) with the Fermi-Dirac occupation probability

$$\xi_i = f(E_i) = \frac{1}{\exp\left(\frac{E_i-\mu_i}{k_B T}\right)+1} \quad . \tag{4.38}$$

In the limit $k_B T \to \infty$ Eqs. (4.30) hold. We have then

$$\xi_i = \frac{1}{\exp(-\mu_i')+1} \quad \Rightarrow \quad \mu_i' = \ln\left(\frac{\xi_i}{1-\xi_i}\right) \tag{4.39}$$

and we arrive at the same form for μ_i'.

4.5. Numerical determination of the weights

In order to find a solution for the vector $\mathbf{w}$ of $2^{N_{\mathrm{rel}}}$ eigenvalues of $\hat{\rho}_{\mathrm{rel}}$, the N_{rel} electrochemical potentials μ_i must be adjusted in such a way that the resulting $\mathbf{w}$ satisfies the ρ_1 constraints. The partition function ensures normalization and the condition that T is given is equivalent to fix the average energy of the system. One has to note that under non-equilibrium conditions (due to an applied voltage V_{DS} between the source and drain contacts at the outer ends of the channel), the effective electrochemical potentials μ_i become independent quantities in general.

Since the problem is under-determined in general, it is possible that more than a single solution exists. On the other hand, there might exist no exact solution for the constraints at all for the assumed functional form of w_N and eigenbasis of $\hat{\rho}_{\mathrm{rel}}$. In the latter case, one has to search for an optimum set of μ_i that minimizes a measure of deviation from the constraint condition.

In Sec. 4.5.1 it is shown that in case A, the Newton-Raphson method is capable of obtaining solutions that fulfill condition (4.13) numerically. Nevertheless, the method cannot be applied to case B, where the number of constraints $N_{\mathrm{rel}} \times N_{\mathrm{rel}}$ is larger than the number N_{rel} of electrochemical potentials in general.

So for case B, as well as for case A if desired, a single-objective genetic algorithm [104] (GA) optimization method is used in the following. Its goal is to minimize an objective function given by the absolute value of the deviation from exact constraint satisfaction with the μ_i as optimization variables. There are several benefits in using a GA: It operates in parallel with a population of candidate solutions, instead of just a single one. It always yields a solution which improves after every iteration, in contrast to other methods that simply do not give a solution if convergence is not achieved. It can leave local optimum points in the search space behind, even if the objective function is not smooth. We have chosen to implement the GA using the multi-crossover formula described in Ref. [105]. For an overview about GAs, see Appendix B.

4.5.1. Newton-Raphson method

To obtain expressions for the chemical potentials we substitute the weights in the form given by Eq. (4.28) in each of the constraints. By virtue of the normalization

constraint, we can write the constraints given by Eqs. (4.13) as

$$\sum_{N=0}^{\dim(\mathcal{F}_{\rm rel})-1} (N_i(|\rho_N\rangle) - \xi_i) w_N = 0 \quad . \tag{4.40}$$

Then substituting w_N we arrive at the following $N_{\rm rel}$ relations

$$F_k(\mu) = \sum_{N=0}^{\dim(\mathcal{F}_{\rm rel})-1} (N_k(|\rho_N\rangle) - \xi_k) E(\mu) = 0 \tag{4.41}$$

where we define

$$E(\mu) \equiv \exp\left(-\frac{1}{k_B T}\left(\varepsilon_N - \sum_{i=0}^{N_{\rm rel}-1} \mu_i N_i(|\rho_N\rangle)\right)\right) \quad . \tag{4.42}$$

This set of equations relate the chemical potentials μ_i and depend only on the known quantities ξ_i, T, ε_N and $N_i(|\rho_N\rangle)$. The zeros or roots of Eqs. (4.41) are the chemical potentials we are looking for. We make use of the multidimensional Newton-Raphson method for this task. This method starts by assigning initial values to μ_i. At each iteration they are updated $\mu_i \to \mu_i + \delta\mu_i$ by addition of a correction $\delta\mu_i$ such that

$$\sum_{i=0}^{N_{\rm rel}-1} \frac{\partial F_k(\mu)}{\partial \mu_i} \delta\mu_i = -F_k(\mu) \quad , \quad k = 0, 1, \ldots, N_{\rm rel} - 1 \tag{4.43}$$

where from Eqs. (4.41) we have

$$\frac{\partial F_k(\mu)}{\partial \mu_i} = \frac{1}{k_B T} \sum_{N=0}^{\dim(\mathcal{F}_{\rm rel})-1} N_i(|\rho_N\rangle)(N_k(|\rho_N\rangle) - \xi_k) E(\mu) \quad . \tag{4.44}$$

These equations can be written in matrix form as

$$J\delta\mu = -F \quad \to \quad \delta\mu = -J^{-1}F \tag{4.45}$$

where J is a $N_{\text{rel}} \times N_{\text{rel}}$ square matrix known as Jacobian with the following structure

$$J = \begin{pmatrix} \frac{\partial F_0}{\partial \mu_0} & \cdots & \frac{\partial F_0}{\partial \mu_{N_{\text{rel}}-1}} \\ \vdots & & \vdots \\ \frac{\partial F_{N_{\text{rel}}-1}}{\partial \mu_0} & \cdots & \frac{\partial F_{N_{\text{rel}}-1}}{\partial \mu_{N_{\text{rel}}-1}} \end{pmatrix} \quad . \tag{4.46}$$

With the new vector $\mu+\delta\mu$ we update the relations F, obtain a new Jacobian and repeat the algorithm until convergence is achieved. Convergence criterion is given by the magnitude of the corrections $\delta\mu_i$ being smaller than a given threshold.

4.5.2. Optimization by genetic algorithm

As we have seen, the free optimization variables to be adjusted in order to obtain the eigenvalues $\mathbf{w}$ of $\hat{\rho}_{\text{rel}}$ are the chemical potentials μ_i. Assuming $V_{\text{DS}} > 0$ they are restricted to the interval $-e\,V_{\text{DS}} \leq \mu_i \leq 0$. If $V_{\text{DS}} < 0$ we have $0 \leq \mu_i \leq -e\,V_{\text{DS}}$. We employ a GA as optimization method (see Appendix B for details), where the chemical potentials are encoded in the genes of the chromosomes of the GA and there are as many genes in a chromosome as chemical potentials. The objective function η to be minimized is the averaged sum of the absolute value of the deviation from the exact constraints satisfaction. It has the following expression

$$\eta = \frac{1}{N_{\text{rel}} \times N_{\text{rel}}} \sum_{j \leq i=0}^{N_{\text{rel}}-1} \left| \sum_{N=0}^{2^{N_{\text{rel}}}-1} w_N \left\langle \rho_N \right| c_j^\dagger c_i \left| \rho_N \right\rangle - \delta_{ij}\xi_i \right| \quad . \tag{4.47}$$

4.6. Expectation values

Once the relevant statistical operator $\hat{\rho}_{\text{rel}}$ has been calculated, the expectation or average value of any observable $\hat{A}$ can be obtained, as follows

$$\left\langle \hat{A} \right\rangle = \text{Tr}\left(\hat{\rho}_{\text{rel}}\hat{A}\right) = \sum_{N=0}^{\dim(\mathcal{F}_{\text{rel}})-1} w_N \left\langle \rho_N \right| \hat{A} \left| \rho_N \right\rangle \quad . \tag{4.48}$$

A mixture of states as given by $\hat{\rho}_{\text{rel}}$ adds an additional statistical averaging. The expectation value, like the trace of a matrix, is independent of the representation. So the same results are expected to be obtained in any many-body orthonormal

basis. Nevertheless, $\langle \hat{A} \rangle$ is dependent on the actual expression of $\hat{\rho}_{\text{rel}}$ as given by its eigenbasis and weights. So beforehand we might expect differences in the calculated expectation values depending on the case under consideration, cases A and B.

We analyze these two cases for a general physical observable $\hat{A}$. The following equations describe how to obtain $\langle \hat{A} \rangle$

$$\langle \hat{A} \rangle = \sum_{N=0}^{\dim(\mathcal{F}_{\text{rel}})-1} w_N \langle D_N | \hat{A} | D_N \rangle \tag{4.49a}$$

$$\langle \hat{A} \rangle = \sum_{N=0}^{\dim(\mathcal{F}_{\text{rel}})-1} w_N \langle \psi_N | \hat{A} | \psi_N \rangle = \sum_{N=0}^{\dim(\mathcal{F}_{\text{rel}})-1} w_N \sum_{I,J=0}^{\dim(\mathcal{F}_{\text{rel}})-1} \Lambda^*_{IN} \Lambda_{JN} \langle D_I | \hat{A} | D_J \rangle \tag{4.49b}$$

in case A and B respectively. As these two expressions show, the work-flow to calculate the expectation value of an observable is as follows: compute the matrix elements of the observable in the Slater determinant basis of natural orbitals, then for case B transform to the eigenbasis of $\hat{H}_{\text{rel}}$ according to the unitary transformation Λ. Finally sum all weighted contributions. So we only need one many-body quantum mechanical calculation for each matrix element and the rest are just matrix multiplications. We obtain ultimately the matrix elements in the Slater determinant basis of natural orbitals since we assume $\hat{A}$ to be expressed in terms of creation and annihilation operators acting on natural orbitals. If this is not the case they have to be transformed to the natural orbital basis.

4.7. Electron density and covariance

4.7.1. Physical meaning

The electron number at spin/site i is given by the expectation value of the number operator $\langle \hat{n}_i \rangle = \left\langle \hat{c}_i^\dagger \hat{c}_i \right\rangle$ in the localized single-particle basis. It describes the number of electrons that are located in each site with spin up or down. Here and in the following we omit the spin index, which is assumed to be absorbed into a collective spin/site index. Each electron inside the NWFET channel occupies in general more than one site, its wave function is spread along the nanowire and so is the electron density. Note that the expectation value of the electron number

operator may be non-integer in general.

The density–density covariance is defined as

$$\sigma_{ij} \equiv \langle (\hat{n}_i - \langle \hat{n}_i \rangle)(\hat{n}_j - \langle \hat{n}_j \rangle) \rangle = \langle \hat{n}_i \hat{n}_j \rangle - \langle \hat{n}_i \rangle \langle \hat{n}_j \rangle \tag{4.50}$$

and describes the reciprocal linear relationship between the electron densities at two spin/sites i and j of the nanowire channel. Whenever the probability for both densities to have deviations from the mean value which are both positive or both negative (they "vary together") is relatively high, the covariance takes a positive value. On the other hand, the covariance is negative if the probability that one deviation is positive and the other negative (they "vary oppositely"), is relatively high. The covariance is constrained within the following limits

$$-\sigma_i \sigma_j \leq \sigma_{ij} \leq \sigma_i \sigma_j \tag{4.51}$$

where $\sigma_i \equiv \sqrt{\sigma_{ii}}$ is the square root of the variance or standard deviation. It can attain one of these limits only in the case that $\hat{n}_i$ and $\hat{n}_j$ satisfy a linear relationship.

It can be seen that the density–density covariance is symmetric ($\sigma_{ij} = \sigma_{ji}$) by noting that

$$\begin{aligned} \hat{n}_i \hat{n}_j = \hat{c}_i^\dagger \hat{c}_i \hat{c}_j^\dagger \hat{c}_j = \delta_{ij} \hat{c}_i^\dagger \hat{c}_j - \hat{c}_i^\dagger \hat{c}_j^\dagger \hat{c}_i \hat{c}_j = \delta_{ij} \hat{c}_i^\dagger \hat{c}_j - \hat{c}_j^\dagger \hat{c}_i^\dagger \hat{c}_j \hat{c}_i = \\ = \delta_{ij} \hat{c}_i^\dagger \hat{c}_j - \delta_{ij} \hat{c}_j^\dagger \hat{c}_i + \hat{c}_j^\dagger \hat{c}_j \hat{c}_i^\dagger \hat{c}_i = \hat{n}_j \hat{n}_i \end{aligned} \tag{4.52}$$

and we can verify that the diagonal elements, which can be identified with the variance, have the form

$$\sigma_{ii} = \langle \hat{n}_i \rangle - \langle \hat{n}_i \rangle^2 \tag{4.53}$$

by realizing that the number operator is idempotent

$$\hat{n}_i \hat{n}_i = \hat{c}_i^\dagger \hat{c}_i \hat{c}_i^\dagger \hat{c}_i = \hat{c}_i^\dagger \hat{c}_i - \hat{c}_i^\dagger \hat{c}_i^\dagger \hat{c}_i \hat{c}_i = \hat{n}_i \tag{4.54}$$

where we have used the fact that $\hat{c}_i^\dagger \hat{c}_i^\dagger = \hat{c}_i \hat{c}_i = 0$ by the Fermionic anti-commutation relations.

Linear independence of $\hat{n}_i$ and $\hat{n}_j$ implies $\sigma_{ij} = 0$. On the other hand, the density–density covariance may be zero even if there is an interdependence of a

nonlinear kind between these quantities. Moreover, the covariance depends on the units of measurement. For this reason, the correlation is defined as

$$\kappa_{ij} \equiv \left\langle \left(\frac{\hat{n}_i - \langle \hat{n}_i \rangle}{\sigma_i} \right) \left(\frac{\hat{n}_j - \langle \hat{n}_j \rangle}{\sigma_j} \right) \right\rangle = \frac{\sigma_{ij}}{\sigma_i \sigma_j} \quad . \tag{4.55}$$

This measure of interdependence does not change with a rescaling of the variables and its limits are

$$-1 \leq \kappa_{ij} \leq 1 \quad . \tag{4.56}$$

4.7.2. Case A: diagonal elements

In case A we need only the diagonal elements of the observables, as Eq. (4.49a) shows. It is possible to transform the general expressions of the diagonal elements into specific and simplified forms which link the quantities together.

The electron density is defined in the localized single-particle basis. Since the Slater determinants express many-body states of natural orbitals we have to transform $\hat{n}_i$ to the natural orbital basis by means of Eqs. (4.1). Doing so leads to the following expression

$$\begin{aligned} \langle D_N | \, \hat{n}_i \, | D_N \rangle = \langle D_N | \, \tilde{c}_i^\dagger \tilde{c}_i \, | D_N \rangle = \sum_{jk} \Upsilon_{ij}^* \Upsilon_{ik} \underbrace{\langle D_N | \, c_j^\dagger c_k \, | D_N \rangle}_{N_k(|D_N\rangle)\delta_{jk}} = \\ = \sum_k |\Upsilon_{ik}|^2 \, N_k(|D_N\rangle) \end{aligned} \tag{4.57}$$

and so the electron density reads

$$\langle \hat{n}_i \rangle = \sum_N w_N \sum_k |\Upsilon_{ik}|^2 \, N_k(|D_N\rangle) \quad . \tag{4.58}$$

More cumbersome is the calculation of the density–density covariance. According to Eq. (4.50), the expectation value of the product of number operators at two spin/sites $\langle \hat{n}_i \hat{n}_j \rangle$ has to be computed. Its normal-ordered form, with all creation operators at the left and annihilation operators at the right, can be obtained by anti-commutation as follows

$$\hat{n}_i \hat{n}_j = \hat{c}_i^\dagger \hat{c}_i \hat{c}_j^\dagger \hat{c}_j = \hat{c}_i^\dagger \hat{c}_j^\dagger \hat{c}_j \hat{c}_i + \delta_{ij} \hat{c}_i^\dagger \hat{c}_i \tag{4.59}$$

from which we deduce that

$$\langle D_N|\, \hat{n}_i \hat{n}_j \,|D_N\rangle = \delta_{ij} \langle D_N|\, \hat{n}_i \,|D_N\rangle + \langle D_N|\, \hat{c}_i^\dagger \hat{c}_j^\dagger \hat{c}_j \hat{c}_i \,|D_N\rangle \quad . \tag{4.60}$$

We focus on the non-diagonal term and transform it into the natural orbital basis to obtain

$$\langle D_N|\, \hat{c}_i^\dagger \hat{c}_j^\dagger \hat{c}_j \hat{c}_i \,|D_N\rangle = \sum_{p,q,r,s} \Upsilon_{ip}^* \Upsilon_{jq}^* \Upsilon_{jr} \Upsilon_{is} \langle D_N|\, c_p^\dagger c_q^\dagger c_r c_s \,|D_N\rangle \quad . \tag{4.61}$$

Since it is evaluated with respect to the same Slater determinant, the term between brackets is nonzero only if $p = s$ and $q = r$ or if $p = r$ and $q = s$, so the only strings of operators that have to be considered are $c_p^\dagger c_q^\dagger c_q c_p = -c_p^\dagger c_q^\dagger c_p c_q$ and $c_p^\dagger c_q^\dagger c_p c_q$.

4.7.3. Case B: full matrix

Case B according to Eq. (4.49b), makes use of all the matrix elements of $\hat{n}_i$ and $\hat{n}_i \hat{n}_j$ in the Slater determinant basis and not only the diagonal. Their form is more general and we give it here, noting that once obtained it is straightforward to translate from the Slater determinant basis to the basis of the projected many-body Hamiltonian $\hat{H}_{\text{rel}}$. Transforming the operators to the natural orbital basis, the electron density matrix elements in the Slater determinant basis of natural orbitals read as

$$\langle D_M|\, \hat{n}_i \,|D_N\rangle = \langle D_M|\, \hat{c}_i^\dagger \hat{c}_i \,|D_N\rangle = \sum_{j,k} \Upsilon_{ij}^* \Upsilon_{ik} \langle D_M|\, c_j^\dagger c_k \,|D_N\rangle \tag{4.62}$$

and we can verify that $\langle D_N|\, \hat{n}_i \,|D_M\rangle^* = \langle D_M|\, \hat{n}_i \,|D_N\rangle$. The remaining term to obtain the covariance reads as

$$\langle D_M|\, \hat{n}_i \hat{n}_j \,|D_N\rangle = \delta_{ij} \langle D_M|\, \hat{n}_i \,|D_N\rangle + \sum_{p,q,r,s} \Upsilon_{ip}^* \Upsilon_{jq}^* \Upsilon_{jr} \Upsilon_{is} \langle D_M|\, c_p^\dagger c_q^\dagger c_r c_s \,|D_N\rangle \,. \tag{4.63}$$

4.8. Results: onset of formation of Wigner molecules

As a result of the method to obtain the relevant many-body statistical operator of the NWFET, we calculate the density–density correlation κ_{ij} for successive steps in the transition between two different regimes of the electrons inside the nanowire channel. These two regimes are termed "atomic" and "Wigner" regimes and are characterized both by the ratio of Coulomb to single-particle energies per electron ($\gamma_E = E_{\text{Coul}}/\Delta E$) and channel length to screening length ($\gamma_L = L/\lambda$). In the Wigner regime, the Coulomb energy is relatively greater than the single-particle energy ($\gamma_E \gg 1$) and the screening length is small enough ($\gamma_L \gg 1$) to favor the spatial separation of the electrons in the nanowire, forming so-called Wigner molecules. This localization is lacking in the atomic regime, where the Coulomb energy is not large enough. Additionally, we present graphs of the electron density and the natural orbitals. Both cases A and B for the choice of eigenbasis of the statistical operator are studied, case B being specially interesting since it introduces a variation with respect to the original MCSCG method, which employs case A.

4.8.1. Energy estimations

Obtaining the energy ratio γ_E implies knowledge of the Coulomb and single-particle energies for a system of electrons in a nanowire channel, which cannot be supplied before the simulation is performed. Therefore, we employ auxiliary energy expressions, which have a simple analytical form and depend straightforwardly on the parameters of the system, to estimate the actual energies.

The difference ΔE between the first two energy levels resulting from considering the nanowire as a 1D infinite potential well is taken as an estimation of the single-particle energy, which reads as [106]

$$\Delta E = \frac{3}{8}\frac{N_e^2 h^2}{m^* L^2} \tag{4.64}$$

where $L_e = L/N_e$ and N_e is the number of electrons in the channel. The single-electron Coulomb charging energy as given by its classical expression $E_{\text{Coul}} = e^2/C_{\text{ox}}$ serves as an estimation for the Coulomb energy per electron, where C_{ox}

is the capacitance per electron for a coaxially gated NWFET and reads as [46]

$$C_{ox} = \frac{\pi \varepsilon_0 \varepsilon_{ch} d_{ch}^2 L_e}{4\lambda^2} \tag{4.65}$$

and the screening length λ is given by Eq. (1.1). Substituting the capacitance in the expression of the energy we get

$$E_{Coul} = \frac{4N_e e^2 \lambda^2}{\pi \varepsilon_0 \varepsilon_{ch} d_{ch}^2 L} \quad . \tag{4.66}$$

For a given nanowire channel and insulator material composition, the γ_E and γ_L ratios are determined by the length L and diameter d_{ch} of the channel, the oxide thickness d_{ox} and the electron number N_e, as these estimations show. Nevertheless, to study the transition from atomic to Wigner regimes, we choose N_e, d_{ch} and the ratios γ_E and γ_L as free variables, determining from them the parameters L, λ and d_{ox} by means of scaling equations. Forming the ratio γ_E with the quantities given by Eqs. (4.64) and (4.66) it is straightforward to express the nanowire channel length as

$$L = \left(\frac{3\pi^2}{32} N_e a_B d_{ch}^2 \gamma_E \gamma_L^2 \right)^{\frac{1}{3}} \tag{4.67}$$

where the Bohr radius is defined as

$$a_B = \frac{4\pi \varepsilon_0 \varepsilon_{ch} \hbar^2}{m^* e^2} \quad . \tag{4.68}$$

Once the nanowire length is determined, the screening length is obtained simply as

$$\lambda = \frac{L}{\gamma_L} \tag{4.69}$$

which can be used to determine the oxide thickness from Eq. (1.1) as

$$d_{ox} = \frac{d_{ch}}{2} \left(\exp\left(8 \frac{\varepsilon_{ox}}{\varepsilon_{ch}} \left(\frac{\lambda}{d_{ch}} \right)^2 \right) - 1 \right) \quad . \tag{4.70}$$

Note that d_{ox} increases exponentially with λ^2, so one must be careful with the choice of parameters so that the produced oxide thickness is kept within realistic limits.

γ_E	N_{sites}	L(nm)	d_{ox}(nm)
0.5	34	11.05	0.926
1	42	13.65	1.717
1.5	49	15.925	2.577
3	61	19.825	5.836
5	73	23.725	12.467
10	92	29.9	50.299

Table 4.2.: Parameters of the simulated systems.

4.8.2. System parameters and approach

We have chosen the following device parameters common to both regimes. The channel consists of a ZnO nanowire of diameter $d_{\text{ch}} = 3$ nm and lattice constant $a_0 = 3.25$ Å, electron effective mass $m^*/m_e = 0.29$ and a relative dielectric constant $\varepsilon_{\text{ch}} = 8.66$, as found in Ref. [85]. The channel and the gate are separated by a SiO_2 oxide layer of relative dielectric constant $\varepsilon_{\text{ox}} = 3.9$. The source and drain are contacted with a metal (Pt for example) to form Schottky barriers [24] of height $\Phi_{\text{SB}} = 0.7$ eV, which act as double tunnel barriers to confine the electrons in the nanowire. The temperature of the system is $T = 4.2$ K. Table 4.2 gathers the parameters particular to each simulation.

The choice of ZnO as nanowire material is motivated by its relatively large effective mass, which makes possible to select a relatively high γ_E corresponding to a relatively short L. Even if the lattice constant a_0 is not very large, the number $N_{\text{sites}} = L/a_0$ of localized orbitals (sites) can be kept low enough, so that the calculation time and memory are within reasonable limits.

The ratio of nanowire length L to screening length λ has been selected as $\gamma_L = 10$ for all the cases we have studied. In this way, λ is small enough to guarantee Wigner molecule formation, provided the ratio γ_E of estimated Coulomb to single-particle energy is large enough. The transition from one regime to the other has been performed by varying γ_E only, for six different values. This quantity determines L by application of Eq. (4.67), which in turn determines λ by Eq. (4.69) and as a result d_{ox} by Eq. (4.70). We have selected a voltage point with $V_{\text{DS}} = 0$ and $V_{\text{GS}} = 0.15\ V$, which corresponds to the center of the second Coulomb diamond, an equilibrium situation with the channel occupied by $N_e = 2$ electrons. The Coulomb diamond's scale and location depend on the parameters

of the system, therefore in principle one should adjust V_{GS} (with chosen $V_{DS} = 0$) in such a way that the voltage point belongs to the diamond in all the studied simulations. Nevertheless, the chosen value of V_{GS} corresponds in all cases to the second diamond.

4.8.3. Resulting statistical operator

The statistical operator with eigenbasis of Slater determinants of natural orbitals (case A), has the form of a pure state $\hat{\rho}_{\text{rel}} = |D_3\rangle \langle D_3|$ in five of the six performed simulations. Only the case with $\gamma_E = 3$ deviates from a pure state, with $\hat{\rho}_{\text{rel}} = w_3 |D_3\rangle \langle D_3| + w_{12} |D_{12}\rangle \langle D_{12}|$ being a mixture of the states $|D_3\rangle = |110000\cdots\rangle$ and $|D_{12}\rangle = |001100\cdots\rangle$, with weights $w_3 = 5.276 \times 10^{-1}$ and $w_{12} = 4.724 \times 10^{-1}$.

The statistical operator whose eigenbasis is chosen to be that of the eigenvectors of the projected many-body Hamiltonian (case B), has in all simulations the form of a pure state $\hat{\rho}_{\text{rel}} = |\psi\rangle \langle \psi|$ corresponding to a single many-body state $|\psi\rangle$. Table 4.3 displays the components $|\langle D_K | \psi\rangle|^2$ of the many-body state $|\psi\rangle$ in the basis of Slater determinants of natural orbitals for the six studied cases.

Most of the components follow a similar pattern. There is a single component with a value very near unity, corresponding to the same Slater determinant as in case A, while the remaining are relatively small. Therefore, the many-body state of the system for these simulations in case B, is almost a single Slater determinant. This indicates that employing an eigenbasis of Slater determinants of natural orbitals (case A) in these situations is a good choice of representation. On the other hand, the results corresponding to $\gamma_E = 3$ deviate from this pattern, since the highest valued component is not so near unity. Nevertheless, for this simulation there is a resemblance between cases B and A, in the sense that the highest components in case B correspond to the same Slater determinants in case A.

4.8.4. Natural orbitals

We have carefully chosen the thresholds that determine the classification of natural orbitals into occupied, fluctuating and empty, in such a way that the Fock subspace dimension is not drastically reduced. Even if the contribution of those

$\gamma_E = 0.5$	
$\lvert D_K\rangle$	$\lvert\langle D_K \mid \psi\rangle\rvert^2$
$\lvert\mathbf{11}0000\mathbf{0000}\rangle$	9.901087×10^{-1}
$\lvert\mathbf{00}0000\mathbf{1100}\rangle$	9.881239×10^{-3}
$\lvert\mathbf{00}0000\mathbf{0011}\rangle$	8.651753×10^{-6}

$\gamma_E = 1.5$	
$\lvert D_K\rangle$	$\lvert\langle D_K \mid \psi\rangle\rvert^2$
$\lvert\mathbf{11}0000\mathbf{0000}\rangle$	8.351109×10^{-1}
$\lvert\mathbf{00}0000\mathbf{1100}\rangle$	1.446486×10^{-1}
$\lvert\mathbf{00}0000\mathbf{0011}\rangle$	8.474243×10^{-3}
$\lvert\mathbf{01}0000\mathbf{0010}\rangle$	5.877250×10^{-3}
$\lvert\mathbf{10}0000\mathbf{0001}\rangle$	5.877197×10^{-3}
$\lvert\mathbf{00}0000\mathbf{0110}\rangle$	3.323030×10^{-6}
$\lvert\mathbf{00}0000\mathbf{1010}\rangle$	2.881298×10^{-6}
$\lvert\mathbf{00}0000\mathbf{1001}\rangle$	2.873206×10^{-6}
$\lvert\mathbf{00}0000\mathbf{0101}\rangle$	2.470142×10^{-6}

$\gamma_E = 5$	
$\lvert D_K\rangle$	$\lvert\langle D_K \mid \psi\rangle\rvert^2$
$\lvert\mathbf{11}0000\mathbf{0000}\rangle$	9.884781×10^{-1}
$\lvert\mathbf{00}0000\mathbf{1100}\rangle$	1.120697×10^{-2}
$\lvert\mathbf{10}0000\mathbf{0100}\rangle$	2.797392×10^{-4}
$\lvert\mathbf{01}0000\mathbf{1000}\rangle$	3.521542×10^{-5}

$\gamma_E = 1$	
$\lvert D_K\rangle$	$\lvert\langle D_K \mid \psi\rangle\rvert^2$
$\lvert\mathbf{11}0000\mathbf{0000}\rangle$	9.287014×10^{-1}
$\lvert\mathbf{00}0000\mathbf{1100}\rangle$	7.040752×10^{-2}
$\lvert\mathbf{00}0000\mathbf{0011}\rangle$	4.487365×10^{-4}
$\lvert\mathbf{01}0000\mathbf{0010}\rangle$	3.075678×10^{-4}
$\lvert\mathbf{10}0000\mathbf{0001}\rangle$	1.321041×10^{-4}
$\lvert\mathbf{10}0000\mathbf{0010}\rangle$	1.842873×10^{-6}

$\gamma_E = 3$	
$\lvert D_K\rangle$	$\lvert\langle D_K \mid \psi\rangle\rvert^2$
$\lvert\mathbf{1100}0000\mathbf{00}\rangle$	7.319653×10^{-1}
$\lvert\mathbf{0011}0000\mathbf{00}\rangle$	2.232429×10^{-1}
$\lvert\mathbf{0100}0000\mathbf{10}\rangle$	1.503594×10^{-2}
$\lvert\mathbf{1000}0000\mathbf{01}\rangle$	1.501137×10^{-2}
$\lvert\mathbf{0000}0000\mathbf{11}\rangle$	1.461581×10^{-2}
$\lvert\mathbf{0010}0000\mathbf{01}\rangle$	6.859462×10^{-5}
$\lvert\mathbf{0001}0000\mathbf{10}\rangle$	5.973664×10^{-5}

$\gamma_E = 10$	
$\lvert D_K\rangle$	$\lvert\langle D_K \mid \psi\rangle\rvert^2$
$\lvert\mathbf{11}0000\mathbf{0000}\rangle$	9.856718×10^{-1}
$\lvert\mathbf{00}0000\mathbf{1100}\rangle$	1.350063×10^{-2}
$\lvert\mathbf{01}0000\mathbf{1000}\rangle$	3.964802×10^{-4}
$\lvert\mathbf{00}0000\mathbf{0110}\rangle$	3.498175×10^{-4}
$\lvert\mathbf{00}0000\mathbf{1010}\rangle$	6.034784×10^{-5}
$\lvert\mathbf{01}0000\mathbf{0010}\rangle$	1.953227×10^{-5}
$\lvert\mathbf{10}0000\mathbf{1000}\rangle$	1.159658×10^{-6}

Table 4.3.: Components $\lvert\langle D_K \mid \psi\rangle\rvert^2 > 10^{-6}$ of the many-body state $\lvert\psi\rangle$ that characterizes the system for the six simulations in case B. Relevant natural orbitals are shown in boldface.

natural orbitals with very low occupation number is small, we preferred to include them so that the impact of the reduction of the Fock space is minimized within some limits.

In all the simulations the number of relevant natural orbitals is 6, so the Fock subspace dimension is 64. Figure 4.1 gathers them for case B. The first two (indices 0 and 1) have the highest occupation number ($\xi_i \sim 1$) and are of the highest relevance in determining the general features of the observables, as compared to the following four, with very small occupation numbers. This can be verified by comparing their shape (one peak or two peaks) with that of the electron density, as shown in Fig. 4.2.

Note that there is an index gap in all six situations. The missing natural orbitals correspond to fluctuating states but strongly coupled to the contacts, thus not being considered as relevant. For example, for $\gamma_E = 10$ these missing states have indices 2,3,4 and 5.

4.8.5. Total electron density

Figure 4.2 displays the total electron density for the system in equilibrium and the channel occupied by $N_e = 2$ electrons, as γ_E is increased. Examining the tendency of the density to develop two peaks from a single one, the transition from atomic to Wigner regime can be seen. Indeed, the two electrons in the channel separate as a consequence of the increased Coulomb interaction and a Wigner molecule emerges.

In any simulation, the densities corresponding to spin up and down are equal to each other, so they are not shown separately. Specifically in the Wigner regime, the two-peaked density associated with spin up coincides with that with spin down, spin symmetry is preserved. This is in accordance to Pauli's exclusion principle but may be counterintuitive, since one might expect both electrons to have definite and opposed spins, whereas there is no spin separation.

Note that if we had chosen to plot the densities against the absolute position x and not against the relative position x/L, the areas below the curves would have been the same and equal to the electron number. Cases A and B produce the same density profiles and therefore only case B is shown.

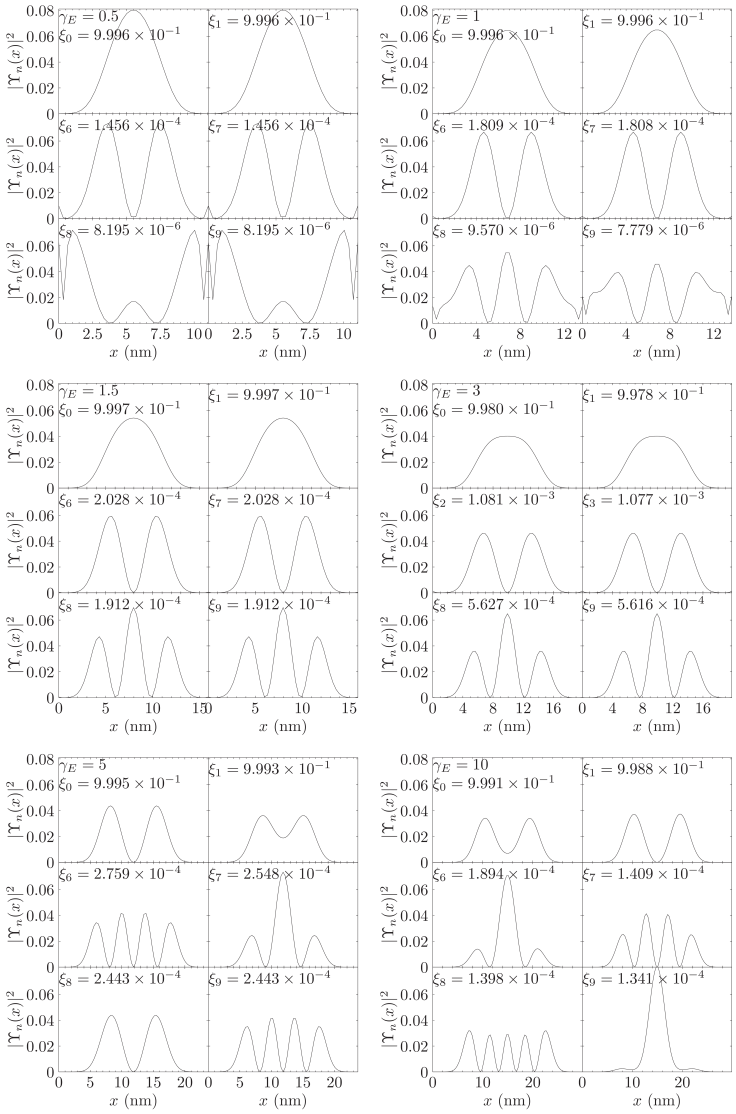

Figure 4.1.: The six relevant natural orbitals for all case B simulations (varying γ_E). Here we make the identification of $\Upsilon_n(x)$ with Υ_{xn}, the unitary matrix that diagonalizes ρ_1, where the column n corresponds to the nth natural orbital and the row to site x.

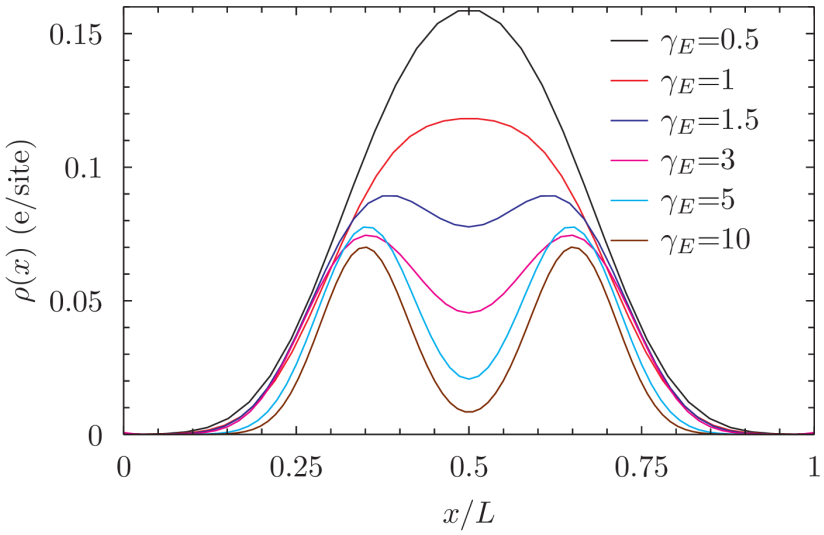

Figure 4.2.: Transition from "atomic" to "Wigner" regimes, as displayed by the total electron density for $N_e = 2$ and increasing Coulomb to single-particle energy ratio γ_E. As Coulomb repulsion gets larger, the electrons separate in two different peaks.

4.8.6. Density–density correlation

The transition from atomic to Wigner regime is also revealed in the density–density correlation κ_{ij}, as defined by Eq. (4.55). This quantity is calculated for all possible spin values: $\kappa^{\uparrow\uparrow}$, $\kappa^{\uparrow\downarrow}$, $\kappa^{\downarrow\downarrow}$ and $\kappa^{\downarrow\uparrow}$. Since there is no physical reason for spin symmetry to be broken (no applied magnetic field, for example), the following identities hold: $\kappa^{\downarrow\downarrow} = \kappa^{\uparrow\uparrow}$ and $\kappa^{\downarrow\uparrow} = \kappa^{\uparrow\downarrow}$, as numerically verified. Therefore, only $\kappa^{\uparrow\downarrow}$ and $\kappa^{\uparrow\uparrow}$ are considered here.

Figure 4.3 shows the $\kappa^{\uparrow\downarrow}$ correlation of the six simulations for case A. The first two graphs ($\gamma_E = 0.5$ and 1) indicate that in the atomic regime, where there is no visible charge separation, the correlation between electron densities for spin up and spin down is almost zero. At the onset of the Wigner regime ($\gamma_E = 1.5, 3, 5$ and 10), $\kappa^{\uparrow\downarrow} < 0$ takes appreciable negative values around the areas corresponding to the two density peaks. Two simultaneous measurements of the density with opposite spins around the same peaks are negatively correlated, meaning that the deviations of the measured density from its mean value for opposite spins have opposite signs. There is a relatively high probability that one increases while the other decreases. There is no significant $\kappa^{\uparrow\downarrow}$ correlation in case

A outside these regions.

A comparison between the $\kappa^{\uparrow\downarrow}$ correlation as displayed in Fig. 4.3 for case A and Fig. 4.4 for case B, clearly shows that case B is able to capture more features and differences exist between the two cases. Most noticeable is the appearance of regions with positive correlation. In the atomic regime ($\gamma_E = 0.5$ and 1), these regions correspond to sites positioned in different halves of the nanowire channel. For two simultaneous density measurements of opposite spin, positive correlation implies a relatively high probability of either an increase or a decrease with respect to the mean value in both observables. For sites located in the same half of the channel the correlation is negative. As γ_E increases, the shape of the correlation changes continually, from a "quadrupole-like" to a "dipole-like" geometry, where the negative areas concentrate around two peaks and the positive areas get smaller.

Figure 4.5 shows the $\kappa^{\uparrow\uparrow}$ correlations for case A. The diagonal elements are omitted, since their value is unity and they are not relevant. In this case, $\kappa^{\uparrow\uparrow}$ is significantly nonzero in all simulations. As the Wigner regime sets on, there is a transition from a single area with negative correlation to two separated localized regions. Outside these areas $\kappa^{\uparrow\uparrow} \sim 0$ is not appreciable. Except for the simulations corresponding to $\gamma_E = 0.5$ and 1, a comparison with Fig. 4.3 shows that $\kappa^{\uparrow\uparrow} \propto \kappa^{\uparrow\downarrow}$ for case A.

Figure 4.6 shows the $\kappa^{\uparrow\uparrow}$ correlations for case B. The first two graphs ($\gamma_E = 0.5$ and 1) corresponding to the atomic regime, coincide with those for case A. The following two graphs ($\gamma_E = 1.5$ and 3) feature four rounded regions in a square arrangement with negative correlation. Finally, the $\kappa^{\uparrow\uparrow}$ correlation for $\gamma_E = 5$ and 10 coincides with the $\kappa^{\uparrow\downarrow}$ correlation (both for case B).

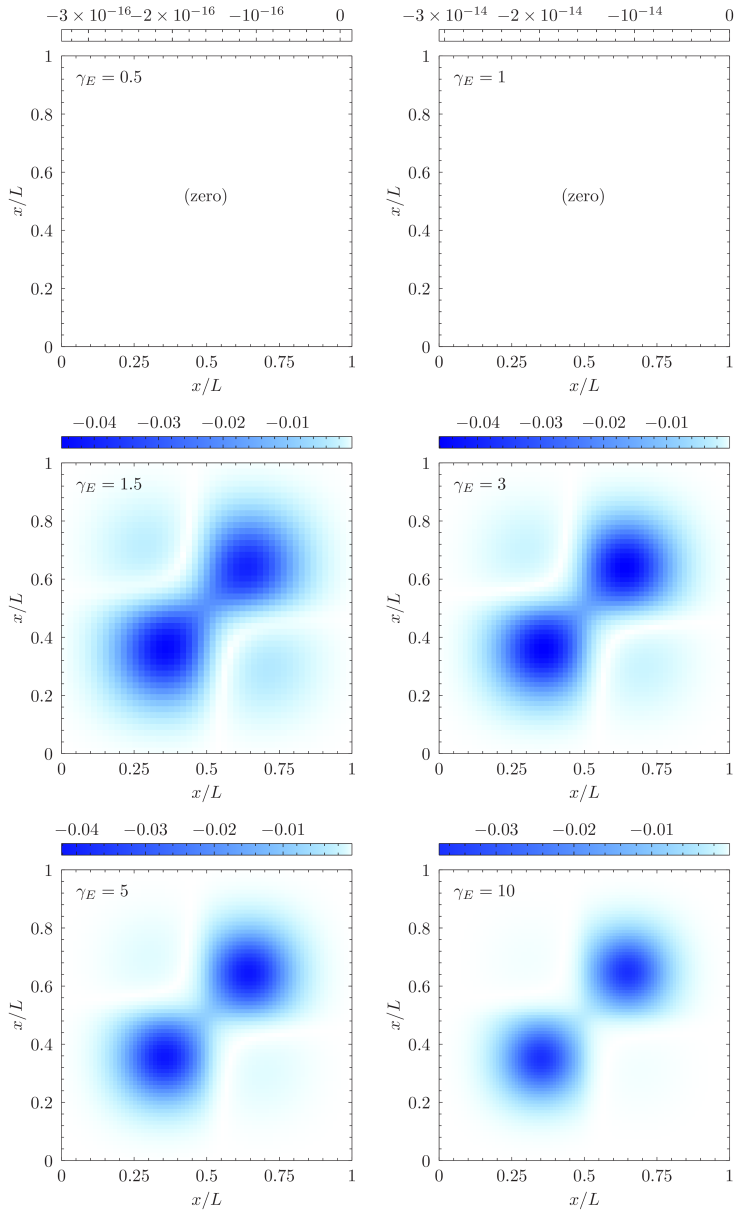

Figure 4.3.: Case A: $\kappa^{\uparrow\downarrow}$ correlation from "atomic" to "Wigner" regimes.

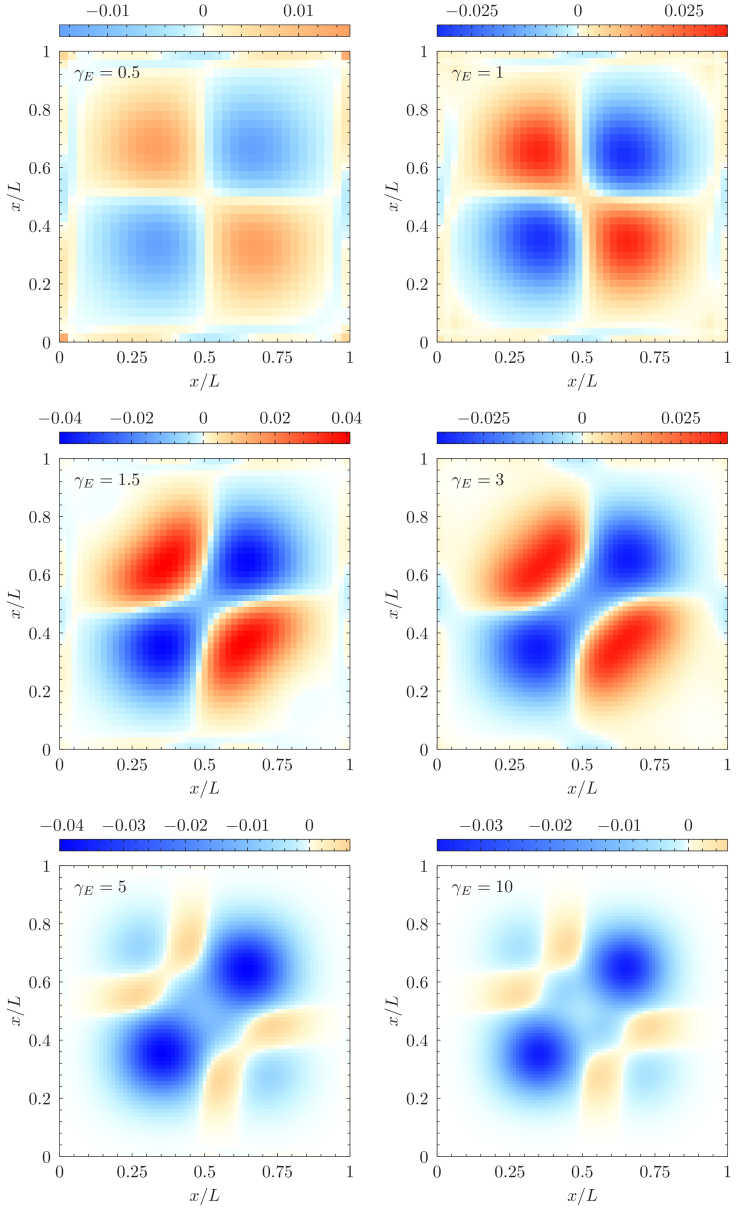

Figure 4.4.: Case B: $\kappa^{\uparrow\downarrow}$ correlation from "atomic" to "Wigner" regimes.

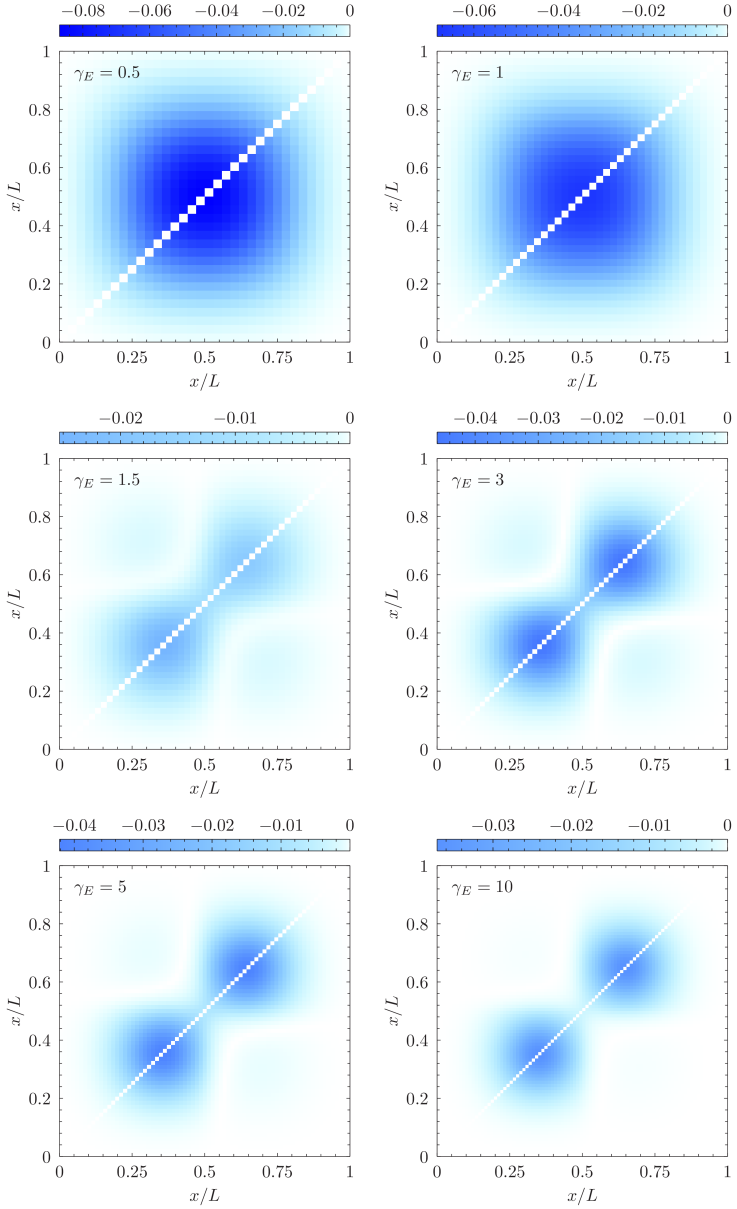

Figure 4.5.: Case A: $\kappa^{\uparrow\uparrow}$ correlation from "atomic" to "Wigner" regimes.

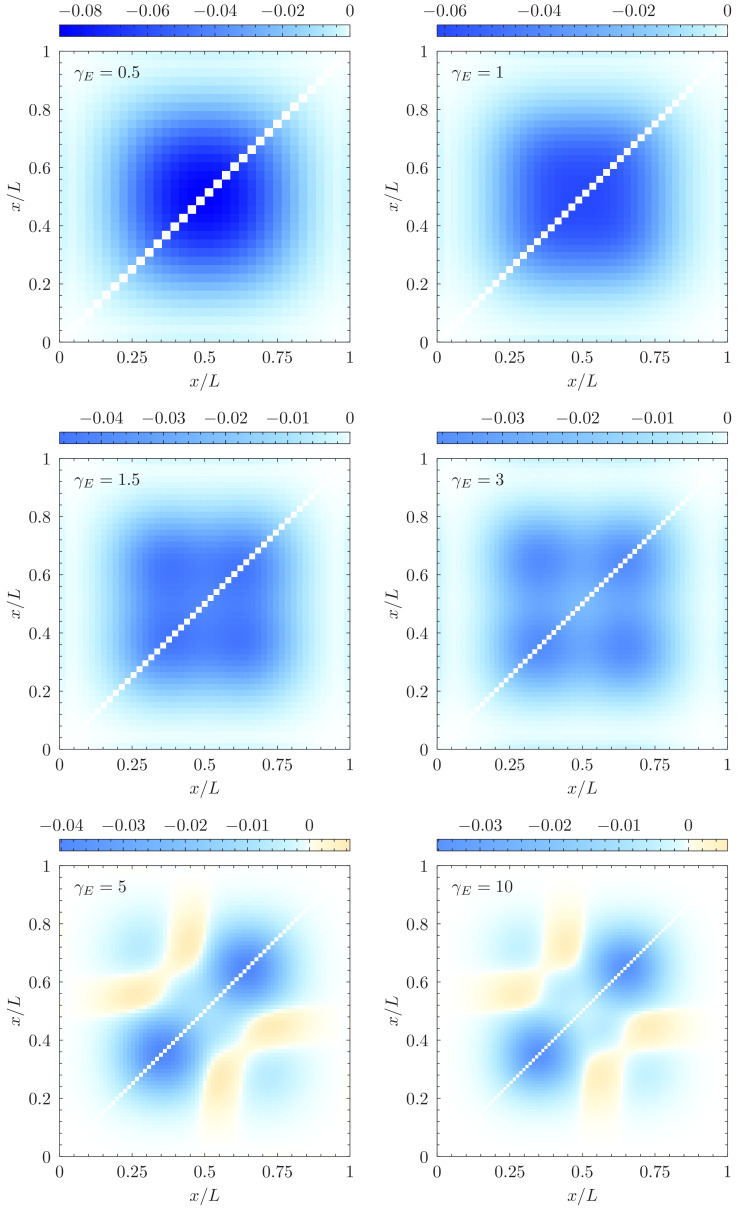

Figure 4.6.: Case B: $\kappa^{\uparrow\uparrow}$ correlation from "atomic" to "Wigner" regimes.

5. Correlation entropy

5.1. Introduction

As an application of the method for numerically determining the non-equilibrium many-body statistical operator described in Chapter 4 and as an interesting topic in itself, we study in the following Sections the issue of quantifying the correlation of interacting electrons in the channel of a NWFET. A Fock space state that cannot be written as a Slater determinant with respect to any single-particle basis is called a "correlated" many-body state. Note that a Slater determinant with respect to a given basis may be written in terms of a superposition of multiple Slater determinants with respect to a different single-particle basis. Therefore, more than one Slater determinant in an expansion does not imply that the state is correlated.

The topic of correlation in many-electron systems for the case where the preparation of the system is given by a pure state has been studied by several authors. It has been shown [107, 108, 109, 110] that the single-particle-reduced entropy S_1 as given by the single-particle density matrix [79] ρ_1 can be interpreted as a measure of correlation for such pure states. If the preparation of the system is given by a mixture of states, S_1 also depends on the degree of mixture [111, 112] and so this quantity is no longer suitable as a measure of correlation alone.

Several relative measures of correlation have been reported [113, 114], that quantify correlation of a many-electron state by comparing it to that of an uncorrelated state. In this Chapter, for a system whose preparation is described by a given many-body statistical operator (see Chapter 4), we consider a modified correlation entropy $\Delta S \equiv \widetilde{S} - S$ [111, 100] as a measure of correlation, which is the difference between two entropies. Here, S is the von Neumann entropy as calculated from the statistical operator $\hat{\rho}_{\mathrm{rel}}$ of the system, providing a measure of mixture. $\widetilde{S}$ is the von Neumann entropy as calculated from a statistical op-

erator $\widetilde{\rho}_{\mathrm{rel}}$ that resembles $\hat{\rho}_{\mathrm{rel}}$ optimally, but whose eigenbasis consists of Slater determinants built from an optimized single-particle orthonormal basis, obtained in such a way that $\widetilde{S}$ is minimized.

In Sec. 5.2, an overview on the single-particle-reduced entropy is given and in Sec. 5.3 the von Neumann entropy is described, before the modified correlation entropy is introduced in Sec. 5.4. In the following sections the determination of the modified correlation entropy is addressed, to end up with some results illustrating its features in Sec. 5.9.

5.2. Single-particle-reduced entropy

The single-particle-reduced entropy (in bit) is defined as [108, 111]

$$S_1 \equiv -\mathrm{Tr}(\rho_1 \log_2 \rho_1) \tag{5.1}$$

where ρ_1 is the single-particle density matrix [79] of the system. In quantum chemistry, S_1 is referred to as the correlation entropy [108, 110] for pure many-body states. Expanded in terms of the natural orbital basis, S_1 can be written as $S_1 = -\sum_i \xi_i \log_2 \xi_i$, where ξ_i denote the eigenvalues of ρ_1. In general, S_1 indicates the deviation from a single Slater determinant of the preparation of the system, due to correlation, mixture or both. For the case of a single Slater determinant, ρ_1 would have only eigenvalues 0 and 1, therefore $S_1 = 0$ in this case. Note that we interpret $0 \log_2 0 = 0$. As considered in previous chapters as case A, the NWFET channel is described by a mixture of a few relevant Slater determinants of natural orbitals with detailed Coulomb interaction and a non-relevant rest which is treated on a mean-field level. Then, S_1 measures the degree of mixture of the system's preparation. This feature provides additional information about the many-body state of the channel beyond its current–voltage characteristics.

We have simulated electronic transport in the Coulomb blockade regime by means of the MCSCG approach [112] for case A (chosen eigenbasis of relevant Slater determinants of natural orbitals for the statistical operator, see Sec. 4.3.4) and the same system as in Sec. 3.7, with Schottky barriers of height $\Phi_{\mathrm{SB}} = 0.2$ eV with respect to the Fermi energy of the contacts. Figure 5.1 shows the simulated characteristics which clearly exhibit a correspodence between the

Point	N_e	Shell	(V_{GS}, V_{DS})	S_1	Slater dets.	w_N
A: Empty channel	0	Empty	(0.034, 0)	0.074	$\|000000\rangle$	1
B: 1st Diamond	1	Open	(0.15, 0)	1.07	$\|100000\rangle$	0.502
					$\|010000\rangle$	0.498
C: Non-equilibrium state			(0.23, 0.026)	0.908	$\|100000\rangle$	0.363
					$\|010000\rangle$	0.361
					$\|110000\rangle$	0.276
D: 2nd Diamond	2	Closed	(0.285, 0)	0.079	$\|110000\rangle$	1
E: 3rd Diamond	3	Open	(0.405, 0)	1.102	$\|110000\rangle$	0.024
					$\|111000\rangle$	0.489
					$\|110100\rangle$	0.487

Table 5.1.: Data from selected points in the diagrams. The table shows the electron number N_e, shell filling, voltage coordinates (V_{GS}, V_{DS}), single-particle-reduced entropy S_1, the dominant Slater determinants and their associated weights $\{w_N\}$.

Coulomb diamonds in the current–voltage characteristics and certain diamond-like shaped structures in the entropy diagram.

Table 5.1 gathers information obtained by means of the MCSCG formalism, corresponding to different voltage points in Fig. 5.1. Point A is associated with an empty channel ($N_e = 0$), whose state is given by the vacuum state with unity weight. $S_1 \simeq 0$ in this case, indicating that the degree of mixture of the preparation is minimum.

Point B corresponds to the first diamond ($N_e = 1$). Here, the single electron in the channel has the chance to occupy one of the two states in the first single-particle energy level: with spin up or with spin down (open shell configuration). This is reflected in the two Slater determinants with almost equal weights $w_1 \simeq w_2 \simeq 0.5$ that describe the state of the system. $S_1 \simeq 1$ and therefore the degree of mixture is higher than in the empty channel case.

A non-equilibrium state is described in point C by three Slater determinants with similar weights $w_1 \simeq w_2 \simeq w_3 \simeq 0.3$. This situation shows that it is equally probable in this state to find an electron in the first single-particle energy level with spin up or down, or two electrons with both spin directions.

Point D corresponds to the second diamond ($N_e = 2$). Each electron occupies the first single-particle energy level with spin up and down respectively. Therefore, there is only one Slater determinant to describe this situation and so its weight is unity. $S_1 \simeq 0$ as in the case of an empty channel. Again, the degree of mixture

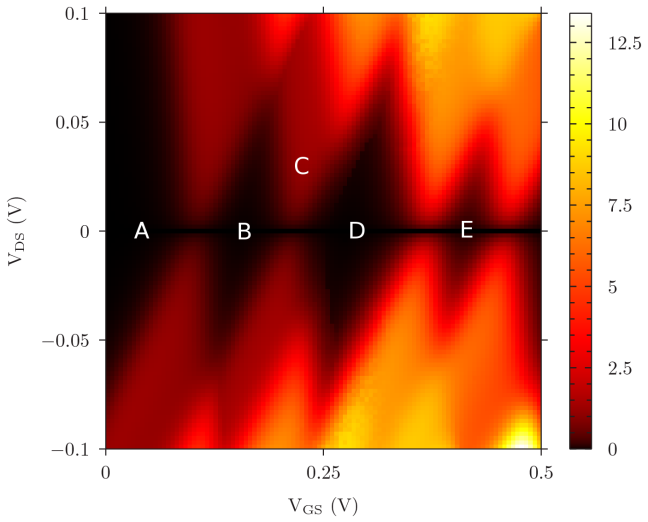

(a) Absolute value of the drain current $|I_D|$ (nA).

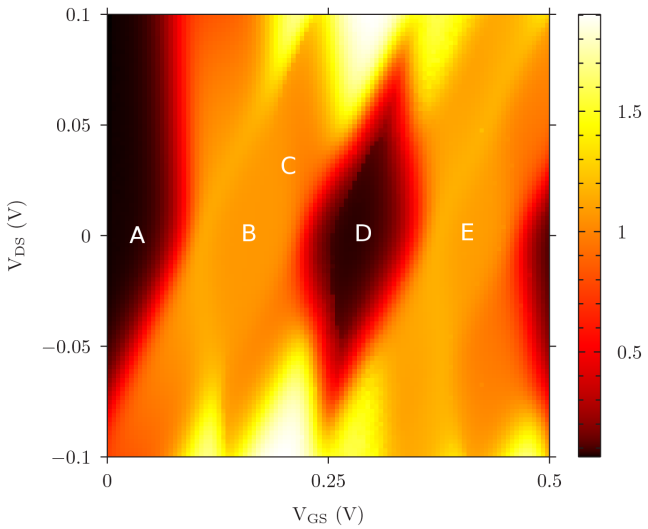

(b) Single-particle-reduced entropy S_1 (bit).

Figure 5.1.: Simulated current–voltage characteristics (a) and single-particle-reduced entropy (b).

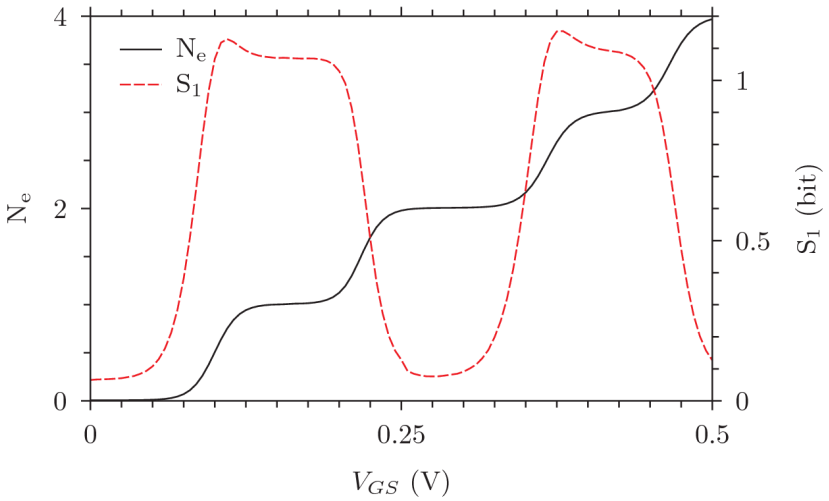

Figure 5.2.: Electron number N_e and single-particle-reduced entropy S_1 (bit) as a function of V_{GS} for fixed $V_{DS} = 0$.

is minimum.

Finally, point E shows the case of the third diamond ($N_e = 3$), very similar to that of the first diamond. Here, two electrons occupy the first single-particle energy level, and a third one has both possibilities of spin occupation in the second single-particle energy level. Although there is a small contribution from a doubly occupied Slater determinant, the last two determinants are the main contributors ($w_1 \simeq 0$, $w_2 \simeq w_3 \simeq 0.5$). The fact that S_1 is slightly higher than one reflects that the first determinant also plays a minor role.

All of the near-equilibrium cases corresponding to Coulomb diamonds that we have analyzed can be summarized in Fig. 5.2, in which N_e and S_1 are plotted against V_{GS} for fixed $V_{DS} = 0$. The N_e curve exhibits integer charging steps. On the other hand, S_1 oscillates approximately between zero and one. It can be seen here that $S_1 \simeq 0$ for $N_e \simeq 0$ and 2, corresponding to an empty channel and the second Coulomb diamond (closed shell configuration) respectively, described by only one Slater determinant, as shown in Table 5.1. Whereas $S_1 \simeq 1$ for $N_e \simeq 1$ and 3, corresponding to the first and third diamonds (open shell configurations) with more than one Slater determinant. One has to note that the rest of the system (outside the relevant Fock subspace) also contributes to S_1, leading to slightly increased values.

5.3. von Neumann entropy

The many-body statistical operator in its general form reads as

$$\hat{\rho}_{\text{rel}} = \sum_{J=0}^{\dim(\mathcal{F}_{\text{rel}})-1} w_J \left|\rho_J\right\rangle \left\langle\rho_J\right| \tag{5.2}$$

and its eigenstates $|\rho_J\rangle$ can be expressed in the many-body basis of Slater determinants of relevant natural orbitals $\mathcal{B}_{\text{rel}} = \{|D_I\rangle\}$ of the relevant many-body Fock subspace $\mathcal{F}_{\text{rel}}$ through the unitary transformation Λ as

$$\left|\rho_J\right\rangle = \sum_{K=0}^{\dim(\mathcal{F}_{\text{rel}})-1} \Lambda_{KJ} \left|D_K\right\rangle \quad . \tag{5.3}$$

Once $\hat{\rho}_{\text{rel}}$ of the system is known, by means of the numerical method described in Chapter 4 for example, the von Neumann entropy [115] (in bit) can be obtained as follows

$$S = -\text{Tr}(\hat{\rho}_{\text{rel}} \log_2 \hat{\rho}_{\text{rel}}) = -\sum_{J=0}^{\dim(\mathcal{F}_{\text{rel}})-1} w_J \log_2(w_J) \tag{5.4}$$

which is a measure of the mixture degree of the system's preparation. If a state is pure (only one weight is unity $w_J = 1$ and the rest are zero $w_{K\neq J} = 0$) the von Neumann entropy vanishes, otherwise $S > 0$.

5.4. Modified correlation entropy

For pure states ($S = 0$) a measure of correlation is obtained by the single-particle-reduced entropy S_1 [107, 108, 109, 110], which has the disadvantage of depending also on the mixture degree [111, 112]. In order to avoid this contribution due to mixture, we consider the so called "modified correlation entropy" [111, 100] which is defined as

$$\Delta S \equiv \widetilde{S} - S \tag{5.5}$$

where S is the von Neumann entropy as a function of $\hat{\rho}_{\text{rel}}$ and

$$\widetilde{S} \equiv -\text{Tr}(\widetilde{\rho}_{\text{rel}} \log_2 \widetilde{\rho}_{\text{rel}}) = -\sum_{I=0}^{\dim(\mathcal{F}_{\text{rel}})-1} \widetilde{w}_I \log_2(\widetilde{w}_I) \tag{5.6}$$

is the entropy for a modified many-body statistical operator

$$\widetilde{\rho}_{\text{rel}} = \sum_{I=0}^{\dim(\mathcal{F}_{\text{rel}})-1} \widetilde{w}_I \left|\widetilde{D}_I\right\rangle \left\langle\widetilde{D}_I\right| \tag{5.7}$$

which is diagonal in the many-body orthonormal basis $\widetilde{\mathcal{B}}_{\text{rel}} = \left\{\left|\widetilde{D}_I\right\rangle\right\}$ of the relevant many-body Fock subspace $\mathcal{F}_{\text{rel}}$. Here, $\left|\widetilde{D}_I\right\rangle$ are Slater determinants built from an optimized single-particle orthonormal basis, chosen in such a way that $\widetilde{S}$ is minimized.

The connection between the many-body basis $\widetilde{\mathcal{B}}_{\text{rel}}$ and the many-body basis $\mathcal{B}_{\text{rel}} = \{|D_I\rangle\}$ of relevant Slater determinants of natural orbitals, is given by the Fock-space unitary transformation $\widetilde{\Lambda}$, with $\dim(\mathcal{F}_{\text{rel}}) \times \dim(\mathcal{F}_{\text{rel}}) = 2^{N_{\text{rel}}} \times 2^{N_{\text{rel}}}$ components $\widetilde{\Lambda}_{JI} = \left\langle D_J \middle| \widetilde{D}_I \right\rangle$ that depend directly on the unitary transformation $\mathcal{U}$ between the optimized single-particle basis and the natural orbital basis. This implies that

$$\left|\widetilde{D}_I\right\rangle = \sum_{J=0}^{\dim(\mathcal{F}_{\text{rel}})-1} \widetilde{\Lambda}_{JI} \left|D_J\right\rangle \quad . \tag{5.8}$$

The projection weights $\widetilde{w}_I$ are defined as

$$\widetilde{w}_I \equiv \left\langle \hat{P}_I \right\rangle = \text{Tr}\left(\hat{\rho}_{\text{rel}} \left|\widetilde{D}_I\right\rangle \left\langle\widetilde{D}_I\right|\right) = \left\langle\widetilde{D}_I\right| \hat{\rho}_{\text{rel}} \left|\widetilde{D}_I\right\rangle \tag{5.9}$$

where the projectors read as $\hat{P}_I \equiv \left|\widetilde{D}_I\right\rangle \left\langle\widetilde{D}_I\right|$. The last equation shows that the projection weights are the diagonal elements of $\hat{\rho}_{\text{rel}}$ in the basis $\widetilde{\mathcal{B}}_{\text{rel}}$. Inserting Parseval's identity (within the relevant Fock subspace) in the appropriate places, they can be expressed as

$$\widetilde{w}_I = \sum_N w_N |\Xi_{IN}|^2 \tag{5.10}$$

where $\Xi_{IN} = \sum_{K=0}^{\dim(\mathcal{F}_{\text{rel}})-1} \widetilde{\Lambda}_{KI} \Lambda^*_{KN}$ and $\Lambda_{KN} = \langle D_K \,|\, \rho_N \rangle$. We see that in order to determine the projection weights we need to obtain the amplitudes $\widetilde{\Lambda}_{KI} = \left\langle D_K \middle| \widetilde{D}_I \right\rangle$ between Slater determinants in both bases $\mathcal{B}_{\text{rel}}$ and $\widetilde{\mathcal{B}}_{\text{rel}}$, assuming the unitary transformation Λ is known.

5.5. Single-particle basis unitary transformation

If we denote $c_i^\dagger$ and c_i (without tilde) as the creation and annihilation operators in the natural orbital basis and $\widetilde{c}_i^\dagger$ and $\widetilde{c}_i$ (with tilde) as those in the optimized single-particle basis, their relation is given by [42]

$$\widetilde{c}_i^\dagger = \sum_{j=0}^{N_{\text{max}}-1} \mathcal{U}_{ji} c_j^\dagger \tag{5.11a}$$

$$\widetilde{c}_i = \sum_{j=0}^{N_{\text{max}}-1} \mathcal{U}_{ji}^* c_j \quad . \tag{5.11b}$$

In the case that the relevant natural orbitals are contiguous in index range, without loss of generality, the unitary transformation $\mathcal{U}$ between the optimized single-particle basis and the natural orbital basis has the following structure

$$\mathcal{U} = \begin{pmatrix} I_{N_{\text{occ}} \times N_{\text{occ}}} & 0 & 0 \\ 0 & U_{N_{\text{rel}} \times N_{\text{rel}}} & 0 \\ 0 & 0 & I_{N_{\text{rest}} \times N_{\text{rest}}} \end{pmatrix} \tag{5.12}$$

and differs from the identity matrix I just for a square block U of dimensions $N_{\text{rel}} \times N_{\text{rel}}$ which operates within the relevant single-particle space.

5.6. Determination of the many-body basis unitary transformation

$\widetilde{\Lambda}$ is obtained by individually calculating its components $\widetilde{\Lambda}_{JI} = \left\langle D_J \middle| \widetilde{D}_I \right\rangle$. It can be seen that they are nonzero only if the number of occupied states in the left and right Slater determinants is the same. The number $\Omega_{\text{c}}(N_{\text{rel}})$ of nonzero components $\widetilde{\Lambda}_{JI}$ as a function of the relevant states can be obtained with the following formula

$$\Omega_{\text{c}}(N_{\text{rel}}) = \sum_{N_e=0}^{N_{\text{rel}}} \binom{N_{\text{rel}}}{N_e}^2 \tag{5.13}$$

where $\binom{N}{M} \equiv N!/(M!(N-M)!)$ and $\binom{N_{\text{rel}}}{N_e}$ counts the number of many-body states with N_e occupied relevant single-particle states.

Two equivalent methods to obtain $\widetilde{\Lambda}$ and therefore the projection weights $\widetilde{w}_I$ are described in the following, together with their respective performances.

5.6.1. Method 1

In the first approach, the Slater determinant $\left|\widetilde{D}_I\right\rangle \in \widetilde{\mathcal{B}}_{\text{rel}}$ is expressed in terms of creation operators in the single-particle optimized basis acting on the vacuum state. Then these operators are expressed as linear combinations of those in the natural orbital basis, according to Eq. (5.11a). $\langle D_J|$ is written also in terms of annihilation operators in the natural orbital basis acting on the vacuum state. As a result $\widetilde{\Lambda}_{JI}$ is obtained as a linear combination of expectation values of strings of annihilation and creation operators in the natural orbital basis with respect to the vacuum state. By considering that an annihilation operator acting on the vacuum state yields zero and by employing the anti-commutation relations valid for Fermions given by Eqs. (2.2) to move the annihilation operators to the right, the strings of operators is decomposed, finally producing a sum of products of Kronecker deltas which select specific combinations of elements of U that can be expressed as determinants.

As an example, we consider the case of $N_{\text{rel}} = 2$ relevant single-particle states and no fixed fully occupied states ($N_{\text{occ}} = 0$). A many-body basis $\mathcal{B}_{\text{rel}} = \{|00\rangle, |10\rangle, |01\rangle, |11\rangle\}$ of the relevant Fock-subspace of dimension $\dim(\mathcal{F}_{\text{rel}}) = 4$ results. This implies that the total number of components $\widetilde{\Lambda}_{JI}$ is 16, out of which $\Omega_c(2) = 6$ are nonzero. We obtain them by direct calculation.

$$\left\langle 00 \middle| \widetilde{00} \right\rangle = \langle \text{vac} \,|\, \text{vac} \rangle = 1 \tag{5.14a}$$

$$\left\langle 10 \middle| \widetilde{10} \right\rangle = \sum_{i=0}^{1} U_{i0} \langle \text{vac}| \underbrace{c_0 c_i^\dagger}_{\delta_{0i} - c_i^\dagger c_0} |\text{vac}\rangle = U_{00} \tag{5.14b}$$

$$\left\langle 01 \middle| \widetilde{10} \right\rangle = \sum_{i=0}^{1} U_{i0} \langle \text{vac}| \underbrace{c_1 c_i^\dagger}_{\delta_{1i} - c_i^\dagger c_1} |\text{vac}\rangle = U_{10} \tag{5.14c}$$

$$\left\langle 10 \middle| \widetilde{01} \right\rangle = \sum_{j=0}^{1} U_{j1} \langle \text{vac}| \underbrace{c_0 c_j^\dagger}_{\delta_{0j} - c_j^\dagger c_0} |\text{vac}\rangle = U_{01} \tag{5.14d}$$

$$\left\langle 01 \middle| \widetilde{01} \right\rangle = \sum_{j=0}^{1} U_{j1} \langle \text{vac}| \underbrace{c_1 c_j^\dagger}_{\delta_{1j} - c_j^\dagger c_1} |\text{vac}\rangle = U_{11} \tag{5.14e}$$

$$\left\langle 11 \middle| \widetilde{11} \right\rangle = \sum_{i,j=0}^{1} U_{i0} U_{j1} \langle \text{vac}| \underbrace{c_0 c_1 c_j^\dagger c_i^\dagger}_{\delta_{0i}\delta_{1j} - \delta_{0j}\delta_{1i}} |\text{vac}\rangle = U_{00}U_{11} - U_{01}U_{10} = \begin{vmatrix} U_{00} & U_{01} \\ U_{10} & U_{11} \end{vmatrix} \tag{5.14f}$$

The vacuum state is assumed to be the same in both representations. Also note that the amplitude $\widetilde{\Lambda}_{33}$ (see Eq. (5.14f)) can be expressed as a 2×2 determinant. The resulting matrix $\widetilde{\Lambda}$ reads as

$$\widetilde{\Lambda} = \begin{pmatrix} 1 & 0 & 0 & 0 \\ 0 & U_{00} & U_{01} & 0 \\ 0 & U_{10} & U_{11} & 0 \\ 0 & 0 & 0 & U_{00}U_{11} - U_{01}U_{10} \end{pmatrix} \quad . \tag{5.15}$$

The amplitudes corresponding to the cases with $N_{\text{occ}} = 0$ and $N_{\text{occ}} > 0$ are equal, for the same number N_{rel} of relevant states. This can be seen by realizing that the creation operator for a fixed fully occupied state i is invariant $\widetilde{c}_i^\dagger = c_i^\dagger$, since $\mathcal{U}$ is the identity outside the $N_{\text{rel}} \times N_{\text{rel}}$ subspace. The corresponding annihilation operator c_i appearing in the expression for the amplitude can be moved by anti-commutation an even number of times to the right up to the position of $c_i^\dagger$, without generating extra terms. This is because the creation operators on the right of c_i, resulting from the transformation U, have indices outside the $[0, N_{\text{occ}} - 1]$ interval. Since $\{c_i, c_i^\dagger\} = 1$, moving c_i one more time generates a term which does not involve the state i and a term which is zero, since c_i anti-commutes with the rest of the creation operators and can be moved to the last position, where $c_i |\text{vac}\rangle = 0$. When this is done for all N_{occ} annihilation operators, we see that the amplitude for the case of having $N_{\text{occ}} > 0$ fix fully occupied states reduces to that for $N_{\text{occ}} = 0$.

5.6.2. Method 2

In the second approach the Slater determinant $\left|\widetilde{D}_I\right\rangle \in \widetilde{\mathcal{B}}_{\text{rel}}$ is written in terms of creation operators in the optimized single-particle basis, similarly to the first

approach. But this time the many-body matrix representations of operators in the relevant Fock-subspace $\mathcal{F}_{\text{rel}}$, as spanned by the basis $\mathcal{B}_{\text{rel}}$, are employed. First the matrix representation of the creation operators $c_i^\dagger$ in this basis is constructed. Then using U they are transformed and the matrices associated with the operators $\widetilde{c}_i^\dagger$ are obtained. Finally, these matrices are applied to the vacuum state as ordered products to produce the components of all Slater determinants $\left|\widetilde{D}_I\right\rangle$ of single-particle states belonging to the optimized basis. Each of their components is directly an amplitude $\left\langle D_J \middle| \widetilde{D}_I \right\rangle$ and therefore an element of the matrix $\widetilde{\Lambda}$.

To illustrate the method, and to compare with the previous results, we consider again the case of $N_{\text{rel}} = 2$ relevant states and no fixed fully occupied states ($N_{\text{occ}} = 0$). As a result $\dim(\mathcal{F}_{\text{rel}}) = 4$ and $\mathcal{B}_{\text{rel}} = \{|00\rangle, |10\rangle, |01\rangle, |11\rangle\}$. Each Slater determinant is characterized by a different pattern of two bits, which is the binary representation of its corresponding unique integer index $I = 0, 1, 2, 3$. Using this index convention, the matrix elements of the two creation operators in the natural orbital basis are given by

$$\left(c_i^\dagger\right)_{IJ} = \langle D_I | \, c_i^\dagger \, | D_J \rangle \tag{5.16}$$

where $i = 0, 1$ and $I, J = 0, 1, 2, 3$. By direct calculation involving the anti-commutation relations for Fermions, it can be seen that these are the following integer 4×4 matrices

$$c_0^\dagger = \begin{pmatrix} 0 & 0 & 0 & 0 \\ 1 & 0 & 0 & 0 \\ 0 & 0 & 0 & 0 \\ 0 & 0 & -1 & 0 \end{pmatrix} \quad , \quad c_1^\dagger = \begin{pmatrix} 0 & 0 & 0 & 0 \\ 0 & 0 & 0 & 0 \\ 1 & 0 & 0 & 0 \\ 0 & 1 & 0 & 0 \end{pmatrix} \quad . \tag{5.17}$$

Applying Eq. (5.11a), the operators are related as follows

$$\widetilde{c}_0^\dagger = U_{00} c_0^\dagger + U_{10} c_1^\dagger \tag{5.18a}$$

$$\widetilde{c}_1^\dagger = U_{01} c_0^\dagger + U_{11} c_1^\dagger \tag{5.18b}$$

which in matrix representation read as

$$\widetilde{c}_0^\dagger = \begin{pmatrix} 0 & 0 & 0 & 0 \\ U_{00} & 0 & 0 & 0 \\ U_{10} & 0 & 0 & 0 \\ 0 & U_{10} & -U_{00} & 0 \end{pmatrix} \quad , \quad \widetilde{c}_1^\dagger = \begin{pmatrix} 0 & 0 & 0 & 0 \\ U_{01} & 0 & 0 & 0 \\ U_{11} & 0 & 0 & 0 \\ 0 & U_{11} & -U_{01} & 0 \end{pmatrix} \quad . \tag{5.19}$$

Finally, in order to obtain the Slater determinants $\left|\widetilde{D}_I\right\rangle$ in terms of the $|D_J\rangle$, the matrices corresponding to $\widetilde{c}_0^\dagger$ and $\widetilde{c}_1^\dagger$ are applied to the vacuum state $|\text{vac}\rangle = (1,0,0,0)$, which is assumed to be the same in both representations. The resulting transformed relevant many-body states read as

$$\left|\widetilde{00}\right\rangle = |\text{vac}\rangle = \begin{pmatrix} 1 \\ 0 \\ 0 \\ 0 \end{pmatrix} = |00\rangle \tag{5.20a}$$

$$\left|\widetilde{10}\right\rangle = \widetilde{c}_0^\dagger |\text{vac}\rangle = \begin{pmatrix} 0 \\ U_{00} \\ U_{10} \\ 0 \end{pmatrix} = U_{00} |10\rangle + U_{10} |01\rangle \tag{5.20b}$$

$$\left|\widetilde{01}\right\rangle = \widetilde{c}_1^\dagger |\text{vac}\rangle = \begin{pmatrix} 0 \\ U_{01} \\ U_{11} \\ 0 \end{pmatrix} = U_{01} |10\rangle + U_{11} |01\rangle \tag{5.20c}$$

$$\left|\widetilde{11}\right\rangle = \widetilde{c}_1^\dagger \widetilde{c}_0^\dagger |\text{vac}\rangle = \begin{pmatrix} 0 \\ 0 \\ 0 \\ U_{00}U_{11} - U_{01}U_{10} \end{pmatrix} = (U_{00}U_{11} - U_{01}U_{10}) |11\rangle \tag{5.20d}$$

which form an orthonormal basis of the Fock-subspace $\mathcal{F}_{\text{rel}}$, as can be seen by

considering that $\left\langle \widetilde{00} \middle| \widetilde{00} \right\rangle = \langle \mathrm{vac} | \mathrm{vac} \rangle = 1$,

$$\begin{pmatrix} \left\langle \widetilde{10} \middle| \widetilde{10} \right\rangle & \left\langle \widetilde{10} \middle| \widetilde{01} \right\rangle \\ \left\langle \widetilde{01} \middle| \widetilde{10} \right\rangle & \left\langle \widetilde{01} \middle| \widetilde{01} \right\rangle \end{pmatrix} = \begin{pmatrix} |U_{00}|^2 + |U_{10}|^2 & U_{00}^* U_{01} + U_{10}^* U_{11} \\ U_{01}^* U_{00} + U_{11}^* U_{10} & |U_{01}|^2 + |U_{11}|^2 \end{pmatrix} = \\ = U^\dagger U = I \tag{5.21}$$

and

$$\left\langle \widetilde{11} \middle| \widetilde{11} \right\rangle = \det(U^\dagger U) = \det(I) = 1 \tag{5.22}$$

which follows from the unitary character of the transformation U. Since the rest of amplitudes involve Slater determinants with different number of occupied states, they are zero. In agreement with the first method, the matrix $\widetilde{\Lambda}$ reads as

$$\widetilde{\Lambda} = \begin{pmatrix} 1 & 0 & 0 & 0 \\ 0 & U_{00} & U_{01} & 0 \\ 0 & U_{10} & U_{11} & 0 \\ 0 & 0 & 0 & U_{00}U_{11} - U_{01}U_{10} \end{pmatrix} \quad . \tag{5.23}$$

We can verify again that the amplitudes corresponding to the cases $N_{\mathrm{occ}} = 0$ and $N_{\mathrm{occ}} > 0$ are equal, for the same number N_{rel} of relevant states. We only have to replace the role of the vacuum state $|\mathrm{vac}\rangle$ as a reference state by that of the Slater determinant with all the relevant states empty $\left| 1 \cdots 1 \overset{N_{\mathrm{occ}}}{0} \cdots 0 \overset{N_{\mathrm{rel}}}{} \right\rangle$. Assuming this Slater determinant is normalized, we have

$$\left| \widetilde{1} \cdots \widetilde{1} \overset{N_{\mathrm{occ}}}{\widetilde{0}} \cdots \widetilde{0} \overset{N_{\mathrm{rel}}}{} \right\rangle = \begin{pmatrix} 1 \\ 0 \\ \vdots \\ 0 \end{pmatrix} = \left| 1 \cdots 1 \overset{N_{\mathrm{occ}}}{0} \cdots 0 \overset{N_{\mathrm{rel}}}{} \right\rangle \quad . \tag{5.24}$$

5.6.3. Numerical performance of both methods

The performance of both methods is estimated by considering the most complex case where $\hat{\rho}$ is composed of the maximum number of relevant many-body states, that is $w_J > 0,\ \forall J = 0, \ldots, 2^{N_{\mathrm{rel}}} - 1$. The number of elemental operations

$\Omega_{\text{op}}(N_{\text{rel}})$ needed to obtain all the amplitudes for each method is evaluated. Elemental operations are defined as the real products that arise in the lowest level of computation as a consequence of multiplying the complex elements of U. Note that the product of two complex numbers involves four products of real numbers.

For the first method the following formula is obtained

$$\Omega_{\text{op1}}(N_{\text{rel}}) = 4 \sum_{N_e=2}^{N_{\text{rel}}} (N_e - 1) N_e! \binom{N_{\text{rel}}}{N_e}^2 \tag{5.25}$$

which can be understood by counting as follows

- Number of Slater determinants with N_e occupied relevant single-particle states: $\binom{N_{\text{rel}}}{N_e}$
- Number of determinants from these Slater determinants: $\binom{N_{\text{rel}}}{N_e}^2$
- Number of sums in a $N_e \times N_e$ determinant: $N_e!$
- Number of real products in a single complex term of the sums: $4 \times (N_e - 1)$

The formula for the second method has two main contributions and reads as

$$\Omega_{\text{op2}}(N_{\text{rel}}) = N_{\text{rel}}^2 2^{2N_{\text{rel}}+1} + 2^{2(N_{\text{rel}}+1)} \sum_{N_e=2}^{N_{\text{rel}}} N_e \binom{N_{\text{rel}}}{N_e} \tag{5.26}$$

The first contribution takes into account the number of elemental products involved in the matrix representation calculations as given by Eq. (5.11a). Specifically we have:

- Number of creation operators $c_i^\dagger$ in natural orbital basis: N_{rel}
- Number of products of a complex U_{ij} and the integer matrix elements of $c_i^\dagger$: $2 \times 2^{N_{\text{rel}}} \times 2^{N_{\text{rel}}}$
- Number of creation operators $\widetilde{c}_i^\dagger$ in optimized basis: N_{rel}

The second contribution counts the number of elemental products involved in the construction of the Slater determinants $\left|\widetilde{D}_I\right\rangle \in \widetilde{\mathcal{B}}$ once all matrix representations have been performed. The counting is as follows:

- Number of combinations of N_e matrices of a total of N_{rel}: $\binom{N_{\text{rel}}}{N_e}$

N_{rel}	Ω_{op1}	Ω_{op2}	$\Omega_{\mathrm{op2}}/\Omega_{\mathrm{op1}}$
2	8	256	32.00
3	120	3 456	28.80
4	1 344	36 864	27.43
5	14 720	358 400	24.35
6	169 320	3 342 336	19.74
7	2 088 408	30 507 008	14.61
8	27 749 120	274 726 912	9.90
9	396 831 744	2 448 949 248	6.17
10	6 090 196 680	21 642 608 640	3.55

Table 5.2.: Number of elemental operations involved in both methods to obtain $\widetilde{\Lambda}$.

- Number of vector-matrix multiplications: N_e
- Number of real products in one complex vector-matrix multiplication: $4 \times 2^{N_{\mathrm{rel}}} \times 2^{N_{\mathrm{rel}}}$

The number of elemental operations for both methods are listed in Table 5.2. Both methods have been compared numerically for verification and provide the same results.

5.7. Determination of the unitary transformation of the single-particle basis

The objective of the calculations is to obtain a single-particle basis unitary transformation U such that the projection weights $\widetilde{\mathbf{w}}$ associated to the Slater determinants of single-particle states belonging to the basis determined by U, yield a minimum entropy $\widetilde{S}$. This is a numerical optimization task, which can be carried on by a genetic algorithm (GA), an overview of which is given in Appendix B.

Any unitary transformation matrix with $N \times N$ elements can be univocally parametrized by a set of $N \times N$ angles, by virtue of the parametrization method introduced by Murnaghan [116], an overview of which is given in Appendix C. So in the GA, the optimization variables are chosen as the set of angles that parametrize univocally U. The objective function to be minimized is chosen to be $\widetilde{S}$, as given by Eq. (5.6) with the projection weights $\widetilde{\mathbf{w}}$ determined by Eq. (5.10).

5.8. Identification of a truly correlated state

At first sight, a particular many-body state $|\rho_K\rangle$ of $\hat{\rho}_{\text{rel}}$ may appear to deviate from being a Slater determinant, if it displays several components in the basis $\mathcal{B}_{\text{rel}}$ above a threshold of relevance, and not just one with a value close to unity. Nonetheless, that may not be the case in the basis $\widetilde{\mathcal{B}}_{\text{rel}}$, where this state may have the character of a Slater determinant, and therefore is actually not a correlated state.

In order to identify such a situation, we propose to calculate the expectation value of the number operator $\widetilde{n}_i = \widetilde{c}_i^\dagger \widetilde{c}_i$ in the optimized single-particle basis, with respect to each many-body state $|\rho_K\rangle$ of $\hat{\rho}_{\text{rel}}$. We find two alternative ways to perform this calculation, which produce the same results. First, we can transform the operators into the natural orbital basis and the state into the basis $\mathcal{B}_{\text{rel}}$, to produce

$$\langle \rho_K | \, \widetilde{n}_i \, | \rho_K \rangle = \sum_{J,L=0}^{\dim(\mathcal{F}_{\text{rel}})-1} \Lambda^*_{LK} \Lambda_{JK} \sum_{j,l=0}^{N_{\text{max}}-1} \mathcal{U}^*_{li} \, \mathcal{U}_{ji} \, \langle D_L | \, c_j^\dagger c_l \, | D_J \rangle \quad . \tag{5.27}$$

As a second approach, we choose to express the state in the basis $\widetilde{\mathcal{B}}_{\text{rel}}$, resulting in the following expression

$$\begin{aligned} \langle \rho_K | \, \widetilde{n}_i \, | \rho_K \rangle &= \sum_{J,L=0}^{\dim(\mathcal{F}_{\text{rel}})-1} \Lambda^*_{LK} \Lambda_{JK} \, \langle D_L | \, \widetilde{n}_i \, | D_J \rangle = \\ &= \sum_{J,L=0}^{\dim(\mathcal{F}_{\text{rel}})-1} \Lambda^*_{LK} \Lambda_{JK} \sum_{P,Q=0}^{\dim(\mathcal{F}_{\text{rel}})-1} \widetilde{\Lambda}^*_{JP} \widetilde{\Lambda}_{LQ} \left\langle \widetilde{D}_P \right| \widetilde{n}_i \left| \widetilde{D}_Q \right\rangle = \\ &= \sum_{J,L=0}^{\dim(\mathcal{F}_{\text{rel}})-1} \Lambda^*_{LK} \Lambda_{JK} \sum_{P=0}^{\dim(\mathcal{F}_{\text{rel}})-1} \widetilde{\Lambda}^*_{JP} \widetilde{\Lambda}_{LP} \widetilde{N}_i \left(\left| \widetilde{D}_P \right\rangle \right) \end{aligned} \tag{5.28}$$

where $\widetilde{N}_i \left(\left| \widetilde{D}_P \right\rangle \right)$ denotes the occupation number (0 or 1) of the single-particle state i of the optimized basis with respect to the Slater determinant $\left| \widetilde{D}_P \right\rangle \in \widetilde{\mathcal{B}}_{\text{rel}}$.

Furthermore, we propose a suitable measure to check if all the expectation values $\langle \rho_K | \, \widetilde{n}_i \, | \rho_K \rangle \equiv \widetilde{n}_i[K]$, for a given K and varying i, are close to zero or one (Slater determinant) or if the deviate from these extreme values (correlated state). It reads as $\widetilde{S}_1[K] = -\sum_i \widetilde{n}_i[K] \log_2 \widetilde{n}_i[K]$ and has an equivalent nature as

	Equilibrium	Non-equilibrium
V_{GS} (V)	0.15	0.4
V_{DS} (V)	0	0.1
I_D (nA)	0	0.167
N_e	2	~ 4
N_{occ}	0	0
N_{rel}	6	6

Table 5.3.: Characteristics of the equilibrium and non-equilibrium voltage points.

the single-particle-reduced entropy S_1 (which is evaluated from the natural orbital occupation numbers ξ_i). If all $\widetilde{n}_i[K] \in \{0, 1\}$, a value of $\widetilde{S}_1[K] = 0$ follows.

5.9. Results

In case A, the statistical operator describes the state of the system as a mixture of Slater determinants of natural orbitals. As such, the von Neumann entropy reflects its degree of mixture. We have verified that the modified correlation entropy ΔS is zero in this case, as expected since a mixture of Slater determinants presents no correlation.

More interesting is case B, where the statistical operator is expressed in the eigenbasis of the many-body Hamiltonian projected to the relevant Fock subspace. We have analyzed two conditions, equilibrium ($V_{DS} = 0$) and non-equilibrium ($V_{DS} > 0$), intermediate between atomic and Wigner regimes, corresponding to $\gamma_E = 3$ and $\gamma_L = 10$, as specified in Sec. 4.8.2 and Table 4.2. The same system is chosen for both cases, only varying the voltage points, as Table 5.3 shows.

The equilibrium many-body state results in a pure state (von Neumann entropy $S = 0$) due to very low T, as described by the statistical operator $\hat{\rho}_{rel} = |\psi\rangle \langle\psi|$, whose components are given in Table 5.4. A first look at the components indicates that this state $|\psi\rangle$ deviates from a Slater determinant in the basis $\mathcal{B}_{rel}$ of Slater determinants of relevant natural orbitals, since there is not a single component with a value close to unity and the rest zero. The calculation of the single-particle-reduced entropy produces $S_1 = 9.126 \times 10^{-2}$, whereas the modified correlation entropy reads as $\Delta S = 9.760 \times 10^{-1}$.

On the other hand, the non-equilibrium many-body state results in a mixture of

$\lvert D_K \rangle$	$\lvert \langle D_K \lvert \psi \rangle \rvert^2$
$\lvert \mathbf{1100}0000\mathbf{00} \rangle$	7.319546×10^{-1}
$\lvert \mathbf{0011}0000\mathbf{00} \rangle$	2.232534×10^{-1}
$\lvert \mathbf{1000}0000\mathbf{10} \rangle$	1.503611×10^{-2}
$\lvert \mathbf{0100}0000\mathbf{01} \rangle$	1.501195×10^{-2}
$\lvert \mathbf{0000}0000\mathbf{11} \rangle$	1.461471×10^{-2}
$\lvert \mathbf{0010}0000\mathbf{01} \rangle$	6.865919×10^{-5}
$\lvert \mathbf{0001}0000\mathbf{10} \rangle$	5.997900×10^{-5}

Table 5.4.: Pure many-body state components $\lvert \langle D_K \lvert \psi \rangle \rvert^2 > 10^{-6}$ for equilibrium point. Relevant natural orbitals are shown in boldface.

four states, as reflected by the statistical operator $\hat{\rho}_{\text{rel}} = \sum_{N=0}^{3} w_N \lvert \psi_N \rangle \langle \psi_N \rvert$. The corresponding weights and the components of the eigenstates $\lvert \psi_N \rangle$ are shown in Table 5.5. One can verify that their components are closer to those corresponding to a Slater determinant than in the equilibrium case. Nevertheless, this is a mixed many-body state and this fact is reflected by the von Neumann entropy $S = 1.173$, a value significantly larger than zero. Also, the single-particle-reduced entropy $S_1 = 1.271$, exhibits a higher value as compared to the equilibrium case. Indeed, S_1 accounts not only for correlation but also for mixture degree. In contrast, the modified correlation entropy $\Delta S = 1.452 \times 10^{-2}$ is much smaller, resembling the fact that the eigenstates of the many-body statistical operator are very close to Slater determinants.

The resulting ΔS for the discussed non-equilibrium case is lower than for the discussed equilibrium case, even though in the non-equilibrium case the mixture degree of the system's preparation is higher than in the equilibrium case. This stands in agreement with the idea that ΔS is indeed a measure of correlation alone, independently of the mixture degree, in contrast to S_1.

In order to analyze the degree of deviation of the many-body states $\lvert \psi_N \rangle$ of $\hat{\rho}_{\text{rel}}$ from single Slater determinants, the expectation values of the occupation numbers $\widetilde{n}_i$ (corresponding to optimized single-particle states, see Sec. 5.8), are shown for the equilibrium and non-equilibrium points, in Tables 5.6 and 5.7 respectively. Inspection of these tables shows that for the equilibrium point, $\langle \psi \rvert \widetilde{n}_i \lvert \psi \rangle$ deviates from the extreme values 0 and 1 significantly for all six single-particle states, indicating that the many-body state deviates from being a Slater determinant.

$w_0 = 7.347524 \times 10^{-1}$		$w_1 = 1.403755 \times 10^{-1}$	
$\|D_K\rangle$	$\|\langle D_K \,\|\, \psi_0\rangle\|^2$	$\|D_K\rangle$	$\|\langle D_K \,\|\, \psi_1\rangle\|^2$
$\|111100\rangle$	9.836548×10^{-1}	$\|111010\rangle$	9.807315×10^{-1}
$\|110101\rangle$	1.231713×10^{-2}	$\|110011\rangle$	1.253150×10^{-2}
$\|111010\rangle$	2.672775×10^{-3}	$\|110110\rangle$	2.502412×10^{-3}
$\|001111\rangle$	7.726548×10^{-4}	$\|111100\rangle$	2.274014×10^{-3}
$\|110011\rangle$	2.818157×10^{-4}	$\|110101\rangle$	1.678201×10^{-3}
$\|100111\rangle$	1.144070×10^{-4}	$\|111001\rangle$	1.608453×10^{-4}
$\|011011\rangle$	1.064737×10^{-4}	$\|101011\rangle$	7.775216×10^{-5}
$\|111001\rangle$	4.882806×10^{-5}	$\|011011\rangle$	2.301173×10^{-5}
$\|101011\rangle$	1.045020×10^{-5}	$\|011110\rangle$	1.424845×10^{-5}
$\|010111\rangle$	9.505482×10^{-6}	$\|101110\rangle$	4.803740×10^{-6}
$\|110110\rangle$	5.660192×10^{-6}	$\|010111\rangle$	1.086428×10^{-6}
$\|011110\rangle$	1.916602×10^{-6}	$w_3 = 1.801348 \times 10^{-2}$	
$\|101101\rangle$	1.571994×10^{-6}	$\|D_K\rangle$	$\|\langle D_K \,\|\, \psi_3\rangle\|^2$
$\|011101\rangle$	1.353062×10^{-6}	$\|110011\rangle$	9.695261×10^{-1}
$w_2 = 1.068586 \times 10^{-1}$		$\|111010\rangle$	1.377540×10^{-2}
$\|D_K\rangle$	$\|\langle D_K \,\|\, \psi_2\rangle\|^2$	$\|111001\rangle$	7.337772×10^{-3}
$\|110101\rangle$	9.807050×10^{-1}	$\|110110\rangle$	6.102984×10^{-3}
$\|111100\rangle$	1.265844×10^{-2}	$\|110101\rangle$	2.525311×10^{-3}
$\|110011\rangle$	3.235242×10^{-3}	$\|111100\rangle$	4.151672×10^{-4}
$\|111001\rangle$	2.203150×10^{-3}	$\|101101\rangle$	7.754029×10^{-5}
$\|111010\rangle$	9.769919×10^{-4}	$\|011110\rangle$	7.197020×10^{-5}
$\|010111\rangle$	1.178670×10^{-4}	$\|101011\rangle$	5.581797×10^{-5}
$\|101101\rangle$	7.633732×10^{-5}	$\|011011\rangle$	3.832239×10^{-5}
$\|110110\rangle$	1.657535×10^{-5}	$\|100111\rangle$	2.104038×10^{-5}
$\|011101\rangle$	6.856518×10^{-6}	$\|001111\rangle$	1.931576×10^{-5}
$\|100111\rangle$	2.307765×10^{-6}	$\|010111\rangle$	1.462401×10^{-5}
$\|011110\rangle$	1.038164×10^{-6}	$\|101110\rangle$	1.066728×10^{-5}

Table 5.5.: Mixed many-body state components $|\langle D_K \,|\, \psi_J\rangle|^2 > 10^{-6}$ for non-equilibrium point.

On the other hand, for the non-equilibrium point, these values are much closer to 0 and 1. This shows that these many-body states are much closer to single Slater determinants. These facts are reflected in the measure $\widetilde{S}_1$ of deviation from single Slater determinant (see Sec. 5.8), which has a higher value in the equilibrium case compared to the non-equilibrium case.

$\widetilde{S}_1 = 1.842036$
$\widetilde{n}_0 = 2.233573 \times 10^{-1}$
$\widetilde{n}_1 = 7.469910 \times 10^{-1}$
$\widetilde{n}_2 = 1.883295 \times 10^{-2}$
$\widetilde{n}_3 = 7.578098 \times 10^{-1}$
$\widetilde{n}_8 = 2.233578 \times 10^{-1}$
$\widetilde{n}_9 = 2.965127 \times 10^{-2}$

Table 5.6.: $\langle\psi|\,\widetilde{n}_i\,|\psi\rangle$ and $\widetilde{S}_1$ for the equilibrium case. Note that for this many-body state, the quantities $\widetilde{n}_i$ are neither near zero nor one, but in between. Therefore the measure $\widetilde{S}_1$ is relatively high, and so is the degree of correlation.

$\widetilde{S}_1[0] = 3.403052 \times 10^{-2}$	$\widetilde{S}_1[1] = 3.670238 \times 10^{-2}$
$\widetilde{n}_0[0] = 9.995616 \times 10^{-1}$	$\widetilde{n}_0[1] = 9.986425 \times 10^{-1}$
$\widetilde{n}_1[0] = 9.991081 \times 10^{-1}$	$\widetilde{n}_1[1] = 9.999616 \times 10^{-1}$
$\widetilde{n}_2[0] = 1.849549 \times 10^{-3}$	$\widetilde{n}_2[1] = 9.980165 \times 10^{-1}$
$\widetilde{n}_3[0] = 9.991022 \times 10^{-1}$	$\widetilde{n}_3[1] = 9.999206 \times 10^{-1}$
$\widetilde{n}_4[0] = 9.990541 \times 10^{-1}$	$\widetilde{n}_4[1] = 1.884835 \times 10^{-3}$
$\widetilde{n}_5[0] = 1.324423 \times 10^{-3}$	$\widetilde{n}_5[1] = 1.574017 \times 10^{-3}$
$\widetilde{S}_1[2] = 3.789003 \times 10^{-2}$	$\widetilde{S}_1[3] = 1.332848 \times 10^{-1}$
$\widetilde{n}_0[2] = 1.431692 \times 10^{-3}$	$\widetilde{n}_0[3] = 7.628653 \times 10^{-3}$
$\widetilde{n}_1[2] = 9.998741 \times 10^{-1}$	$\widetilde{n}_1[3] = 9.998478 \times 10^{-1}$
$\widetilde{n}_2[2] = 2.166739 \times 10^{-3}$	$\widetilde{n}_2[3] = 9.919029 \times 10^{-1}$
$\widetilde{n}_3[2] = 9.999182 \times 10^{-1}$	$\widetilde{n}_3[3] = 9.998045 \times 10^{-1}$
$\widetilde{n}_4[2] = 9.979671 \times 10^{-1}$	$\widetilde{n}_4[3] = 8.206616 \times 10^{-3}$
$\widetilde{n}_5[2] = 9.986422 \times 10^{-1}$	$\widetilde{n}_5[3] = 9.926095 \times 10^{-1}$

Table 5.7.: $\widetilde{n}_i[K] = \langle\psi_K|\,\widetilde{n}_i\,|\psi_K\rangle$ and $\widetilde{S}_1[K]$ for the non-equilibrium case. Note that the values of the different quantities $\widetilde{n}_i[K]$ are either very near one or very near zero, therefore the measure $\widetilde{S}_1[K]$ is quite low for all many-body states $|\psi_K\rangle$. This is indicative of low correlation.

6. Summary

In this dissertation, the multi-configurational self-consistent Green's function method for the simulation of non-equilibrium electronic transport in a nanowire field-effect transistor has been augmented with new features, resulting in a new open-source simulation package named **NWFET-Lab**. This package has been the basis of the calculations performed in this work.

An adaptive numerical approach to determine a reduced non-equilibrium many-body statistical operator for quasi-isolated electronic states within the channel of a realistic nanowire field-effect transistor has been presented. In this approach, the statistical operator must satisfy a set of constraints related to the single-particle density matrix, as obtained from a non-equilibrium Green's function self-consistent calculation. Furthermore, since the number of constraints is in general smaller than the number of unknowns, a form for its eigenvalues or weights that maximizes the entropy has been chosen. As an alternative to the Slater determinants of relevant natural orbitals employed in the original multi-configurational self-consistent Green's function implementation, the eigenstates of the projected many-body Hamiltonian have also been used as eigenbasis of the statistical operator. As an application, the onset of formation of Wigner molecules has been discussed by means of the calculation of the electronic density–density correlation.

A new numerical determination of the correlation of the system of electrons within the nanowire channel of the device, for pure as well as for mixed states, has been presented. In contrast to the single-particle-reduced entropy, this so-called "modified correlation entropy" accounts for the correlation independently of the mixture degree of the many-body state, as given by the statistical operator and measured by the von Neumann entropy. An analysis of these three concepts of entropy has been performed. We compared an equilibrium pure state with a non-equilibrium mixed state and showed that in the considered example the modified correlation entropy was lower in the mixed state, a fact that indicates the capability of this new entropy determination method to capture correlation

beyond mixture.

The present work can be further extended in several directions. Electron–phonon interaction can be modeled by suitable self-energies within the non-equilibrium Green's function formalism. Also within this formalism, the possibility exists to describe the Coulomb interaction with a higher order approximation. The single-band tight-binding description of the nanowire channel can be extended to include multiple bands and inter-valley scattering by the inclusion of additional states in the 1D single-particle localized basis. Furthermore, a better approximation than nearest neighbor hopping can be considered, as well as an alternative derivation of the tight-binding description which takes into account more realistic single-particle orbitals, like localized Wannier functions, and more realistic energy bands by means, for example, of the $k \cdot p$ method.

As further investigations within the framework of the method employed in this dissertation, the impact of single dopants in the channel on the performance of the nanowire transistor can be addressed. This is a topic being actively researched in the present by means of methods that usually do not take into account a detailed many-body description of Coulomb interaction beyond mean-field. New light could be thrown to such a topic, specially in regimes where few-electron charging effects play an important role, like the Coulomb blockade regime.

Appendices

A. NWFET-Lab: Simulation package

A.1. Overview

NWFET-Lab [82] is a new simulation package with the aim to provide nanoelectronics researchers with a tool by means of which to setup a NWFET system, calculate and display its electronic transport properties. Set as one of the main objectives of this dissertation, it spans over 30000 lines of code. Its elaboration has been carried out with the help of a group of libraries and application programming interfaces (APIs) [117, 118, 119, 120, 121, 122] in the C++ language [123] and benefits from multithread parallel computation and 3D accelerated graphics capabilities. It is an open-source, multiplatform software package that has been shown to run under Linux and Windows operating systems. It can be redistributed and/or modified under the terms of the GNU General Public License version 2 [124].

NWFET-Lab is structured in three different and interdependent modules, each of which serves a specific purpose in the workflow of simulating electronic transport in a NWFET. It is based on a jobfile which contains the list of parameters that define the system. In order for the user to find easy configuration of these parameters a setup module has been implemented. It provides both an interface to edit the jobfile and also graphs to get a better idea of the characteristics of the system.

Once the jobfile is saved to disk, it can be opened by the calculation module. This is the module that implements the MCSCG method and took its machinery from **whiskersim** [81], only to be adapted from the C programming language [125] to C++ and augmented with new features. Quantities like the electron current and density or the single-particle-reduced entropy are calculated by this mod-

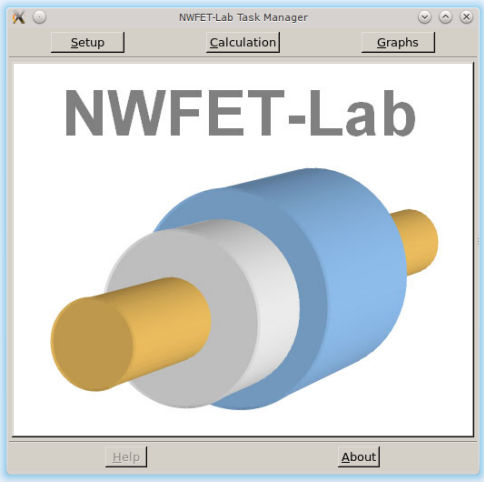

Figure A.1.: Screenshot of the task manager.

ule, either for a single or for a whole array of voltage points, optionally doing the calculations in parallel if the computer provides several CPUs or a multicore architecture. The results are output in data files.

The data files with the results of the simulation are displayed with the graphical module. 2D graphs, 3D graphs and colormaps allow the user to easily analyze the quantities obtained with the calculation module. Selectable axes can be used to plot different variables against each other. If the computer provides a 3D graphics acceleration card with a graphics processing unit (GPU), use is made of it thanks to the OpenGL API [120].

A.2. Structure

A.2.1. Task manager

The three modules may be launched from a task manager. It is a simple interface with a button associated to each module. Once a button is pressed the corresponding module opens and the task manager is minimized. The use of the task manager is optional, each module may be opened independently by running its executable file.

A.2.2. Setup module

Running the setup module is the first step in order for the user to be able to start a simulation. Not only does it provide access to the parameters that define the system, but also to those that are related to the calculation algorithm itself.

The user has the option to create a new jobfile with standard parameters given by default or to open an existing jobfile for editing it. Reading a jobfile is accomplished by means of a parser, a tool that allows the efficient detection of parameter tags and their corresponding values. Once this is done, the list of parameters opens in a new window by pressing the button labeled "Edit jobfile". For a description of the meaning of the parameters the reader is referred to section A.3 in this Appendix.

Another option of the setup module is the displaying of useful graphs to give a better image of the system being setup. This can be done by pressing the button labeled "Show graphs". A window opens then, with four tabs on it. With the first tab a customizable 3D view of the NWFET is displayed, with the possibility to enable or disable drawing its various parts. The second and third tabs are associated to 2D graphs for setting up the doping and the background potential. These graphs are editable, the user can modify the values of each point with the mouse. The fourth tab shows a 2D graph with the total potential profile along the NWFET channel and selectable gate–source and drain–source voltages.

The last option is to save the jobfile, an action performed by pressing the button labeled "Save jobfile". Once the jobfile is saved it can be opened with the calculation module.

A.2.3. Calculation module

The calculation module is the physical core of **NWFET-Lab** since it implements the MCSCG method for non-equilibrium electronic transport simulation in NWFETs. A C++ adapted and augmented version of **whiskersim** [81] is used as main calculation algorithm that depends as an input on the parameters listed in the jobfile edited with the setup module. The user is able to load the jobfile by pressing a button and once this is done several options can be adjusted that affect the calculation.

The functionality of a NWFET relies on the tunning of two voltages, V_{GS}

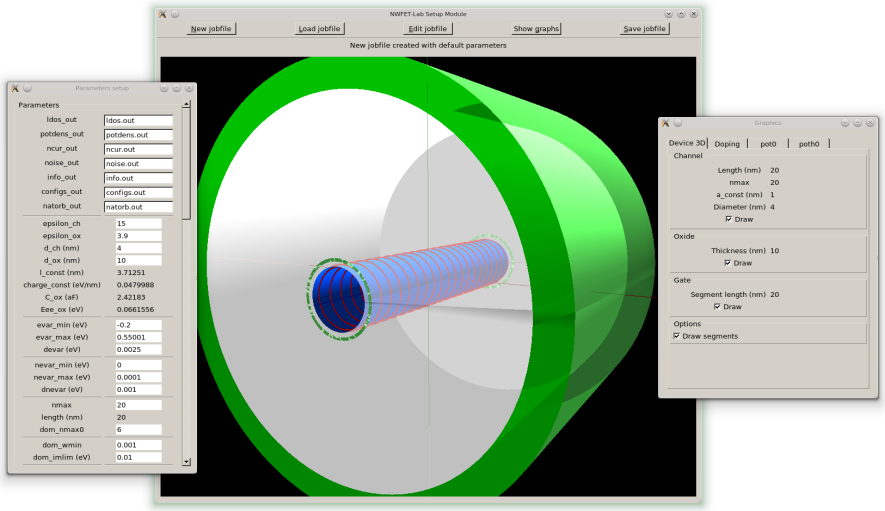

Figure A.2.: Screenshot of the setup module.

and V_{DS} which determine its operational regime and yield different values of its characteristics. The calculation module can run an array of different voltage pairs. If the number of voltage points is larger than one, the user can select the option of performing the calculations in parallel. This is possible because this module is programmed with parallel computing capabilities, thanks to the OpenMP API [122]. The user can choose whether to run simultaneously several voltage points along the V_{GS} or the V_{DS} axis, using for this task a selectable number of calculation threads. Optionally, the single-particle density matrix may be reset between points, although the algorithm performs more efficiently if the resulting single-particle density matrix of the previous calculation point is reused for different, close enough points. These options are available by pressing the "Threads options" button.

Once the calculation has been started after pressing the "Start" button, the textual output of the algorithm is displayed in the tabbed text windows that the calculation module features. Each tab with its associated output text window corresponds to each calculation thread. At the same time, this output is saved to as many logfiles as threads are running for later review. The user can select which tab to display and their text windows can be made auto-scrollable by checking the "Autoscroll" check button.

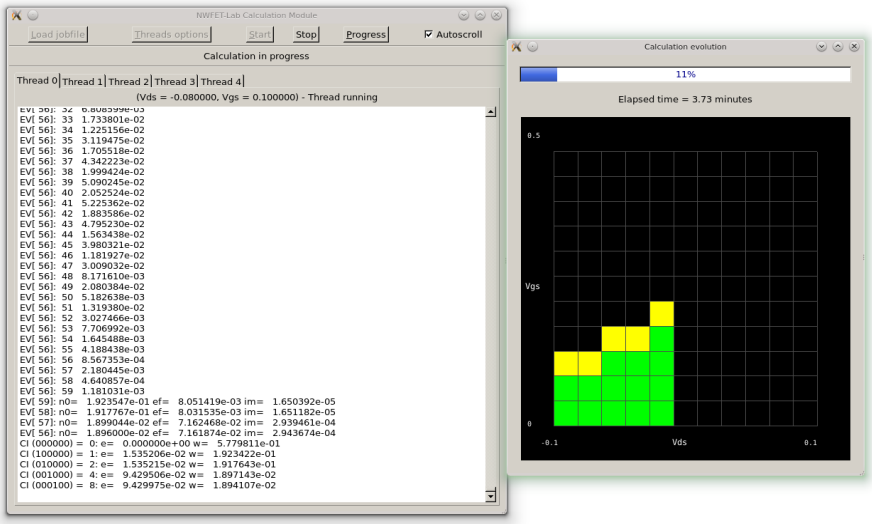

Figure A.3.: Screenshot of the calculation module.

Optionally a window with the evolution of the calculation may be displayed by pressing the button labeled "Progress". In this window a progress bar indicates the percentage of the total calculation that has already been performed, together with the elapsed time. Also displayed is an array with the voltage points involved in the calculation, with three different colors depending on their status: black for not yet computed, yellow for being computed and green for already computed. To end the calculation before it is finished the user may press the "Stop" button. Once the running algorithms for the current voltage points reach to an end, the program gracefully stops.

As a result of running the calculation module, output files containing the following quantities are obtained: local density of states (LDOS), potential, electron density, number of electrons, drain current, spin balance, current noise, natural orbitals with occupation numbers, density–density correlation, covariance, statistical operator: weights and eigenstates, single-particle reduced entropy, von Neumann entropy, modified entropy, energy, spin, current of natural orbitals, information about the weights and additional data related to the calculation

A.2.4. Graphical module

The graphical module is designed with the purpose of displaying graphical views of the several quantities obtained by the calculation module. In terms of the number of available options it is the most complex of the four modules. The OpenGL API is employed as the basis for the graphics and so GPUs may be used to process them more efficiently. No external graphical representation libraries were used, but all the details concerning graphics were programmed from scratch by means of OpenGL.

The first thing a user can do is to open a jobfile by pressing the "Load jobfile" button. Not only the relevant parameters for this module are read from the jobfile, but also the output files produced by the calculation module are read. This may take more or less time depending on the number of voltage points for which the calculation has been performed. Immediately after the data is loaded a floating window is opened with as many tabs available as output files were read. If a particular data file is missing, its associated tab is disabled.

The contents of all the tabs are similar. Starting from the top, a user can find the following groups of elements on a tab. First the "Graphs" group provides three choice buttons to select one out of three different types of graphs: 2D graph, 3D graph or colormap. Of these three types, the 2D graph and the colormap allow the user to read the coordinates of every point by clicking the mouse left button. Additionally, whenever the drain current or the single-particle-reduced entropy are being displayed as a function of V_{GS} and V_{DS} in a colormap, a new window may be opened with the electronic configurations and their weights corresponding to the voltage point selected by clicking the mouse right button.

Next the "Axis" group comprises up to three subgroups associated to each of the axis of the plot: X, Y and Z. The user can select which quantity to link with each axis, given the available quantities present in the data files of each particular tab. Some of these subgroups may be disabled if there is not enough number of independent variables to be represented in a given type of graph. Besides, if a 2D graph is selected the Z axis is disabled. The type of graph is restricted according to the same criterion. The independent variables that are not linked to an axis may be varied with the sliders present in the "Variables" group while the plot displayed on screen is immediately updated.

The fourth group is the "Scaling" group and is associated to the scaling of the

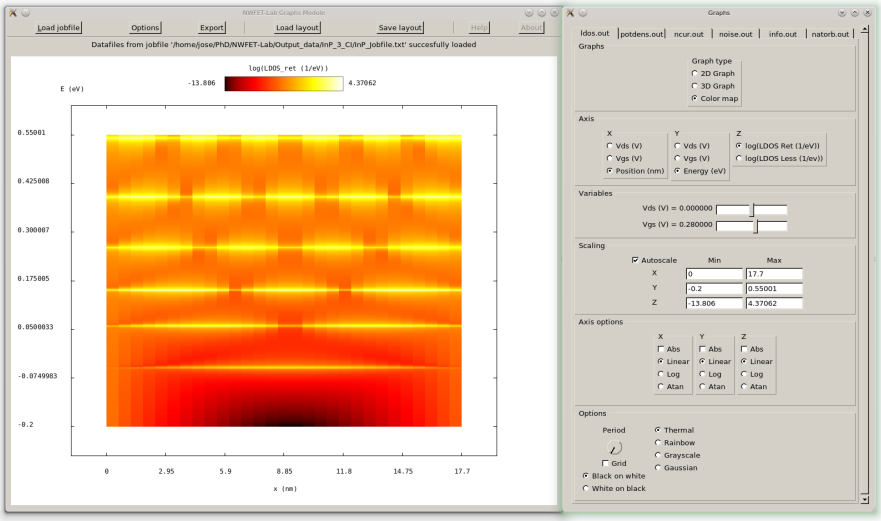

Figure A.4.: Screenshot of the graphical module.

graphs. Here, minimum and maximum limit values for each of the available axis can be entered, with the possibility to override these values and autoscale the graph. The "Axis options" group follows which contains choice buttons to select which transformations are performed on each of the available axis. These are: absolute value, linear scale, logarithmic scale and arctangent scale. Whenever the last option is chosen the user may enter the value of a factor by which to scale the argument of the arctangent axis scaling.

Finally, the "Options" group provides several choices related to the appearance of the graphs and its contents vary depending on the selected graph type. Common to all graph types, the user may choose between two color schemes: black lines on a white background or white lines on a black background. For a 3D graph the user may also choose the style of the plot: surface or mesh. For a colormap, the color gradient used in the representation may be selected from: thermal, rainbow, grayscale, Gaussian or positive/negative.

There is also the possibility to export the data currently being displayed to an external data file and to export the graphs to image files, by pressing the "Export" button. To conclude, the layout of the graphical module, consisting of the state of all its controls, may be saved to a layout file, similar to a jobfile but concerning only the appearance of this module. Later this file may be loaded so that the

saved layout is restored.

A.3. Technical details

A.3.1. Libraries and APIs

The way **NWFET-Lab** presents itself to the user is not as a text-based command-line interface but as a graphical user interface (GUI). The benefits of using a GUI are several. It enables easy change of the parameters by making them accessible to the user through controls of the interface. It enables also the interaction between the external user and the internal mechanisms of the program without the need of learning a complex command language. It makes faster and unifies the workflow of setting up a system, calculating its characteristics and displaying the results.

The choice of a GUI library for **NWFET-Lab** was guided by several considerations. First of all it should be easy to learn and use. In this sense poorly documented GUIs were discarded. The second important condition was its intrusiveness, whether to use it would require the code to be adapted to its canons or gave structural liberty to the programmer. This is connected to its programming style, either procedural or object-oriented. Since the selected language to write the software was C++ an object-oriented approach would be the best. Other considerations included platform dependence, variety of controls, OpenGL integration, inclusion of an own window manager and 64-bit compatibility.

According to these considerations, the GUI library of choice was FOX-Toolkit [117], a multiplatform, well-enough documented, open-source library released under the GNU Lesser General Public License. There are both a FOX forum and mailing list that were helpful whenever a question arose.

NWFET-Lab was designed from the beginning to be able to run calculations in parallel. Two different approaches to parallel computation were assessed: OpenMP [122] and MPI [126]. The benefits and drawbacks of each one are summarized in the following. On the one hand, OpenMP is easier to program and debug, its directives can be added incrementally which allows for gradual parallelization, if desired the code can be still run serially, serial code statements usually do not need modification and the code is easier to understand and maintain. On the other hand, it can be run only in shared memory computers and

requires a compiler that supports it. As for MPI, although it is able to run on both shared and distributed memory architectures and can be used on a wider range of problems, nevertheless requires more programming changes to go from serial to parallel version and can be harder to debug. Since shared memory computers are more common than computing grids and our code did not need more than what OpenMP could offer, this was the choice, which has proved to be a reliable and efficient option.

The details concerning the graphics were implemented starting from zero, instead of relying on external libraries. This allowed much control over the display options and features. For this purpose use was made of the OpenGL API [120], one of the most widely adopted graphics standards that produces high quality and high performance 2D and 3D graphics regardless of operating system or windowing system. It is a very well documented, easy to learn API. Since by itself OpenGL does not have the possibility to render text, the FTGL library [118] was employed for all text-based graphics, such as labels, titles and numbers along the plot axis. The DevIL image library [119] enabled the capturing of the plots displayed by the graphical module and saving them into image files. Finally, the calculation and many-body modules make use of LAPACK numerical routine libraries [121].

Links to the aforementioned libraries and APIs are presented in the following list:

FOX-Toolkit http://www.fox-toolkit.org/

OpenMP http://openmp.org/wp/

OpenGL http://www.opengl.org/

FTGL http://sourceforge.net/apps/mediawiki/ftgl/

DevIL http://openil.sourceforge.net/

LAPACK http://www.netlib.org/lapack/

A.3.2. Parameters

To itemize and clarify the meaning of the parameters used by **NWFET-Lab** a list with of all of them, together with short descriptions follows.

XXX_out Filename of the output datafile containing quantity XXX

obs_XXX Indicates whether to calculate or not the observable XXX

epsilon_ch Relative dielectric constant of the nanowire channel

epsilon_ox Relative dielectric constant of the oxide

d_ch Diameter of the nanowire channel

d_ox Thickness of the oxide

l_const Screening length λ

evar_min Minimum energy for LDOS calculation

evar_max Maximum energy for LDOS calculation

devar Energy step

nevar_min Minimum energy for current noise calculation

nevar_max Maximum energy for current noise calculation

dnevar Energy step

nmax Number of orbitals in 1D nanowire channel

dom_nmax0 Maximum number of relevant single-particle states

density_dom_thres1 Minimum absolute threshold for an occupied state

density_dom_thres2 Maximum absolute threshold for an empty state

density_dom_thres3 Relative threshold for a fluctuating state

coul_empty_thres Minimum threshold for state to be included in calculations (case B)

dom_slater_dets 0 for case B, 1 for case A, 2 for case A+B

dom_wmin Minimum value for a weight below which it is considered zero

dom_imlim Maximum dissipation energy due to contacts

dom_indep_w Switches on/off the independent electron regime

a_const Lattice constant of the nanowire channel

eff_mass Effective electron mass

t_const Tight-binding hopping matrix element $\hbar^2/(2m^*a^2)$

tc_const Contact hopping matrix element

charge_const $e^2/(2\varepsilon_0\varepsilon_{ch}A)$

current_const $e/\hbar$

temperature Temperature T

kt_const Thermal energy k_BT

imin_vgate Site index of gate minimum limit

imax_vgate Site index of gate maximum limit

vgate0 Minimum gate–source voltage

vgate1 Maximum gate–source voltage

dvgate Gate–source voltage step

vdrain0 Minimum drain–source voltage

vdrain1 Maximum drain–source voltage

dvdrain Drain–source voltage step

neq_nmin Non-equilibrium region minimum limit

neq_nmax Non-equilibrium region maximum limit

imin_npar Minimum site index for electron number count

imax_npar Maximum site index for electron number count

damp1 Self-consistency parameter

scount_min Self-consistency parameter

scount_max Self-consistency parameter

sdev_min Self-consistency parameter

dither_amp1 Self-consistency parameter

int_demin Related to the Runge-Kutta integration function.

int_demax Related to the Runge-Kutta integration function.

int_rezeps Related to the Runge-Kutta integration function.

doping Doping 1D charge density

pot0 Potential offset to band minimum

pot0_l Potential offset to band minimum within left contact

poth_l0 Potential height of left contact

pot0_r Potential offset to band minimum within right contact

poth_r0 Potential height of right contact

parallel_mode Set the voltage axis to be computed in parallel: 0 for V_{DS}, 1 for V_{GS}

nthreads Number of parallel threads for voltage loops

nthreads1 Number of parallel threads for case B

meanfield_rest Include mean-field interaction of the non-relevant states (case B)

meanfield_occ Include mean-field interaction of fixed occupied states (case B)

epsilon_const Optical potential

i_cur Layer of current

enable_cself Enable Coulomb self-energy

spinsplit Zeeman term

density_reset Switch on/off reset of single-particle density matrix between calculation points

hamop_diag Make many-body Hamiltonian diagonal (case B = case A)

B. Genetic algorithm

B.1. Overview

A general optimization problem consists of searching for the global optimum solution that optimizes a specific set of objective functions in a given search space. When considering a minimization or maximization problem, the goal is to find the best solution that minimizes or maximizes one or more objective functions. If the number of objective functions is greater than one, the problem is termed multi-objective optimization. We focus here in single-objective optimization and denote the single objective function as fitness function. These two terms are used in the following interchangeably.

The search space is defined by the number of variables that model the system and their limits. The fitness function has different values in each point of the search space and in general there may exist many local minima or maxima. These regions of the search space may constitute possible trap points of a given numerical optimization method such as a local search technique, which for example looks for the optimum solution using the gradient of the fitness function. Genetic algorithms on the contrary are able to leave these local optimum points behind, since they search in multiple directions, even if the fitness function is not differentiable.

A genetic algorithm (GA) [104] is an optimization method inspired by Darwin's theory of evolution. Its ingredients are a population of chromosomes, each of which encodes a possible solution to the problem, a set of operations performed on the chromosomes and a fitness function. A chromosome is composed of genes each of which encodes a variable of the problem and are defined within the limits of the search space. Its rules are such that after every iteration the population is expected to improve, based on the criterion defined by the fitness function for each chromosome. Each implementation of a GA has its own peculiarities. We

0. Init population: produce set of chromosomes and evaluate fitness.
1. Selection: population → mating pool.
2. Reproduction (crossover): mating pool → offspring.
3. Mutation: population → offspring.
4. Evaluate fitness of the offspring.
5. Select best chromosomes → new generation.
6. Check convergence: if converged then end, else go to 1.

Table B.1.: A typical GA.

describe a single-objective standard version and note that a specific version may deviate in some details from it.

At the beginning the method constructs a population of chromosomes, randomly or otherwise, taking care that each gene is within its domain of definition. Then it enters into an iterative process, first selecting for reproduction a fraction of the population that has the best fitness and constitute the mating pool. Note that by choosing the fittest individuals the next generation should in principle be better than the previous. Secondly comes the reproduction phase, a crossover operation is applied between two or more randomly picked chromosomes from the mating pool, generating new offspring. The characteristics of the parent chromosomes are inherited by the offspring. And thirdly several randomly chosen chromosomes are mutated by altering the values of their genes by a small random amount. This adds variety to the population and avoids the algorithm to get stuck in a local minimum or maximum. These three steps, selection, reproduction and mutation, produce a new generation which replaces the previous population. Such algorithm is repeated until a termination criterion is satisfied. Convergence is achieved if the fitness of the best chromosome in the population is smaller or greater than a certain threshold value, in the case of a minimization or maximization problem respectively, and/or if the fitness of the best chromosome does not change appreciably between subsequent iterations. See Table B.1 for a schematic view of a typical GA.

B.2. Chang's genetic algorithm

The GA by Chang [105] is novel because it introduces a multi-crossover formula which makes use of three instead of the traditional two chromosomes to generate three new ones. Let Θ_i represent a vector of genes or chromosome. Suppose that three chromosomes Θ_1, Θ_2 and Θ_3 are randomly chosen from the mating pool to crossover and that Θ_1 is the fittest of them. They define a new adjusting direction

$$\Theta_D \equiv (\Theta_1 - \Theta_2) + (\Theta_1 - \Theta_3) = 2\Theta_1 - \Theta_2 - \Theta_3 \tag{B.1}$$

along which all three chromosomes are changed simultaneously. If $r \in [0, 1]$ is a random number determining the crossover grade, the following multiple crossover formulas are performed

$$\begin{aligned} \Theta_1 + r\Theta_D &\to \Theta_1' \\ \Theta_2 + r\Theta_D &\to \Theta_2' \\ \Theta_3 + r\Theta_D &\to \Theta_3' \end{aligned} \tag{B.2}$$

which mean that the offspring Θ_i' will be translated copies of the parents along the direction that points to the fittest of the three.

Similarly to other GAs, the mating pool is generated by tournament selection, but as an alternative to Chang's original implementation this can be done by randomly selecting in N_{pop} rounds, t chromosomes from the total of N_{pop} that constitute the population and choosing the single best fit of those t for inclusion in the mating pool, which ends up containing N_{pop} chromosomes. The multi-crossover operation and mutation are performed with a probability p_c and p_m respectively, so that the $(3 \times p_c)\%$ of the mating pool undergoes reproduction and a $p_m\%$ of the population is mutated to a certain degree.

C. Parametrization of unitary matrices

In this section we describe how to factorize any given unitary matrix as a product of several unimodular unitary matrices which depend on a set of angles or parameters. This parametrization method was introduced by Murnaghan and except for the compact expression at the end of the section, we have followed his steps as given in Ref. [116].

An n-dimensional unitary matrix U satisfies the equation $U^\dagger U = I$, which implies $U^{-1} = U^\dagger$. Because $\det U^\dagger = (\det U)^*$ it follows that $\det U = e^{i\phi}$ is a complex number of unit modulus. Whenever $\det U = 1$ we term U unimodular unitary matrix.

Before describing how to parametrize an n-dimensional unitary matrix we introduce the so called plane n-dimensional unimodular unitary matrices $U_{pq}(\phi, \sigma)$, which operate in the pq-plane, where $q > p$. They are constructed in such a way that the diagonal terms are 1 except for $(U_{pq})_{pp} = (U_{pq})_{qq} = \cos\phi$ and the non-diagonal terms are 0 except for $(U_{pq})_{qp} = \sin\phi\ e^{i\sigma}$ and $(U_{pq})_{pq} = -\sin\phi\ e^{-i\sigma}$. For example, when n=3

$$U_{13}(\phi, \sigma) = \begin{pmatrix} \cos\phi & 0 & -\sin\phi\ e^{-i\sigma} \\ 0 & 1 & 0 \\ \sin\phi\ e^{i\sigma} & 0 & \cos\phi \end{pmatrix} \quad . \tag{C.1}$$

Let us also define an n-dimensional diagonal matrix

$$D(\delta_1, \delta_2, \ldots, \delta_n) = \mathrm{Diag}(e^{i\delta_1}, e^{i\delta_2}, \ldots, e^{i\delta_n}) \quad . \tag{C.2}$$

We are now in a position to describe the parametrization method. We will give only the final result, for a detailed explanation on how to arrive at it see Ref. [116].

Let U be any given n-dimensional unitary matrix. It can be shown that it can be expressed as the following product

$$U = U^{(n-1)} U_{12}(\theta_{n-2}, \sigma_{n-1}) U_{13}(\theta_{n-3}, \sigma_{n-2}) \cdots U_{1(n-1)}(\theta_1, \sigma_2) U_{1n}(\phi_1, \sigma_1) \quad \text{(C.3)}$$

where $U^{(n-1)}$ is an n-dimensional unitary matrix with the form

$$U^{(n-1)} = \begin{pmatrix} e^{i\delta_1} & 0 \\ 0 & V \end{pmatrix} \quad \text{(C.4)}$$

and V is an $(n-1)$-dimensional unitary matrix. The plane matrices can be readily computed, given their angles. Hence once the matrix V is known from the application of the same prescription to the expression of an $(n-1)$-dimensional unitary matrix, U is completely determined.

Let us consider the case $n = 3$. The parametric form of a general 2-dimensional unitary matrix has the expression

$$V = D(\delta_2, \phi_3) U_{12}(\phi_2, \sigma_3) \quad \text{(C.5)}$$

as it appears in Eq. (C.4), from which it follows that

$$U^{(2)} = D(\delta_1, \delta_2, \phi_3) U_{23}(\phi_2, \sigma_3) \quad \text{(C.6)}$$

and therefore we obtain the factorization of the 3-dimensional unitary matrix U as

$$U = D(\delta_1, \delta_2, \phi_3) U_{23}(\phi_2, \sigma_3) U_{12}(\theta_1, \sigma_2) U_{13}(\phi_1, \sigma_1) \quad . \quad \text{(C.7)}$$

Thus any 3-dimensional unitary matrix is parametrized by a set of 9 angles.

To clearly show the iterative process, let us take the case of $n = 4$.

$$\begin{aligned} U = & [D(\delta_1, \delta_2, \delta_3, \phi_4) U_{34}(\phi_3, \sigma_6) U_{23}(\theta_3, \sigma_5) U_{24}(\phi_2, \sigma_4)] \cdot \\ & \cdot U_{12}(\theta_2, \sigma_3) U_{13}(\theta_1, \sigma_2) U_{14}(\phi_1, \sigma_1) \end{aligned} \quad \text{(C.8)}$$

where the product between brackets comes from identifying with V the expression of a 3-dimensional unitary matrix as given by Eq. (C.7), yielding $U^{(3)}$. We see that any 4-dimensional unitary matrix is parametrized by a set of 16 angles.

In the general n-dimensional case the number of parameters is n^2, of which the

n angles ϕ are longitude angles $\in [-\pi, \pi[$ and the $n-1$ angles δ, the $n(n-1)/2$ angles σ and the $(n-1)(n-2)/2$ angles θ are latitude angles $\in [-\pi/2, \pi/2]$. The number of plane matrices U_{pq} that appear in the factorization is $n(n-1)/2$.

Any given n-dimensional unitary matrix U may be expressed in compact form as

$$U = D(\delta_1, \ldots, \delta_{n-1}, \phi_n) \prod_{p=n-1}^{1} \left(\prod_{q=p+1}^{n-1} U_{pq}(\theta_{x-p}, \sigma_x) \right) U_{pn}(\phi_p, \sigma_x) \qquad \text{(C.9)}$$

where the index of σ obeys the rule $x = 1 + np - q - p(p-1)/2$ so that the ordering of the angles is adequate. The first sequence product runs backwards from higher to lower values of p, the second may not be evaluated if $q > n-1$.

References

[1] M. S. Lundstrom and J. Guo. *Nanoscale Transistors: Device Physics, Modeling and Simulation*. United States of America: Springer, 2006.

[2] G. E. Moore. "Cramming more components onto integrated circuits". In: *Electronics* 38.8 (1965).

[3] G. E. Moore. "Progress in digital integrated electronics". In: *Electron Devices Meeting, 1975 International* 21 (1975), pp. 11–13.

[4] R. H. Dennard et al. "Design of Ion-Implanted MOSFET's with Very Small Physical Dimensions". In: *IEEE Journal Of Solid-State Circuits* 9.5 (1974).

[5] A. Chaudhry. *Fundamentals of Nanoscaled Field Effect Transistors*. Springer, 2013.

[6] *Process Integration, Devices, and Structures*. Tech. rep. International Technology Roadmap for Semiconductors, 2013. URL: http://www.itrs.net/.

[7] Y. Xia et al. "One-Dimensional Nanostructures: Synthesis, Characterization, and Applications". In: *Advanced Materials* 15.5 (2003).

[8] W. Lu and C. M. Lieber. "Semiconductor nanowires". In: *Journal of Physics D: Applied Physics* 39 (2006), R387–R406.

[9] V. Schmidt et al. "Silicon Nanowires: A Review on Aspects of their Growth and their Electrical Properties". In: *Advanced Materials* 21 (2009), pp. 2681–2702.

[10] C. M. Lieber. "Semiconductor nanowires: A platform for nanoscience and nanotechnology". In: *MRS Bulletin* 36 (2011), pp. 1052–1063.

[11] R. G. Hobbs, N. Petkov, and J. D. Holmes. "Semiconductor Nanowire Fabrication by Bottom-Up and Top-Down Paradigms". In: *Chemistry of Materials* 24 (2012), pp. 1975–1991.

[12] Y. Cui et al. “High Performance Silicon Nanowire Field Effect Transistors”. In: *Nano Letters* 3.2 (2003).

[13] H. Yan et al. “Programmable nanowire circuits for nanoprocessors”. In: *Nature* 470 (2011), pp. 240–244.

[14] G. Larrieu and X.-L. Han. “Vertical nanowire array-based field effect transistors for ultimate scaling”. In: *Nanoscale* 5.2437 (2013).

[15] J. Yao et al. “Nanowire nanocomputer as a finite-state machine”. In: *PNAS* 111.7 (2014), pp. 2431–2435.

[16] M. S. Gudiksen et al. “Growth of nanowire superlattice structures for nanoscale photonics and electronics”. In: *Nature* 415 (2002), pp. 617–620.

[17] B. Tian, T. J. Kempa, and C. M. Lieber. “Single nanowire photovoltaics”. In: *Chemical Society Reviews* 38 (2009), pp. 16–24.

[18] P. Krogstrup et al. “Single-nanowire solar cells beyond the Shockley–Queisser limit”. In: *Nature Photonics* 7 (2013), pp. 306–310.

[19] F. Patolsky and C. M. Lieber. “Nanowire nanosensors”. In: *Materials Today* 8.4 (2005).

[20] F. Patolsky et al. “Detection, Stimulation, and Inhibition of Neuronal Signals with High-Density Nanowire Transistor Arrays”. In: *Science* 313 (2006), pp. 1100–1104.

[21] F. Patolsky et al. “Nanowire-Based Nanoelectronic Devices in the Life Sciences”. In: *MRS Bulletin* 32 (2007), pp. 142–149.

[22] Q. Qing et al. “Free-standing kinked nanowire transistor probes for targeted intracellular recording in three dimensions”. In: *Nature Nanotechnology* 9 (2014), pp. 142–147.

[23] P.-C. Chang and J. G. Lu. “ZnO Nanowire Field-Effect Transistors”. In: *IEEE Transactions On Electron Devices* 55.11 (2008), pp. 2977–2987.

[24] L. J. Brillson and Y. Lu. “ZnO Schottky barriers and Ohmic contacts”. In: *Journal of Applied Physics* 109.121301 (2011).

[25] D. S. Reddy et al. “Schottky Barrier Parameters of Pd/Ti Contacts on N-Type InP Revealed from I-V-T And C-V-T Measurements”. In: *Journal of Modern Physics* 2 (2011), pp. 113–123.

[26] J. Appenzeller et al. “Toward Nanowire Electronics”. In: *IEEE Transactions On Electron Devices* 55.11 (2008).

[27] C. P. Auth and J. D. Plummer. “Scaling Theory for Cylindrical, Fully-Depleted, Surrounding-Gate MOSFET’s”. In: *IEEE Electron Device Letters* 18.2 (1997).

[28] G. T. Kim et al. “Field-effect transistor made of individual V_2O_5 nanofibers”. In: *Applied Physics Letters* 76.14 (2000).

[29] X. Duan et al. “Indium phosphide nanowires as building blocks for nanoscale electronic and optoelectronic devices”. In: *Nature* 409 (2001), pp. 66–69.

[30] J. Xiang et al. “Ge/Si nanowire heterostructures as high-performance field-effect transistors”. In: *Nature* 441 (2006), pp. 489–493.

[31] A. I. Hochbaum et al. “Controlled Growth of Si Nanowire Arrays for Device Integration”. In: *Nano Letters* 5.3 (2005).

[32] E. Latu-Romain et al. “A generic approach for vertical integration of nanowires”. In: *Nanotechnology* 19.345304 (2008).

[33] Y. Huang et al. “Directed Assembly of One-Dimensional Nanostructures into Functional Networks”. In: *Science* 291.5504 (2001).

[34] S. E. Laux, A. Kumar, and M. V. Fischetti. “Analysis of quantum ballistic electron transport in ultrasmall silicon devices including space-charge and geometric effects”. In: *Journal of Applied Physics* 95.10 (2004), pp. 5545–5582.

[35] T. J. Walls and K. K. Likharev. “Two-dimensional quantum effects in "ultimate" nanoscale metal-oxide-semiconductor field-effect transistors”. In: *Journal of Applied Physics* 104.124307 (2008).

[36] M. Nedjalkov et al. “A Wigner equation with quantum electron-phonon interaction”. In: *Microelectronic Engineering* 63 (2002), pp. 199–203.

[37] R. Gebauer and R. Car. “Kinetic theory of quantum transport at the nanoscale”. In: *Physical Review B* 70.125324 (2004).

[38] M. V. Fischetti. “Master-equation approach to the study of electronic transport in small semiconductor devices”. In: *Physical Review B* 59.7 (1999).

[39] S. Datta. "Nanoscale device modeling: the Green's function method". In: *Superlattices and Microstructures* 28.4 (2000).

[40] P. Danielewicz. "Quantum Theory of Nonequilibrium Processes, I". In: *Annals of Physics* 152 (1984), pp. 239–304.

[41] S. Datta. *Electronic Transport in Mesoscopic Systems*. Cambridge University Press, 1999.

[42] J. Rammer. *Quantum Field Theory of Non-Equilibrium States*. Cambridge University Press, 2007.

[43] H. Haug and A.-P. Jauho. *Quantum Kinetics in Transport and Optics of Semiconductors*. Springer, 2008.

[44] R. A. Jishi. *Feynman Diagram Techniques in Condensed Matter Physics*. Cambridge University Press, 2013.

[45] K. M. Indlekofer, J. Knoch, and J. Appenzeller. "Quantum kinetic description of Coulomb effects in one-dimensional nanoscale transistors". In: *Physical Review B* 72.125308 (2005).

[46] K. M. Indlekofer, J. Knoch, and J. Appenzeller. "Understanding Coulomb Effects in Nanoscale Schottky-barrier-FETs". In: *IEEE Transactions On Electron Devices* 54.6 (2007).

[47] H. Haken. *Quantum Field Theory of Solids: an Introduction*. North-Holland, 1983.

[48] W. Schäfer and M. Wegener. *Semiconductor Optics and Transport Phenomena*. Springer, 2002.

[49] G. Stefanucci and R. van Leeuwen. *Nonequilibrium Many-Body Theory of Quantum Systems*. Cambridge University Press, 2013.

[50] J. Maciejko. *An Introduction to Nonequilibrium Many-Body Theory*. Springer, 2007.

[51] K. M. Indlekofer. *Introduction to the Non-Equilibrium Green's Function Formalism for the Simulation of Nanoelectronic Devices*. Tech. rep. IMtech, Hochschule RheinMain - University of Applied Sciences, Germany, 2013.

[52] R. Venugopal et al. "Simulating quantum transport in nanoscale transistors: Real versus mode-space approaches". In: *Journal of Applied Physics* 92.7 (2002).

[53] R. Lake et al. "Single and multiband modeling of quantum electron transport through layered semiconductor devices". In: *Journal of Applied Physics* 81.12 (1997), pp. 7845–7869.

[54] A. Svizhenko et al. "Two-dimensional quantum mechanical modeling of nanotransistors". In: *Journal of Applied Physics* 91.4 (2002), pp. 2343–2354.

[55] C. Rivas and R. Lake. "Non-equilibrium Green function implementation of boundary conditions for full band simulations of substrate-nanowire structures". In: *Physica Status Solidi (B)* 239.1 (2003), pp. 94–102.

[56] D. Mamaluy, M. Sabathil, and P. Vogl. "Efficient method for the calculation of ballistic quantum transport". In: *Journal of Applied Physics* 93.8 (2003), pp. 4628–4633.

[57] D. Mamaluy et al. "Contact block reduction method for ballistic transport and carrier densities of open nanostructures". In: *Physical Review B* 71.245321 (2005).

[58] S. Birner et al. "Ballistic quantum transport using the contact block reduction (CBR) method". In: *Journal of Computational Electronics* 8 (2009), pp. 267–286.

[59] J. Wang, E. Polizzi, and M. Lundstrom. "A three-dimensional quantum simulation of silicon nanowire transistors with the effective-mass aproximation". In: *Journal of Applied Physics* 96.4 (2004), pp. 2192–2203.

[60] E. Polizzi and N. Ben Abdallah. "Subband decomposition approach for the simulation of quantum electron transport in nanostructures". In: *Journal of Computational Physics* 202 (2005), pp. 150–180.

[61] Y. M. Sabry, T. M. Abdolkader, and W. F. Farouk. "Uncoupled mode-space simulation validity for double gate MOSFETs". In: *International Conference on Microelectronics*. 2007, pp. 351–354.

[62] D. Selim et al. "Rapid and Efficient Method for Numerical Quantum Mechanical Simulation of Gate-All-Around Nanowire Transistors". In: *International Conference on Microelectronics*. 2012, pp. 229–232.

[63] H. Takeda and N. Mori. "Mode-Coupling Effects in Non-Equilibrium Green's Function Device Simulation". In: *Japanese Journal of Applied Physics* 44.4B (2005), pp. 2664–2668.

[64] M. Luisier, A. Schenk, and W. Fichtner. "Quantum transport in two- and three-dimensional nanoscale transistors: Coupled mode effects in the nonequilibrium Green's function formalism". In: *Journal of Applied Physics* 100.043713 (2006).

[65] A. Martinez et al. "3-D Nonequilibrium Green's Function Simulation of Nonperturbative Scattering From Discrete Dopants in the Source and Drain of a Silicon Nanowire Transistor". In: *IEEE Transactions On Nanotechnology* 8.5 (2009), pp. 603–610.

[66] B. C. Johnson et al. "Darin current modulation in an nanoscale field-effect-transistor channel by single dopant implantation". In: *Applied Physics Letters* 96.264102 (2010).

[67] A. Martinez et al. "NEGF simulations of a junctionless Si gate-all-around nanowire transistor with discrete dopants". In: *Solid-State Electronics* 71 (2012), pp. 101–105.

[68] M. Aldegunde, A. Martinez, and J. R. Barker. "Study of Discrete Doping-Induced Variability in Junctionless Nanowire MOSFETs Using Dissipative Quantum Transport Simulations". In: *IEEE Electron Device Letters* 33.2 (2012), pp. 194–196.

[69] N. D. Akhavan et al. "Influence of discrete dopant on quantum transport in silicon nanowire transistors". In: *Solid-State Electronics* 70 (2012), pp. 92–100.

[70] V. P. Georgiev, E. A. Towie, and A. Asenov. "Impact of Precisely Positioned Dopants on the Performance of an Ultimate Silicon Nanowire Transistor: A Full Three-Dimensional NEGF Simulation Study". In: *IEEE Transactions On Electron Devices* 60.3 (2013).

[71] N. D. Akhavan et al. "Discrete Dopant Impurity Scattering in p-Channel Silicon Nanowire Transistors: A $k \cdot p$ Approach". In: *IEEE Transactions On Electron Devices* 61.2 (2014), pp. 386–393.

[72] C. Buran et al. "Three-Dimensional Real-Space Simulation of Surface Roughness in Silicon Nanowire FETs". In: *IEEE Transactions On Electron Devices* 56.10 (2009).

[73] A. Martinez et al. "Variability in Si Nanowire MOSFETs Due to the Combined Effect of Interface Roughness and Random Dopants: A Fully Three-Dimensional NEGF Simulation Study". In: *IEEE Transactions On Electron Devices* 57.7 (2010).

[74] A. Cresti et al. "A Comparative Study of Surface-Roughness-Induced Variability in Silicon Nanowire and Double-Gate FETs". In: *IEEE Transactions On Electron Devices* 58.8 (2011), pp. 2274–2281.

[75] V. P. Georgiev, E. A. Towie, and A. Asenov. "Interactions Between Precisely Placed Dopants and Interface Roughness in Silicon Nanowire Transistors: Full 3-D NEGF Simulation Study". In: *SISPAD 2013*. 2013.

[76] F. G. Pikus and K. K. Likharev. "Nanoscale field-effect transistors: An ultimate size analysis". In: *Applied Physics Letters* 71.25 (1997).

[77] E. N. Economou. *Green's Functions in Quantum Physics*. Springer, 2006.

[78] S. Adachi. *Physical Properties of III-V Semiconductor Compounds: InP, InAs, GaAs, GaP, InGaAs, and InGaAsP*. New York: John Wiley & Sons, 1992.

[79] P.-O. Löwdin. "Quantum Theory of Many-Particle Systems. I. Physical Interpretations by Means of Density Matrices, Natural Spin-Orbitals, and Convergence Problems in the Method of Configuration Interaction". In: *Physical Review* 97.6 (1955).

[80] E. R. Davidson. "Properties and Uses of Natural Orbitals". In: *Reviews of Modern Physics* 44.3 (1972).

[81] K. M. Indlekofer. *whiskersim*. 2011. URL: http://sourceforge.net/projects/whiskersim/.

[82] J. M. Castelo and K. M. Indlekofer. *NWFET-Lab*. 2014. URL: http://sourceforge.net/projects/nwfetlab/.

[83] K. M. Indlekofer. Diploma Thesis. RWTH Aachen, 1996.

[84] P. N. Racec, E. R. Racec, and H. Neidhardt. "Evanescent channels and scattering in cylindrical nanowire heterostructures". In: *Physical Review B* 79.155305 (2009).

[85] Z. Fan and J. G. Lu. "Zinc Oxide Nanostructures: Synthesis and Properties". In: *Journal of Nanoscience and Nanotechnology* 5.10 (2005), pp. 1561–1573.

[86] M. A. Kastner. "The single-electron transistor". In: *Reviews of Modern Physics* 64.3 (1992).

[87] H. van Houten et al. "Single Charge Tunneling". In: *NATO ASI Series B294, New York: Plenum* 167 (1992).

[88] K. K. Likharev. "Single-Electron Devices and Their Applications". In: *Proceedings of the IEEE* 87.4 (1999).

[89] L. P. Kouwenhoven, D. G. Austing, and S. Tarucha. "Few-electron quantum dots". In: *Reports on Progress in Physics* 64 (2001), pp. 701–736.

[90] W. Tai-hong, L. Hong-wei, and Z. Jun-ming. "Coulomb blockade oscillations of Si single-electron transistors". In: *Chinese Physics* 10.9 (2001), pp. 844–846.

[91] S. De Franceschi et al. "Single-electron tunneling in InP nanowires". In: *Applied Physics Letters* 83.2 (2003).

[92] M. T. Björk et al. "Few-Electron Quantum Dots in Nanowires". In: *Nano Letters* 4.9 (2004), pp. 1621–1625.

[93] K. H. Cho et al. "Observation of Single Electron Tunneling and Ballistic Transport in Twin Silicon Nanowire MOSFETs (TSNWFETs) Fabricated by Top-Down CMOS Process". In: *Electron Devices Meeting, 2006. IEDM '06. International*. Dec. 2006, pp. 1–4.

[94] S. Hershfield. "Reformulation of Steady State Nonequilibrium Quantum Statistical Mechanics". In: *Physical Review Letters* 70.14 (1993).

[95] P. Bokes and R. W. Godby. "Maximum-entropy theory of steady-state quantum transport". In: *Physical Review B* 68.125414 (2003).

[96] A. Dhar, K. Saito, and P. Hänggi. "Nonequilibrium density-matrix description of steady-state quantum transport". In: *Physical Review E* 85.011126 (2012).

[97] H. Ness. "Nonequilibrium density matrix for quantum transport: Hershfield approach as a McLennan-Zubarev form of the statistical operator". In: *Physical Review E* 88.022121 (2013).

[98] J. M. Castelo and K. M. Indlekofer. "Numerical determination of the non-equilibrium many-body statistical operator for a nanowire-based field-effect transistor". In: *Deutsche Physikalische Gesellschaft*. Poster presentation. Dresden, 2014.

[99] J. M. Castelo and K. M. Indlekofer. "Numerical determination of a non-equilibrium many-body statistical operator for quasi-bound electrons in a gated nanowire system". In: *arXiv:1406.4312v1 [cond-mat.mes-hall]* (2014).

[100] J. M. Castelo and K. M. Indlekofer. "Modified correlation entropy of a gated nanowire system described by a numerically determined non-equilibrium many-body statistical operator". In: *Physica Status Solidi (B)* (2015). DOI: 10.1002/pssb.201552174.

[101] K. M. Indlekofer. *newbpotcoul*. 2011. URL: http://sourceforge.net/projects/newbpotcoul/.

[102] A. Berera. *Notes for Senior Honours/Integrated Masters: Statistical Physics, Section 2*. School of Physics and Astronomy, University of Edinburgh. 2012.

[103] K. M. Indlekofer. Private communication. 2013.

[104] R. L. Haupt and S. E. Haupt. *Practical Genetic Algorithms*. John Wiley & Sons, Inc., 2004.

[105] W.-D. Chang. "An improved real-coded genetic algorithm for parameters estimation of nonlinear systems". In: *Mechanical Systems and Signal Processing* 20 (2006), pp. 236–246.

[106] J. J. Sakurai. *Modern Quantum Mechanics*. Addison-Wesley, 2011.

[107] P. Ziesche. "Correlation Strength and Information Entropy". In: *International Journal of Quantum Chemistry* 56 (1995), pp. 363–369.

[108] R. O. Esquivel et al. "Physical interpretation of information entropy: Numerical evidence of the Collins conjecture". In: *Physical Review A* 54.1 (1996).

[109] P. Ziesche et al. "Two-site Hubbard model, the Bardeen-Cooper-Schrieffer model, and the concept of correlation entropy". In: *Physical Review B* 55.16 (1997).

[110] P. Gersdorf et al. "Correlation Entropy of the H_2 Molecule". In: *International Journal of Quantum Chemistry* 61 (1997), pp. 935–941.

[111] K. M. Indlekofer and J. M. Castelo. "On The Correlation Entropy of Discrete Nanoelectronic Systems". In: *Annales Universitatis Scientiarum Budapestinensis de Rolando Eötvös Nominatae, Sectio Computatorica* 39 (2013), pp. 149–159.

[112] J. M. Castelo, K. M. Indlekofer, and J. Malindretos. "On the single-particle-reduced entropy of a gated nanowire system in the Coulomb blockade regime". In: *Physica Status Solidi RRL* 7.10 (2013), pp. 907–910.

[113] A. D. Gottlieb and N. J. Mauser. "New Measure of Electron Correlation". In: *Physical Review Letters* 96.123003 (2005).

[114] K. Byczuk et al. "Quantification of Correlations in Quantum Many-Particle Systems". In: *Physical Review Letters* 108.087004 (2012).

[115] A. Wehrl. "General properties of entropy". In: *Reviews of Modern Physics* 50.2 (1978), pp. 221–260.

[116] F. D. Murnaghan. *The Unitary And Rotation Groups*. Washington, D. C.: Spartan books, 1962.

[117] *FOX Toolkit*. 2014. URL: http://www.fox-toolkit.org/.

[118] *FTGL*. 2013. URL: http://sourceforge.net/projects/ftgl/.

[119] *DevIL*. 2014. URL: http://openil.sourceforge.net/.

[120] R. S. Wright Jr., B. Lipchak, and N. Haemel. *OpenGL superbible: comprehensive tutorial and reference*. Addison-Wesley, 2007.

[121] E. Anderson et al. *LAPACK User's Guide*. SIAM, 1999.

[122] R. Chandra et al. *Parallel Programming in OpenMP*. Morgan Kaufmann Publishers, 2001.

[123] B. Eckel. *Thinking in C++: Introduction to Standard C++*. Prentice Hall, 2000.

[124] *GNU General Public License, version 2*. 1991. URL: http://www.gnu.org/licenses/gpl-2.0.html.

[125] K. N. King. *C Programming: A Modern Approach*. W. W. Norton & Company, 2008.

[126] W. Gropp, E. Lusk, and A. Skjellum. *Using MPI: Portable Parallel Programming with the Message Passing Interface*. The MIT Press, 1999.